AN ABSTRACT OF THE THESIS OF

Wenwen Li for the degree of Master of Ocean Engineering in Ocean Engineering presented on September 19, 2006.

Title: Analysis of Pressure Variations Observed at the Ocean Bottom during the 2003 Tokachi-Oki Earthquake

Redacted for privacy

Abstract approved:

Harry Yeh

Most tsunami studies have been conducted based on the incompressible fluid theory. However water compressibility must be considered for the process of tsunami generation by bottom displacements during submarine earthquakes. During the 2003 Tokachi-Oki earthquake, the ocean-bottom pressure variations were registered by the pressure gauges PG1 and PG2 located right in the tsunami source area. The co-seismic ocean-bottom displacements were estimated by the observed ocean-bottom pressure variations. The pressure waves (acoustic waves) traveling back and forth between the hard bottom and the water surface were generated due to the ocean bottom displacements during the earthquake.

In this study, the e-folding time for the attenuation of pressure wave was estimated for the mainshock and the following three aftershocks. The amplitude modulation of the pressure fluctuations at PG1 caused by the mainshock was investigated by applying the variable-frequency complex demodulation method (VFCDM). The

temporal evolution of amplitude spectra indicates that the dominant frequency of the pressure wave decreases gradually.

The numerical simulation of the pressure wave is conducted by using a one-dimensional model with the method of characteristics and the finite-difference scheme. The numerical model is base on the linear momentum equation and the conservation of mass. Results show that the dominant frequency of the simulated pressure wave is in good coincidence with that of the measurement if sediment layers are taken into account. This strongly suggests that the sediment layers must play a role in the formation of the pressure wave caused by the earthquake.

©Copyright by Wenwen Li
September 19, 2006
All Rights Reserved

Analysis of Pressure Variations Observed at the Ocean Bottom during the 2003 Tokachi-Oki Earthquake

by
Wenwen Li

A THESIS

submitted to

Oregon State University

in partial fulfillment of
the requirements for the
degree of

Master of Ocean Engineering

Presented September 19, 2006
Commencement June 2007

Master of Ocean Engineering thesis of Wenwen Li
presented on September 19, 2006.

APPROVED:

Redacted for privacy

Major Professor, representing Ocean Engineering

Redacted for privacy

Head of the Department of Civil, Construction and Environmental Engineering

Redacted for privacy

Dean of the Graduate School

I understand that my thesis will become part of the permanent collection of the Oregon State University libraries. My signature below authorizes release of my thesis to any reader upon request.

Li Wenwen.

Wenwen Li, Author

TABLE OF CONTENTS

TABLE OF CONTENTS (Continued)

Page

LIST OF FIGURES

LIST OF FIGURES (Continued)

Figure Page

LIST OF FIGURES (Continued)

LIST OF FIGURES (Continued)

LIST OF TABLES

Analysis of Pressure Variations Observed at the Ocean Bottom during the 2003 Tokachi-Oki Earthquake

1 Introduction

On September 26, 2003 at 04:50:06 JST (Japan Standard Time, nine hours ahead to UTC (Coordinated Universal Time), a large thrust-type earthquake occurred along the Kuril Trench near Tokachi, Hokkaido, Northern Japan. The epicenter (41.78°N, 144.08°E) is approximately 60 km east of Cape Erimo and 42 km deep under the seabed reported by Japan Meteorological Agency (JMA) or 27 km deep by U.S. Geological Survey (USGS). The seismic moment magnitude (Mw) is 8.0 (JMA) or 8.3 (USGS). Yamanaka and Kikuchi (2003) estimated the source duration to be 40 seconds and the maximum slip to be 5.8 meters. This earthquake was an inter-plate earthquake associated with the subduction of the Pacific plate under the Eurasian plate. The rupture propagated northward from the shallow to deep region (Yamanaka and Kikuchi, 2003). This earthquake occurred in the same area as the previous Tokachi-Oki inter-plate earthquake ($Mw = 8.2$) on March 4, 1952 (Hirata *et al.*, 2004). A number of aftershocks subsequently occurred around the epicenter of the 2003 Tokachi-Oki mainshock. Among them, the largest aftershock (epicenter: 41.71°N, 143.69°E; Mw: 7.1 (JMA); depth: 21km) took place at 06:08 local time, a little more than one hour after the mainshock (Ueno *et al.*, 2003). The aftershock area was almost the same as that of the 1952 Tokachi-Oki earthquake (Ichiyanagi *et al.*, 2004).

This earthquake generated a series of tsunamis that struck coastal areas in the Hokkaido and Tohoku regions, causing coastal flooding, washing away many containers at Port of Kushiro, floating automobiles in many locations, and two people are missing. Fortunately, there was little serious damage of port facilities by the tsunami attack (Tomita *et al.*, 2003). The large tsunami run-up heights of about 4 meters were recorded at the east side of Cape Erimo and Bansei-onsen located about 70 km northeast of the Cape Erimo, and 0.5–2.5 meters tsunami run-up heights were observed along the northeastern coast of Tohoku area (Tanioka *et al.*, 2004). Figure 1.1 shows the 2003 Tokachi-Oki earthquake epicenter, and locations of Hokkaido, Tohoku and Cape Erimo.

Figure 1.1: The 2003 Tokachi-Oki earthquake epicenter (star), and locations of Hokkaido, Tohoku and Cape Erimo.

The seismic waves, ocean bottom pressure fluctuations and other geophysical data of the 2003 Tokachi-Oki earthquake were captured by the cabled seafloor observatory

located right in the source region of the earthquake – the Japan Agency for Marine-Earth Science and Technology (JAMSTEC) deployed the observatory in 1999, just four years prior to the earthquake (Hirata *et al.*, 2002). The closest ocean-bottom seismometer (OBS) to the epicenter of the mainshock, KOBS1, is located approximately 30 km southeast from the epicenter. The other two OBSs, KOBS2 and KOBS3, are located within 100 km from the epicenter. Ocean bottom pressure data were collected by the pressure gauges PG1 (41.70°N, 144.44°E) and PG2 (42.24°N, 144.85°E) located at the depth 2283 m and 2248 m, respectively. The distances from PG1 and PG2 to the epicenter are 31.4 km and 81.8 km, respectively. Note that both the pressure gauges (PGs) are located within the source area of the tsunami (Hirata *et al.*, 2003). According to Nosov (2005), Dotsenko and Soloviev provided the following empirical formula to calculate the radius of tsunami source area:

$$lgR_{TS}[km] = 0.5M - 2.1 \tag{1.1}$$

where M is earthquake magnitude. The 2003 Tokachi-Oki tsunami source radius R_{TS} can be computed to be around 100 km ($M = 8.0$). This is consistent with the estimate made by Hirata *et al.* (2004) ($\sim 1.4\times10^4 km^2$), based on the observed tsunami travel times at 17 Japanese tide gauge stations. The earthquake epicenter, locations of ocean-bottom seismometers KOB1, KOB2 & KOB3 and pressure gauges PG1 & PG2 are shown in Figure 1.2. The area indicated by the dashed line denotes the estimated tsunami source.

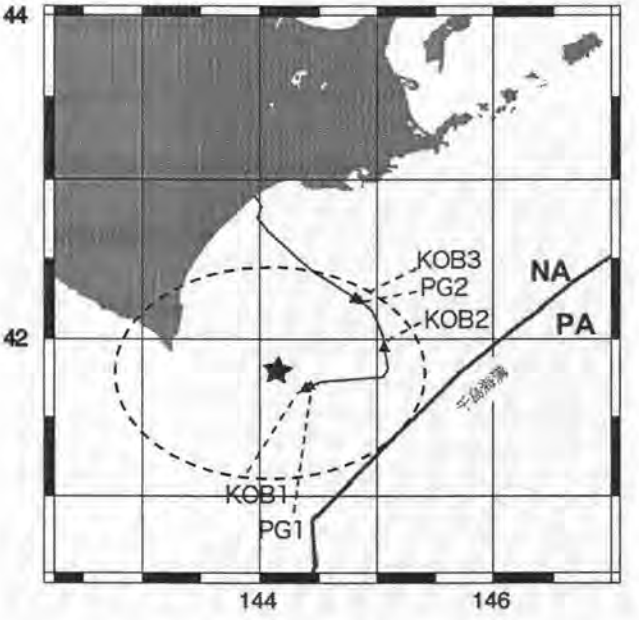

Figure 1.2: The 2003 Tokachi-Oki earthquake epicenter (star) and locations of ocean-bottom seismometers KOB1, KOB2 and KOB3 and pressure gauges PG1 and PG2. The estimated tsunami source area is enclosed by a dashed curve. (JAMSTEC, 2003).

The observed pressure variations at the pressure gages, PG1 and PG2 during the 2003 Tokachi-Oki earthquake mostly represent the existence of the normal elastic oscillations of compressible water and sediment layers. The co-seismic sea-bottom displacements can generate pressure waves associated with compression and expansion of the water column, namely acoustic waves. The acoustic waves due to fluid compressibility have vibrations along the wave.

This thesis is organized as follows: literature relevant to this study is reviewed in Chapter 2. Detailed analysis of the measured pressure data is given in Chapter 3. In Chapter 4, a one-dimensional numerical model is constructed to simulate the pressure wave propagation with the method of characteristics using the convenient finite-

difference scheme. Chapter 5 gives the analytical solutions for the natural frequencies of the pressure wave. Results and discussions are presented in Chapter 5 and conclusions in Chapter 6.

2 Literature Review

High seismicity characterizes the Kuril subduction zone, where the Pacific plate is subducting under the Eurasia plate at the Kuril Islands and Hokkaido, Japan (Figure 2.1). Large earthquakes ($Mw > 7.5$) have occurred here frequently. These earthquakes often generated tsunamis and struck the northwest Pacific coasts. Studies of earthquake and tsunamis are important to mitigate the natural hazard. In order to monitor seismicity, tsunamis, and other geophysical phenomena in the southern Kuril subduction zone, a permanent real-time geophysical observatory using a submarine electro-optical cable was developed and deployed at the continental slope of the southeast Kuril trench, southeast Hokkaido, Japan in July 1999.

Hirata *et al.* (2002) described the deep seafloor geophysical observatory off Kushiro and Tokachi. The geophysical observatory contains six bottom-sensor units: three ocean bottom broadband seismometers with hydrophone (OBSHs), two pressure gauges (PGs), and a cable end station. The sensor units are directly connected to the two land stations through a main electro-optical cable about 240km long with two branching units. The OBSHs (Figure 2.2. a) use a three-axis broad acceleration sensor, the PGs (Figure 2.2. b) (made by NEC Corporation) use a quartz pressure sensor and the cable end station (Figure 2.2. c) is equipped with a current meter, an acoustic Doppler current profiler (ADCP) and a CTD sensor, etc.

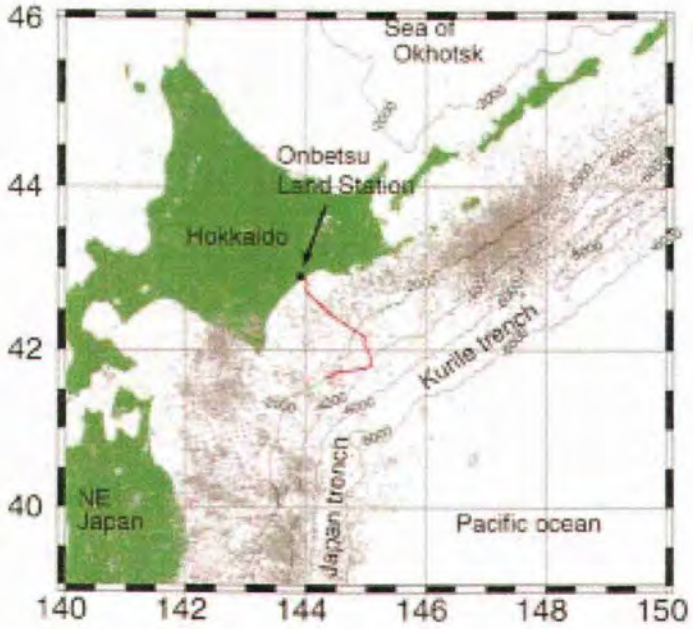

Figure 2.1: Seismicity map in the southern Kurile subduction zone. The red line represents the main electro-optical cable (Hirata, 2002).

(a)

(b)

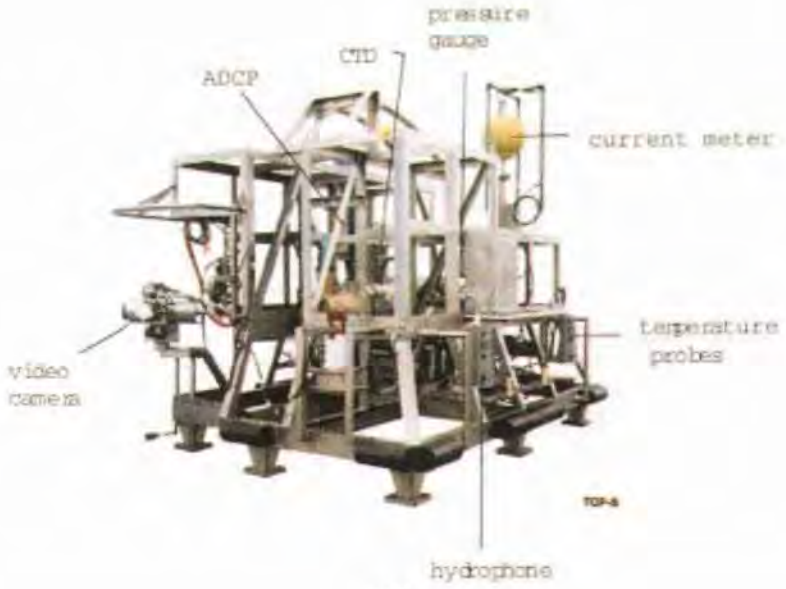

(c)

Figure 2.2: Ocean bottom broadband seismometer (a), Pressure gauge (b), and Cable end station (c) (Hirata, 2002).

Offshore detection of tsunami and storm surge before arriving at the coast is very important for coastal disaster reduction. Long term field observation by the GPS buoy deployed 2km off the Ofunato-Port (53m deep) started in 2001 (Kota *et al.*, 2001). On September 26, 2003 JST, the GPS buoy recorded the offshore tsunami caused by the 2003 Tokachi-Oki earthquake. The tsunami data obtained by the GPS buoy are consistent with the data taken by other instruments, e.g., JMA Ofunato-Port tide station and NOWPHAS coastal wave stations.

Yamanaka and Kikuchi (2003) investigated the source process of the 2003 Tokachi-oki earthquake by using teleseismic body wave (P-wave) and shear horizontal wave (SH-wave) data. They summarized the main source parameters as follows: total seismic moment ($Mo = 1.0 \times 10^{21} Nm$ or $Mw = 8.0$); (strike, dip, rake) = (230, 20, 109);

depth of initial break point = 25 km; total source duration = 40 seconds; and maximum slip = 5.8 m. They also estimated the fault slip distribution of this earthquake using the teleseismic body waves.

Yagi *et al.* (2004) constructed a detailed and stable source model of the 2003 Tokachi-oki earthquake using the teleseismic body wave data recorded at IRIS-DMC stations and the strong ground motion data obtained by K-NET (NIED). They also obtained that the total seismic moment is $Mo = 1.7 \times 10^{21} Nm$ ($Mw = 8.1$) and the total source duration is about 50 seconds.

Nagai *et al.* (2004b) reported the observed tsunami profiles caused by the 2003 Tokachi-Oki earthquake at 10 offshore wave gauges and 23 tide stations. Among the offshore wave gauges, five are newly developed Doppler-type Wave Directional Meter (DWDM), which is the principle seabed installed system of NOWPHAS (Nationwide Ocean Wave information network for Ports and HArbourS: see http://nowphas.org/) and is capable to obtain acoustic water surface fluctuation, seabed pressure fluctuation, and multi-layered horizontal current (Takayama *et al.*, 1994; Hashimoto *et al.*, 1996). One is the GPS buoy, which obtains water surface fluctuation with accuracy of cm order (Nagai *et al.*, 2003). The other four are either seabed Ultra-Sonic Wave gauge (USW), which can obtain acoustic water surface fluctuation, or Pressure-type Wave gauge (PW), which is able to record seabed pressure fluctuation. Comparison of offshore tsunami profiles and coastal tide station data were conducted based on wave-to-wave analysis and spectrum analysis.

NOWPHAS is Japanese wave observation and analysis system, which has been operated since 1970 by the Ports and Harbors Bureau of the Ministry of Land, Infrastructure and Transport, and its associated agencies including the Ports and Airports Research Institute (PARI) (Nagai *et al.*, 1994; Nagai *et al.*, 2002). NOWPHAS is very unique coastal wave information system in the world with capability to observe long period waves, because NOWPHAS wave observation system comprises seabed installed acoustic wave gauges, which are able to observe any frequency waves from short period waves to long period waves such as tsunami, storm surge and tides, if applying sufficient data acquisition and analysis (Nagai *et al.*, 2004a).

Tomita *et al.* (2004) investigated the characteristics of the 2003 Tokachi-Oki earthquake tsunami by means of the numerical simulations. Their numerical model is based on the horizontally two-dimensional nonlinear shallow water equations with the 600m grid system. The initial condition of the tsunami was estimated with the slip distribution provided by Yamanaka and Kikuchi (2003).

The two-dimensional nonlinear shallow-water equation can be written as:

Continuity equation

$$\frac{\partial \eta}{\partial t}+\frac{\partial M}{\partial x}+\frac{\partial N}{\partial y}=0 \tag{2.1}$$

Momentum equations (2-D)

$$\frac{\partial M}{\partial t}+\frac{\partial}{\partial x}\left(\frac{M^2}{D}\right)+\frac{\partial}{\partial y}\left(\frac{MN}{D}\right)+gD\frac{\partial \eta}{\partial x}+\frac{f}{D^2}M\sqrt{M^2+N^2}=0 \tag{2.2}$$

$$\frac{\partial N}{\partial t}+\frac{\partial}{\partial x}\left(\frac{MN}{D}\right)+\frac{\partial}{\partial y}\left(\frac{N^2}{D}\right)+gD\frac{\partial \eta}{\partial y}+\frac{f}{D^2}N\sqrt{M^2+N^2}=0 \tag{2.3}$$

where

$$M = Du\,,\ N = Dv\,,\ D = h + \eta \tag{2.4}$$

u and v are the horizontal velocities in the x and y directions, M and N are the discharge fluxes in the x and y directions, h is the undisturbed water depth, η is the water surface displacement, D is the total water depth, g is the gravitational acceleration, and f is the bottom friction factor. These equations were solved by the finite difference method (FDM) with the leap-frog scheme in time and the staggard mesh in space.

Most of the tsunami studies have been conducted based on the incompressible fluid theory. However the role of water compressibility in the tsunami problem has been discussed many times. Kajiura (1970) pointed out that when the sea bottom is uplifted during submarine earthquakes; the energy is transferred from the solid bottom to the overlying water by generating compressional waves (acoustic waves) in the water and then partly converted to gravity waves. He examined the relative importance of acoustic waves and gravity waves in terms of the generated energy using a 1-D model (only the vertical direction is considered with an assumption of a very large horizontal dimension of the bottom uplift), and derived the ratio of the acoustic wave energy E_1 and the gravity wave energy E_2

$$\frac{E_1}{E_2} = \frac{2c}{g\tau} \tag{2.5}$$

where c is the acoustic speed in water (1500 m/s), g is the gravity acceleration, and τ is the duration of bottom displacement (assume the bottom displacement velocity is

constant for the duration of $[0, \tau]$ and zero otherwise). Equation (2.5) indicates that the considerable part of the energy transferred from the bottom to the ocean exists not in the gravity waves but in the acoustic waves for a very short duration of the bottom displacement.

Nosov (1999, 2000) showed that the water compressibility must be considered for the process of tsunami generation by bottom displacements during submarine earthquakes; however the processes of tsunami propagation and run-up can be correctly studied in incompressible fluid. The behavior of a real compressible ocean differs from that of an incompressible one mostly by the formation of elastic oscillations of water layer. The significant feature of the surface disturbance of compressible water is the appearance of high-frequency vertical surface oscillations, which are a consequence of compressive and rarefaction waves traveling back and forth between the hard bottom and the water surface. The resonant frequencies of these oscillations (normal modes) are given by

$$f_k = (1+2k)c/4H \text{ , for } k = 0,1,2,... \tag{2.6}$$

where c is the acoustic speed in water and H is the water depth. The dominant frequency is the lowest mode $f_0 = c/4H$.

Ohmachi *et al.* (2001) carried out a 2-D numerical simulation of tsunami considering dynamic seafloor displacement due to an oceanic earthquake. The simulation consists of two steps: the first step is to simulate the dynamic seafloor displacement due to a seismic faulting by applying the boundary element method (BEM); the second step is to simulate generation of the seawater disturbance with the finite difference method (FDM). For the second step, the water is regarded as a compressible fluid, and the

numerical simulation is conducted using the extended subtractive optimally localized averages (SOLA) method (a numerical solution algorithm for transient fluid flows) in 3-D. From the results, they obtained the relation between the sea floor pressure and water surface elevation with changing fault parameters and water depth, and developed a simple procedure to evaluate the tsunami component from the sea floor pressure variations following an earthquake.

Nosov (2005) proved the existence of elastic oscillations of water column by the sea bottom pressure variations recorded in the tsunami source area during the 2003 Tokachi-Oki earthquake and estimated the amplitude, velocity, and duration of the co-seismic bottom displacement from the pressure data. He also presented that better agreement between the dominant frequency of the observed bottom pressure variations and theoretically calculated frequency range was reached considering coupled elastic oscillations of water and sediment layers.

3 Analyses of Measured Pressure Data

3.1 Estimation of Seafloor Uplift

Time series of pressure variations registered by PG1 and PG2 from 00:00:00 to 23:59:59, Sep.26, 2003 (JST) are plotted in Figure 3.1. The pressure data are provided by Hirata (2004). The data sampling rate was 10 Hz, which is fast enough to detect not only tsunami generation, but also transient pressure waves. Figure 3.2 shows the time histories of pressure variations at PG1 and PG2 using expanded pressure scale. It is clearly seen that static pressure changes after the earthquake are $\Delta P1 \approx 4KPa$ and $\Delta P2 \approx 1.5KPa$. This shift in pressure must be caused by the residual vertical ocean bottom displacement (ΔH) resulted from the fault rupture of the earthquake. Hydrostatic computation:

$$\Delta H = \Delta P / \rho g \tag{3.1}$$

where ρ is the water density and g is the gravity acceleration, yields the vertical bottom displacements $\Delta H1 \approx 0.4m$ and $\Delta H2 \approx 0.15m$ at PG1 and PG2, respectively (Nosov, 2005).

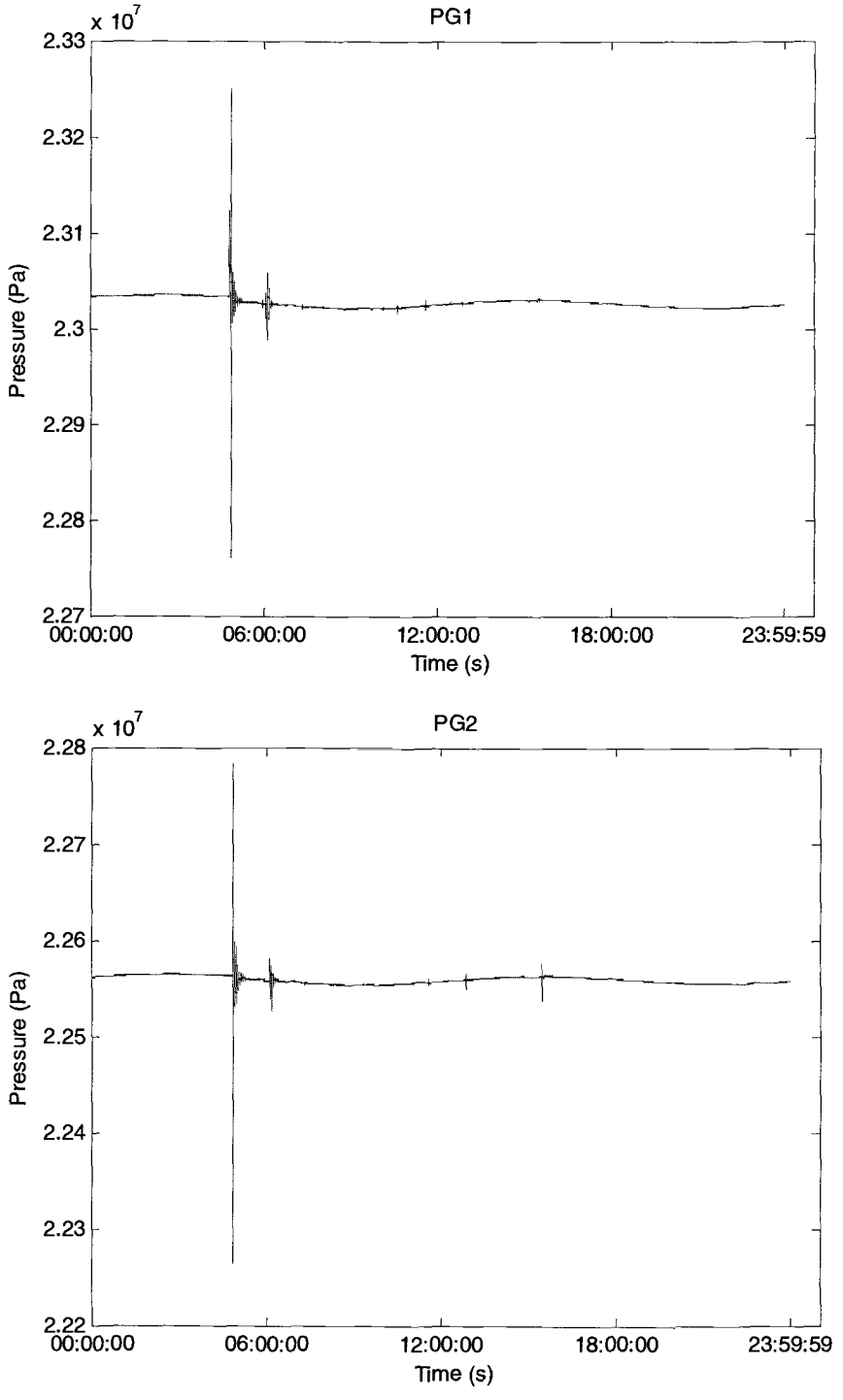

Figure 3.1: Time histories of the pressure variations at PG1 and PG2 from 00:00:00 to 23:59:59.

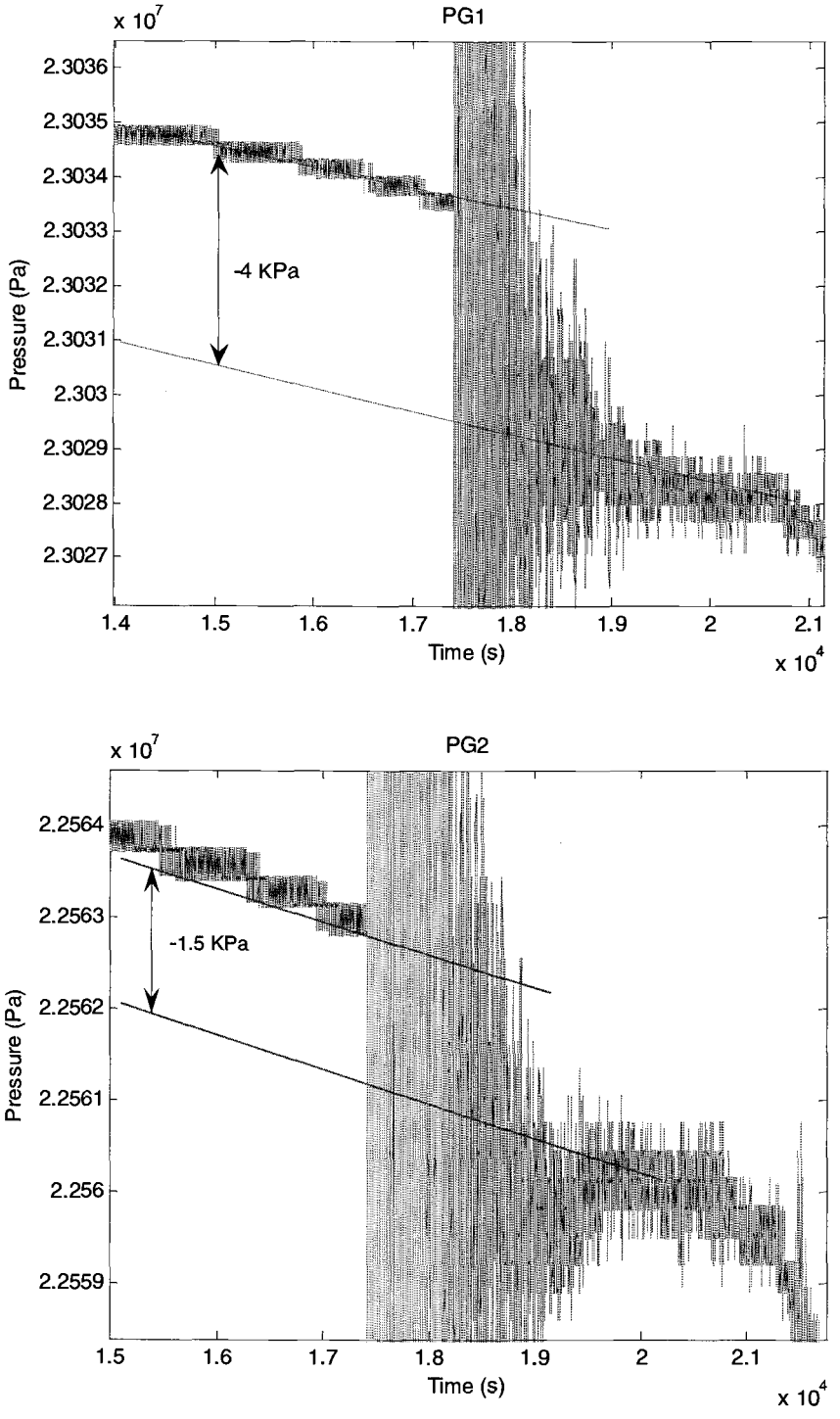

Figure 3.2: Time histories of pressure variations at PG1 and PG2 in an expanded pressure scale and static pressure changes due to residual bottom uplift.

The estimation of co-seismic uplift of the sea floor was refined by Hirata (2004) with the "static" temperature correction necessary to the pressure sensors: Hirata reported that the co-seismic uplift at PG1 and PG2 is 36 cm and 14 cm, respectively, which are slightly lower than the values without the temperature correction. Hirata (2004) further refined the data by removing the "transient" thermal response of the sensors; then the net uplift becomes 33 cm and 3 cm at PG1 and PG2, respectively. Figure 3.3 shows the estimation of co-seismic uplift at PG1 and PG2 given by Hirata (2004). In this figure, A denotes the duration of 30 minutes before the mainshock and B is 10 minutes around the second zero-cross. Two parallel lines are fitted to the data in the durations of A and B; then the offset value $\Delta D = dA - dB$ was obtained as the co-seismic uplift (Hirata, 2004).

The data shown in Figure 3.3 were obtained after low-pass filtering the raw data. The data clearly demonstrate that the co-seismic sea-floor displacements are not monotonic. At PG1, the displacement started by a fast uplift, followed by a brief subsidence (~ 1 minute), then gradual uplift in approximately 12 minutes to the settlement of the upward displacement of 33 cm. The similar pattern can be found at PG2, but the subsidence is much longer (~ 10 minutes) and the final uplift was much faster (~ 5 minutes). Also note that Figure 3.3 indicates that the seafloor displacements also occurred continuously after the mainshock; the displacements around 6:00 must be related to the first aftershock shown in Figure 3.1.

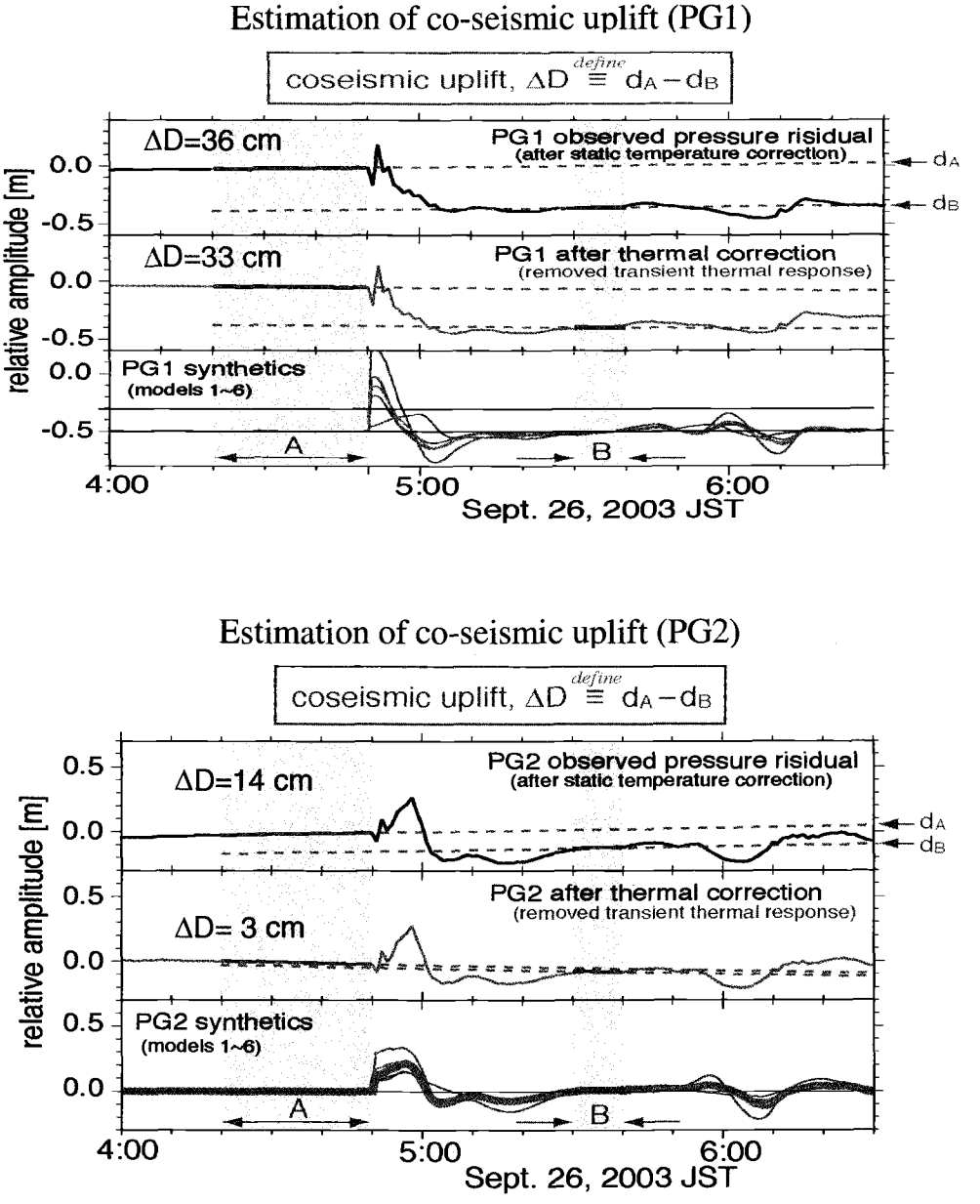

Figure 3.3: Estimation of co-seismic uplift at PG1 and PG2 (Hirata, 2004).

3.2 Band-pass Filtering of Pressure Data

Analyses of low-pass-filtered data provided the time history of seafloor displacement as shown in Figure 3.3 (Hirata, 2004). We are also interested in higher-frequency components of the data. At the outset, we conjecture that the high-frequency fluctuation of pressure data must be related to pressure waves associated with compression and expansion of the water column, namely acoustic waves. To extract the acoustic wave data from the raw data, we apply a band-pass filter. Figure 3.4 is an illustration of the characteristic curve of a hypothetical band-pass filter. The cutoff frequencies f_1 and f_2 are the frequencies at which the output signal magnitude falls to half of its level at f_0, the center frequency of the filter. The value of $f_2 - f_1$, expressed in hertz (Hz), is called the filter bandwidth. The range of frequencies between f_1 and f_2 is called the filter passband.

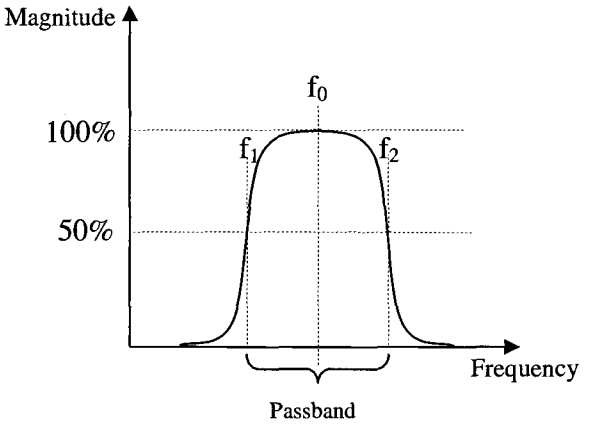

Figure 3.4: The frequency response of a hypothetical band-pass filter.

For the raw pressure data at PG1, we used a 5^{th} order Butterworth band-pass filter with the cutoff frequencies $f_1 = 0.01$ Hz and $f_2 = 2$ Hz. The frequency response of this

band-pass filter is shown in Figure 3.5. The filter eliminates the gradual pressure variations; hence the data will be de-mean and de-trended. The dominant frequency of acoustic waves in a water column of 2283m (i.e. water depth at PG1) is roughly 0.16 Hz; hence the filter should capture the acoustic waves while eliminating high-frequency noise. The time series of the filtered pressure data at PG1 from 00:00:00 to 23:59:59 are presented in Figure 3.6.

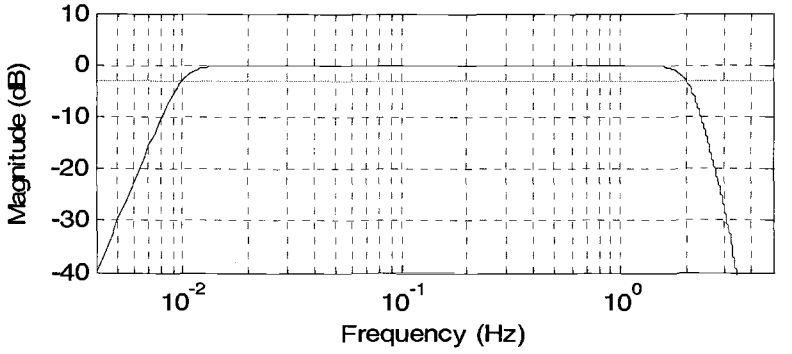

Figure 3.5: The frequency response of a 5th order Butterworth band-pass filter with the cutoff frequencies $f_1 = 0.01$ Hz and $f_2 = 2$ Hz.

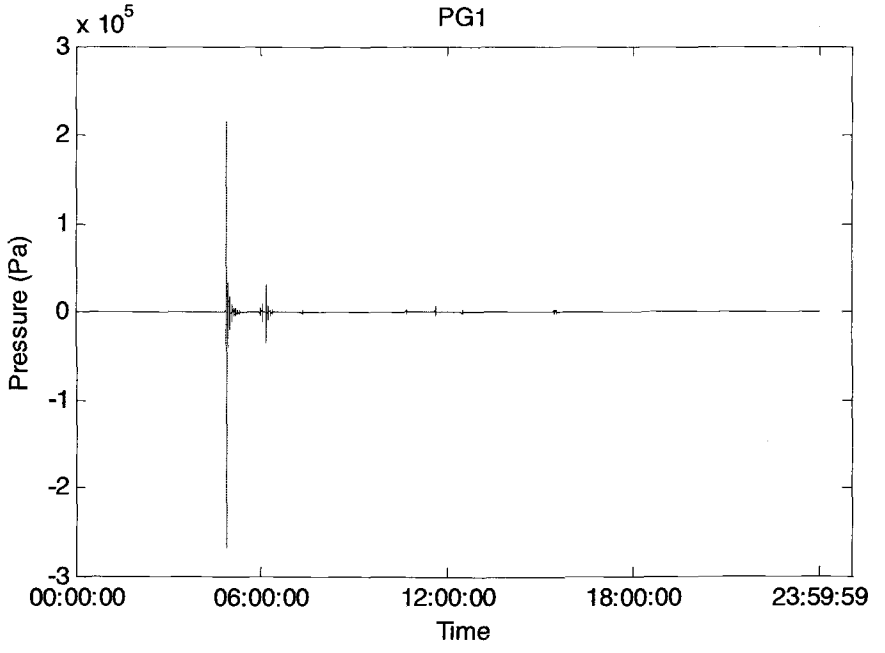

Figure 3.6: Time histories of the filtered pressure data at PG1 from 00:00:00 to 23:59:59; the band-pass filter used is shown in Figure 3.5.

3.3 Analysis of Pressure-wave Amplitude Attenuation

The raw pressure data at PG1 were re-plotted in Figure 3.7(a) for the duration of 8000 seconds (roughly 2 hours and 13 minutes) starting at 4:43:20 (Note that the mainshock occurred at 4:50:06). In the figure, we can see a few of aftershocks subsequently occurred and the largest aftershock followed about one hour after the mainshock. It is seen that the amplitude of pressure fluctuations attenuates quickly after every shock. The attenuation patterns can be more explicitly observed in the band-pass filtered pressure data shown in Figure 3.7(b).

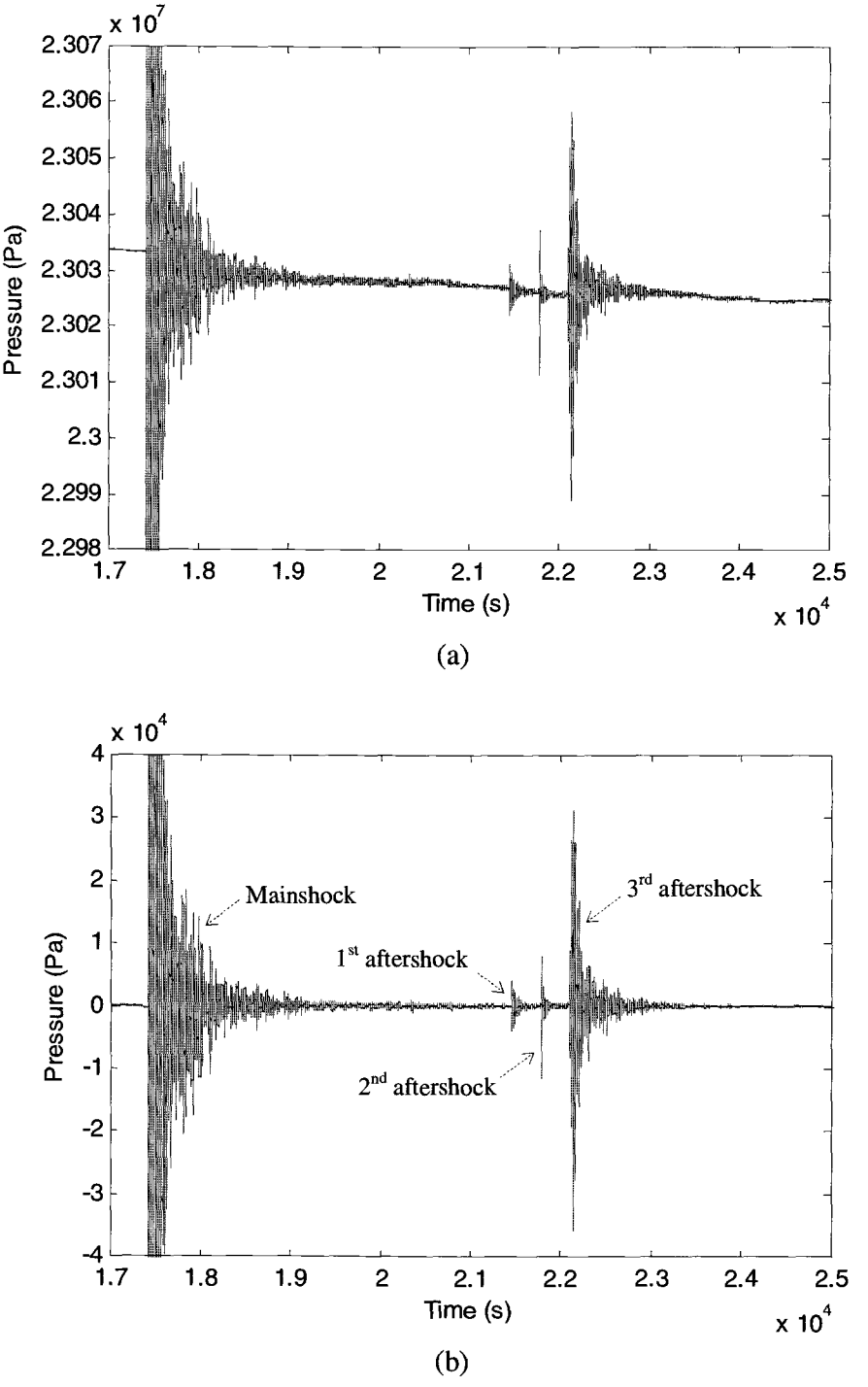

Figure 3.7: Time series of pressure data at PG1 for the duration of 8000 seconds starting at 4:43:20. (a) raw data; (b) filtered data.

Figure 3.8 presents time histories of the filtered pressure data for the duration of 1000 seconds after the mainshock, for the duration of 200 seconds after the 1st aftershock, for the duration of 250 seconds after the 2nd aftershock, and for the duration of 1000 seconds after the 3rd aftershock. Each time series begins from the start of the corresponding local shock. The starting time and duration for each shock are listed in Table 3.1.

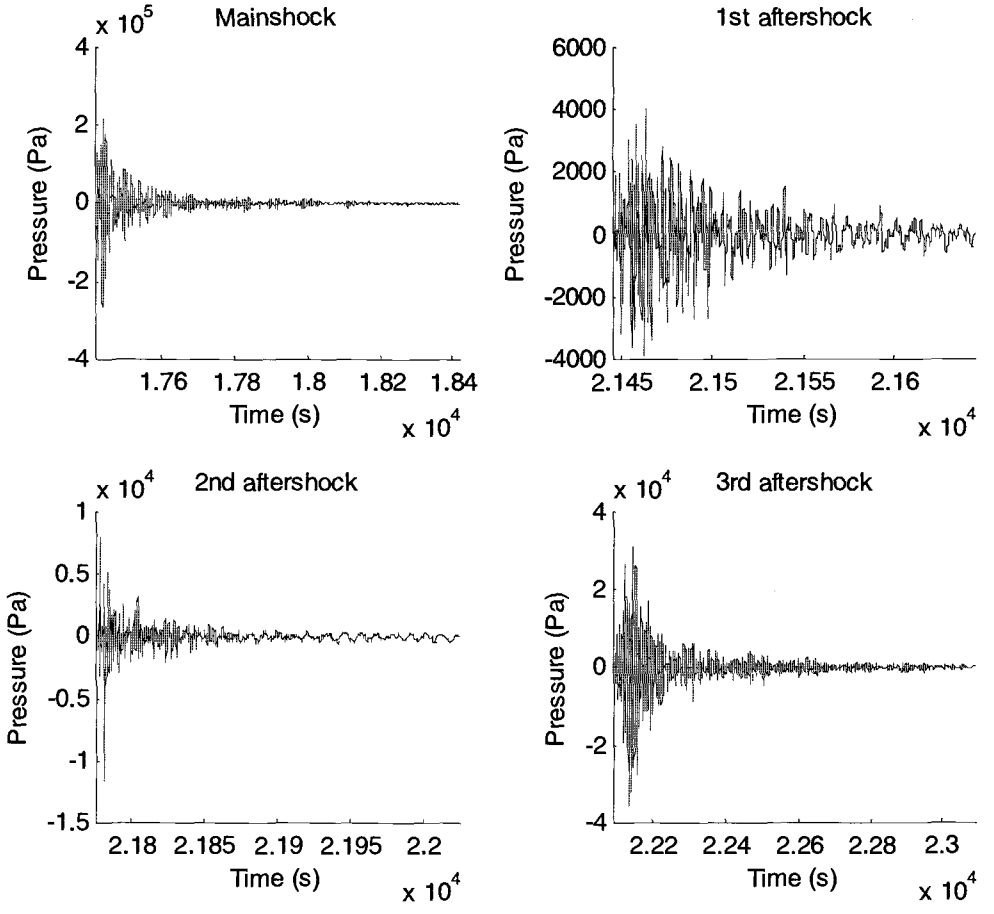

Figure 3.8: Time histories of filtered pressure data at PG1 for mainshock and three following aftershocks.

Table 3.1: The starting time and duration for each shock.

Shocks at PG1	Starting time (seconds)	Time duration for study (seconds)
Mainshock	17416	1000
1st aftershock	21445	200
2nd aftershock	21775	250
3rd aftershock	22090	1000

To investigate the characteristic of the attenuation of pressure wave, we first calculate the peak-to-peak amplitude (P-P) of the pressure wave, and then estimate the e-folding time, because the attenuation is often exponential in many natural systems (the term "e-folding time" is the time interval in which an exponentially growing or attenuating quantity increases or decreases by a factor of e: it is used as a representative time scale for an exponentially varying phenomenon). To calculate peak-to-peak amplitudes of the pressure wave, we need to find the local maxima and minima first. However, there are many small spikes generated by noise in the data and these spikes are not what we want for calculating the peak-to-peak pressure-wave amplitudes. To eliminate the small spikes as much as possible while retaining the peaks we need, the following procedure was implemented. First, we set a running window with the duration of $2\Delta t$, as shown in Figure 3.9. If the pressure P at time $t = t_0$ is the maximum or minimum in the interval of $[t_0-\Delta t, t_0+\Delta t]$, we will choose this peak at t_0 as the maximum or the minimum peak. The value of peak-to-peak amplitude is equal to the difference between the adjacent maximum and minimum peaks. The time corresponding to the

peak-to-peak pressure-wave amplitude is assigned as the average time of the adjacent maximum and minimum peaks.

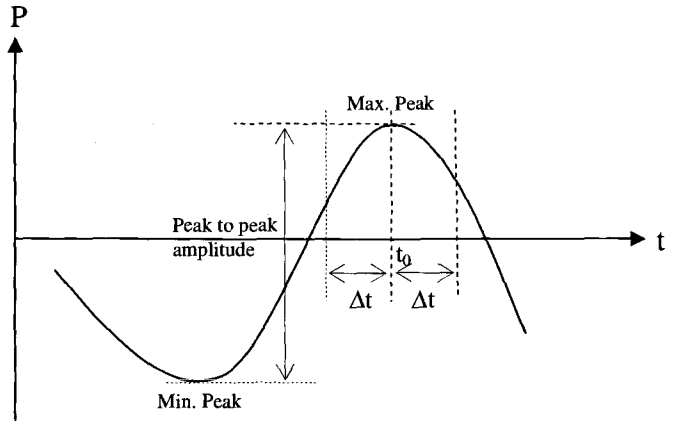

Figure 3.9: Sketch of the peak to peak amplitude.

Using the window size of $2\Delta t = 2$ seconds (20 data points), temporal variations of the peak-to-peak amplitudes were determined and presented in Figure 3.10 for the mainshock, the 1st aftershock, the 2nd aftershock and the 3rd aftershock. Note that each plot in Figure corresponds to the time series shown in Figure 3.8. In the figure, the green solid line denotes the peak-to-peak amplitude plotted in Logarithm scale and the blue dashed line represents the envelope of the peak-to-peak amplitudes.

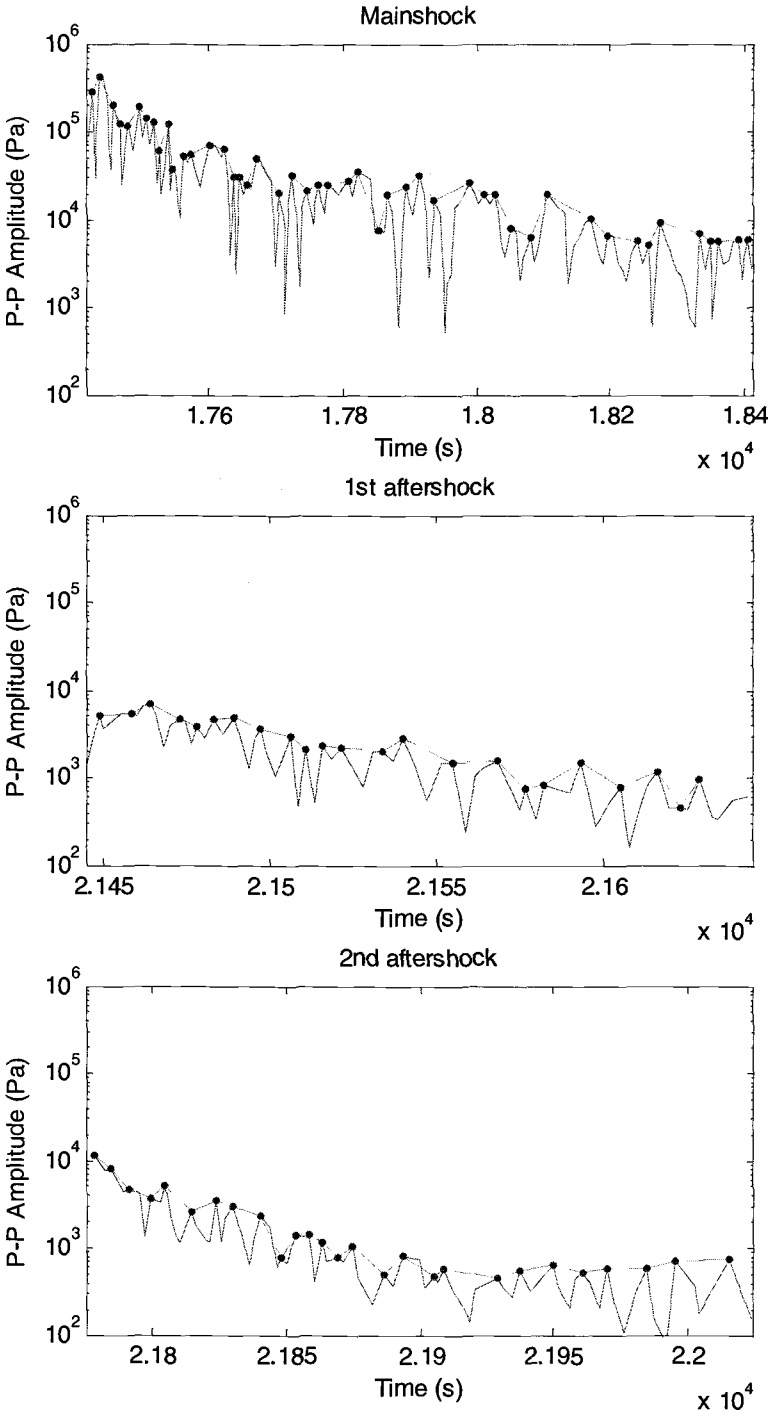

Figure 3.10: Temporal variations of the peak to peak amplitudes (solid) for the four shocks with the window size $2\Delta t = 2$ seconds and the envelopes of the peak-to-peak amplitudes (dashed).

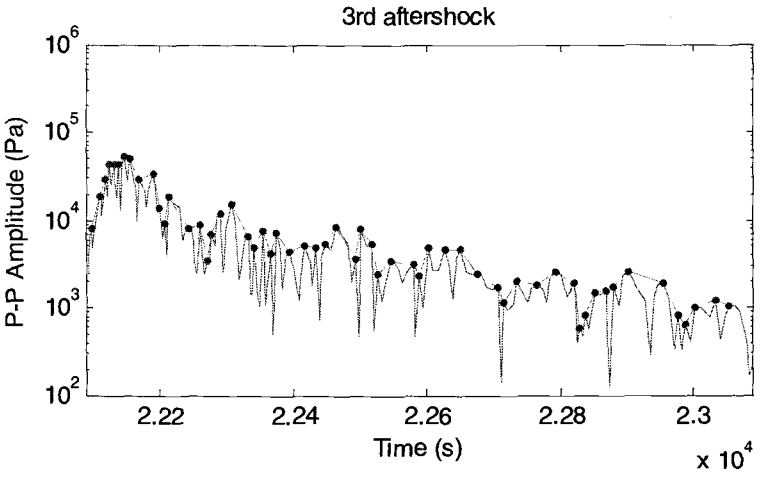

Figure 3.10 (Continued)

To compare the attenuation rates of the four shocks, the four envelope curves in Figure are superimposed and presented in Figure 3.11. The time origin in the figure corresponds to the time of the highest peak for each envelope. For the mainshock and the 3rd aftershock, it can be seen that the attenuation for both events is faster in the first 150 seconds or so and then slows down, while the pressure fluctuation is order-of-magnitude greater for the mainshock than for the 3rd aftershock. The similar attenuation rate can be observed in the first 150 seconds for the other two events (the 1st and 2nd aftershocks). Using linear regression to the semi-log plots of Figure 3.11 for the first 150 seconds, straight lines for the best fit are drawn in Figure 3.11. The e-folding time of the attenuation was computed for each event. In the semi-log plot, the e-folding time (Te) can be calculated by

$$Te = 1/(k \ln 10) \tag{3.2}$$

where k is the slope of the straight line. Applying the formula to the straight lines in Figure 3.11, we can get the e-folding time for each shock, which is listed in Table 3.2.

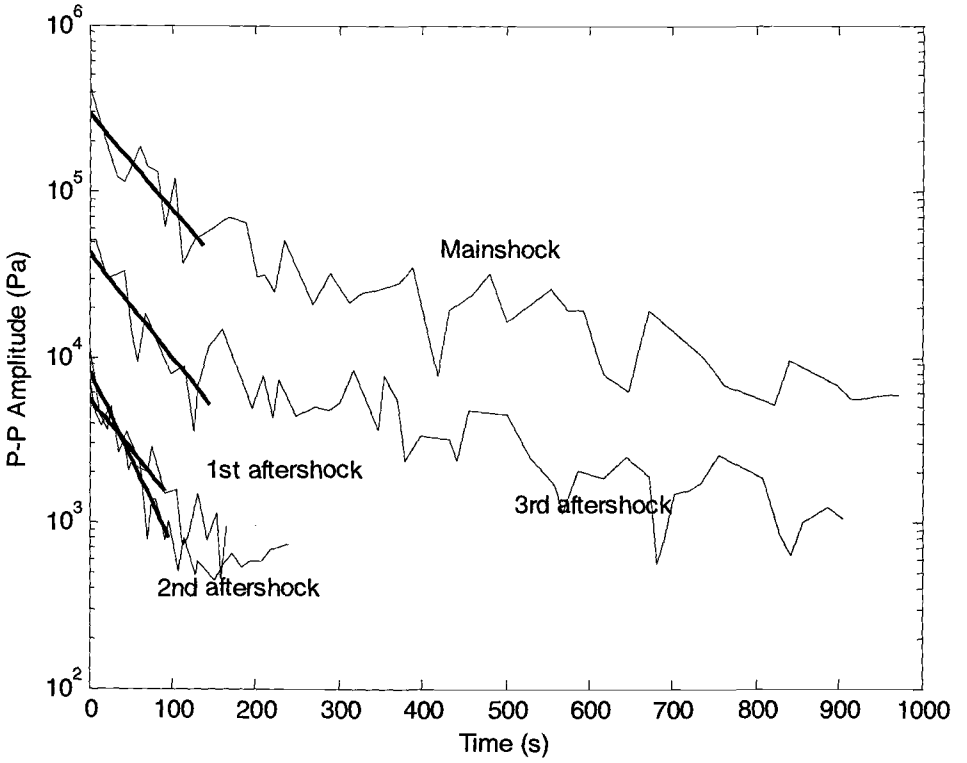

Figure 3.11: Envelopes of the peak-to-peak amplitudes (semi-log plots) for the mainshock and the next three aftershocks (thin solid lines). The thick straight lines are the best-fitting curves of the envelopes for the first 150 seconds using linear regression. The time origin corresponds to the time of the highest peak for each envelope.

Table 3.2: The e-folding times for the mainshock and the following three aftershocks.

Shock	Mainshock	1st aftershock	2nd aftershock	3rd aftershock
e-folding time (s)	75.4	70.9	41.5	67.9

For the acoustic pressure waves generated at the same position, the attenuation characteristic should be similar for the mainshock and aftershocks, that is, the e-folding times should be similar. Table 3.2 indicates that the e-folding times for the mainshock, 1st aftershock and 3rd aftershock just have a little difference, but for the 2nd aftershock, the

e-folding time is much shorter than other events: the attenuation for the 2nd aftershock is much quicker than other three events. The different decay rate of the 2nd aftershock might be due to a different source mechanism; such as the rupture of a very small area or not occurred at PG1 but somewhere nearby.

3.4 Application of Complex Demodulation Method

We now focus on temporal variation of pressure fluctuations (the band-pass filtered data) caused by the mainshock: the 2400 seconds time history is shown in Figure 3.12. The time origin corresponds to the start of the mainshock. Figure 3.13 presents the expanded plot of this time series up to 1000 seconds, which indicates the formation of amplitude modulations. The complex demodulation method (CDM) was applied to study the low frequency modulation of the carrier-frequency component.

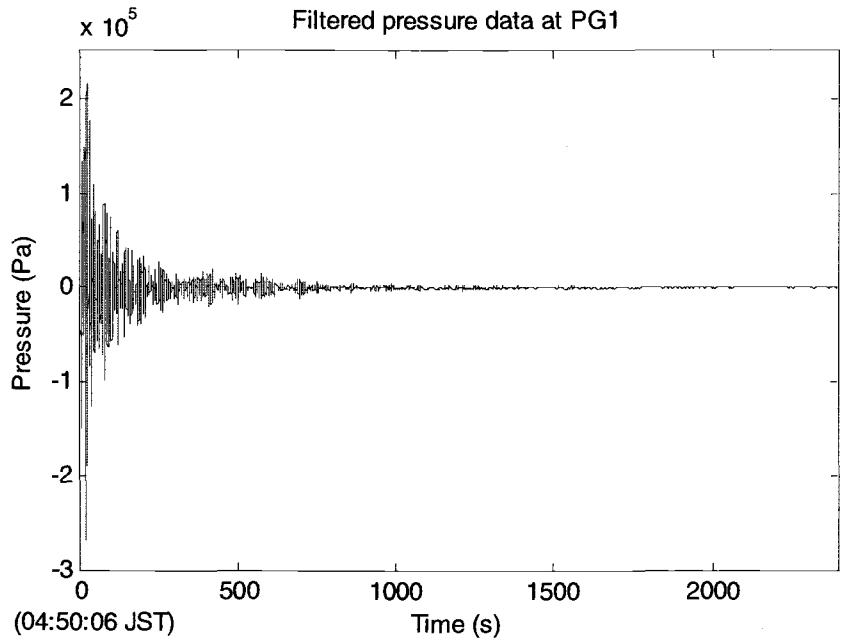

Figure 3.12: 2400s time history of the band-pass filtered pressure data at PG1 (The time origin corresponds to the start of the mainshock).

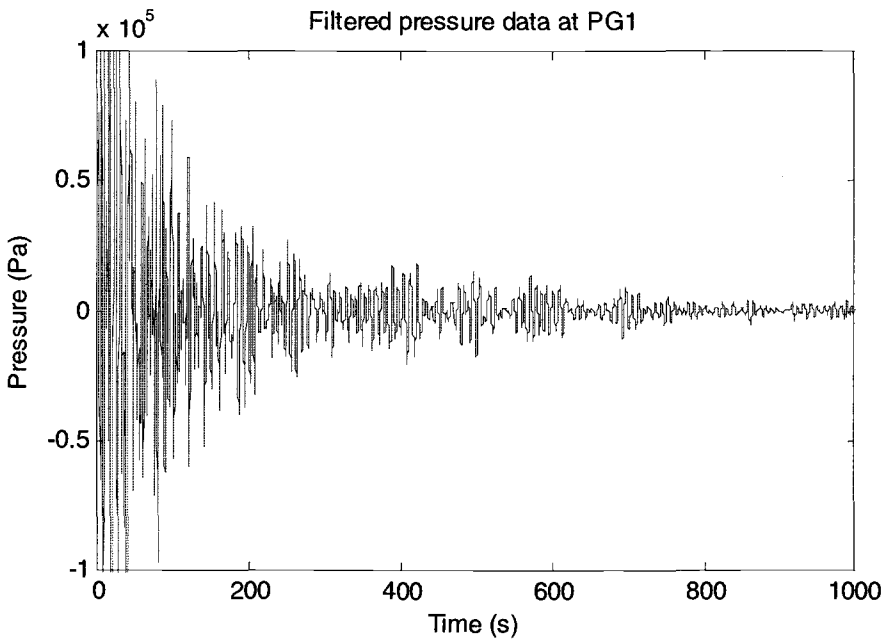

Figure 3.13: Expanded plot of the time history of the band-pass filtered pressure data at PG1 up to 1000 seconds.

Suppose that a signal $y(t)$ contains a perturbed component of the form

$$x(t) = A(t)\cos(2\pi f_s t + \delta) \tag{3.3}$$

where $A(t)$ is a slowly varying amplitude or amplitude modulation, f_s is the carrier frequency and δ is the initial phase. Consider the time series $y(t)$ represented by $x(t)$ and $z(t)$ of the form

$$y(t) = x(t) + z(t) \tag{3.4}$$

where $z(t)$ is the remainder components that make up the time series $y(t)$. Multiplying the signal $y(t)$ by an oscillation $\{\exp(-2\pi i f_m t)\}$ of demodulation frequency f_m yields

$$d(t) = y(t)e^{-2\pi i f_m t} = \frac{A(t)}{2}\left[e^{2\pi i(f_s - f_m)t + i\delta} + e^{-2\pi i(f_s + f_m)t - i\delta}\right] + z(t)e^{-2\pi i f_m t} \tag{3.5}$$

where $d(t)$ is the demodulated signal, which shifts the spectrum of the signal $y(t)$ to lower frequency by an amount f_m.

If $d(t)$ is operated with an ideal low-pass filter of cutoff frequency $f_c < f_m$, then only spectral components in the range $[-f_c, f_c]$ will be retained. Assume $f_m \approx f_s$, so the difference frequency term $(f_s - f_m)$ is the only component in $d(t)$ within this range. After the low-pass filter operation on $d(t)$, the result can then be expressed as

$$D(t) = \frac{A(t)}{2}e^{2\pi i(f_s - f_m)t + i\delta} \tag{3.6}$$

The low-pass filter is critical for complex demodulation. To avoid the distortion of signals within the pass band, the ideal low- pass filter should have a flat frequency response and have no ripple within the pass band. The most important filter parameter is

the cutoff frequency f_c. The choice of the cutoff frequency should be high enough to pass the wanted low frequency components ($\frac{A(t)}{2}e^{2\pi i(f_s-f_m)t+i\delta}$), and low enough to reject the unwanted high frequency components ($e^{-2\pi i(f_s+f_m)t-i\delta}$ and $z(t)e^{-2\pi i f_m t}$). To satisfy these requirements, f_c is usually chosen to be in the range of $[\Delta f/2, f_m]$, where Δf is the width of the peak at frequency f_m in power spectrum.

Let

$$\phi_r(t) = 2\pi(f_s - f_m)t + \delta \tag{3.7}$$

then, $D(t)$ can be expressed as

$$D(t) = \frac{A(t)}{2}e^{i\phi_r(t)} \tag{3.8}$$

The slowly changing phase $\phi_r(t)$ comes from the slight difference between the demodulation frequency f_m and the carrier frequency f_s. The time–dependent amplitude $A(t)$ and relative phase $\phi_r(t)$ can be obtained by taking twice the magnitude of $D(t)$ and by taking the arc tangent of the ratio of the imaginary part to real part of $D(t)$, respectively. The aim of complex demodulation is to extract approximations to the series $\{A(t)\}$ and $\{\phi_r(t)\}$. The time derivative of $\phi_r(t)$ is a correction to the specified demodulation frequency f_m. Then the carrier frequency f_s can be estimated by using

$$f_s = f_m + \frac{1}{2\pi}\frac{d\phi_r(t)}{dt} \tag{3.9}$$

Positive (or negative) values of the time derivative of $\phi_r(t)$ correspond to the situation where the local carrier frequency f_s is higher (or lower) than f_m. The derivative of the phase is computed numerically by finite difference. Since typical treatment is to wrap the relative phase result $\phi_r(t)$ is in the range of $[-\pi, \pi]$, as shown in Figure 3.14(a), there are discontinuities appearing as spikes in the plot of the derivative of the phase when the phase jumps from $-\pi$ to π. In order to avoid these spikes, we can compute the derivative of the phase function without wrapping around the fixed 2π interval. The unwrapped phase is shown in Figure 3.14(b).

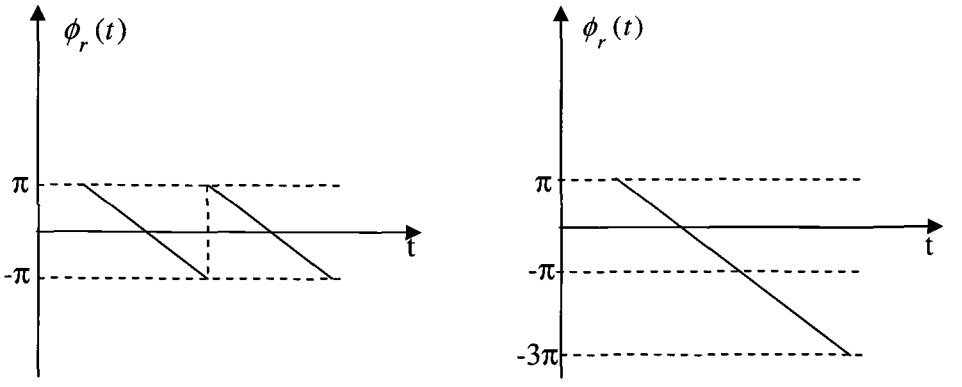

Original phase plot
(a)

Unwrapped phase plot
(b)

Figure 3.14: Sketch of unwrapping the phase function.

The first step of CDM is to estimate the demodulation frequency f_m. The demodulation frequency can be estimated from the dominant peak frequency found in the power spectra of the pressure fluctuation data shown in Figure 3.12. Figure 3.15 presents the periodogram of the data shown in Figure 3.12. The periodogram is obtained by

taking the discrete Fourier transform of the auto-covariance function of the time series and the power spectral density (PSD) can be derived by smoothing the periodogram. With a moving average of length 60, i.e., the window size of 61 points, the periodogram shown in Figure 3.15 was smoothed to obtain the spectrum of the pressure data at PG1 (The pressure data are shown in Figure 3.12). From the spectrum (Figure 3.16), it was found that the dominant peak frequency is around 0.148 Hz.

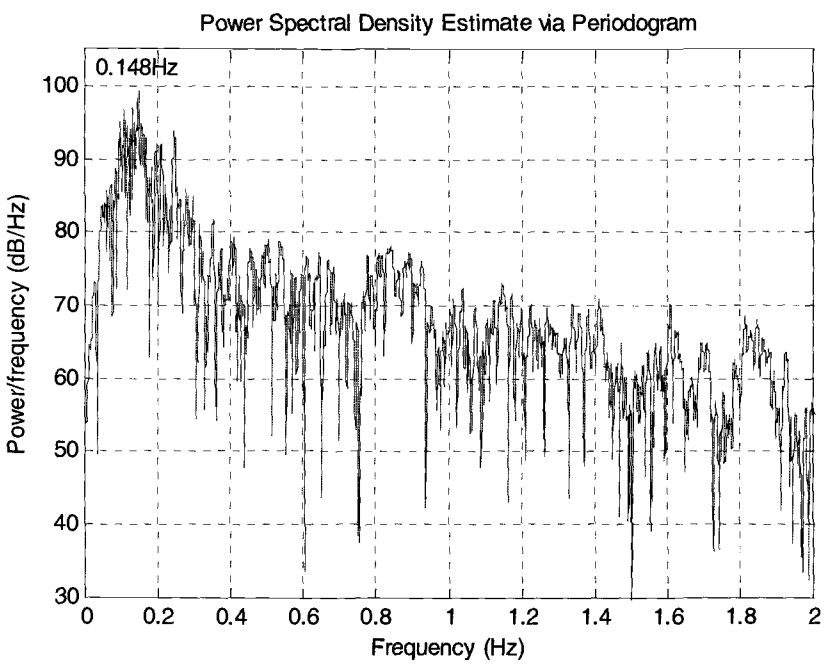

Figure 3.15: Periodogram of the filtered pressure data at PG1 shown in Figure 3.12; Δf = 1/2400 Hz.

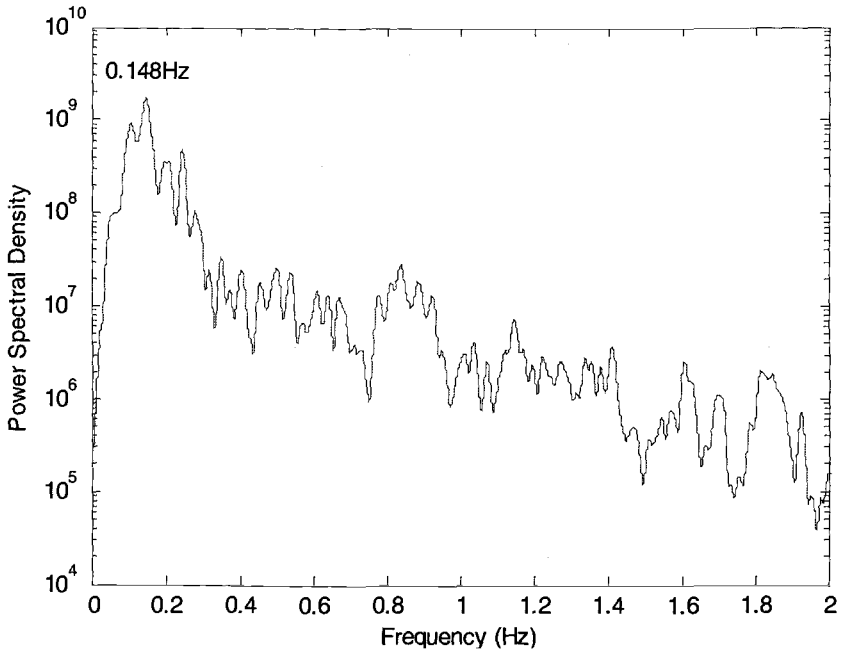

Figure 3.16: Power spectrum of the filtered pressure data at PG1 shown in Figure 3.12 with a moving average of length 60; $\Delta f = 1/2400$ Hz.

In order to keep track of the variation in peak frequency in the duration of 2400 seconds, the power spectra were computed in segmented time intervals. Since the mainshock lasted about 40 seconds, we start the computation from t = 50 seconds. Figure 3.17 shows a series of the resulting spectra in segmented time intervals. The dominant peak frequencies in the spectra and the corresponding time intervals are listed in Table 3.3. The results in Table 3.3 indicate that the dominant peak frequency is fairly constant varying between 0.120 and 0.133 Hz except the very early and very late stages of the pressure fluctuations. It suggests that there is one dominant physical mechanism to sustain the regular pressure fluctuations after seafloor shaking by the earthquake. On the other hand, for the application of complex demodulation method, it may be more

effective to use the frequency of the dominant component in each segment in order to extract temporal variations of the amplitude and the relative phase.

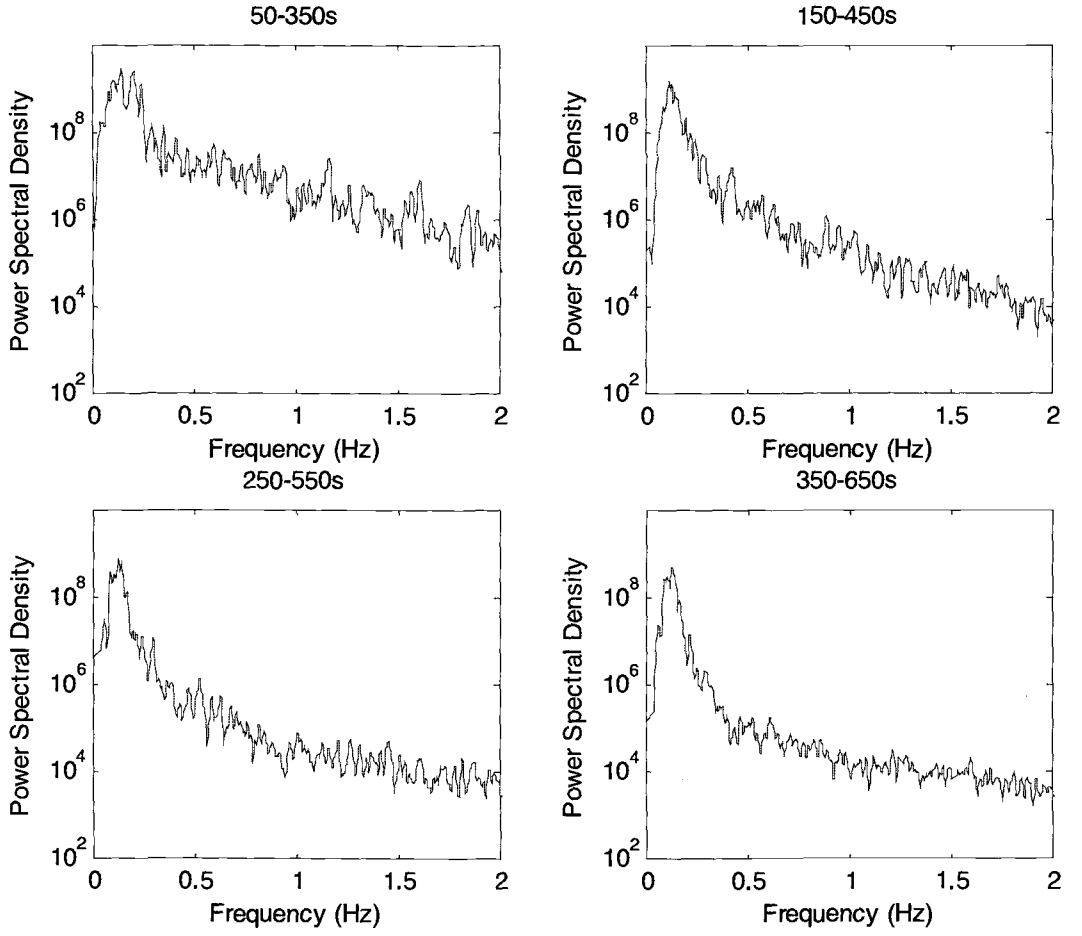

Figure 3.17: A series of the resulting spectra for the filtered pressure data in segmented time intervals of 300 seconds.

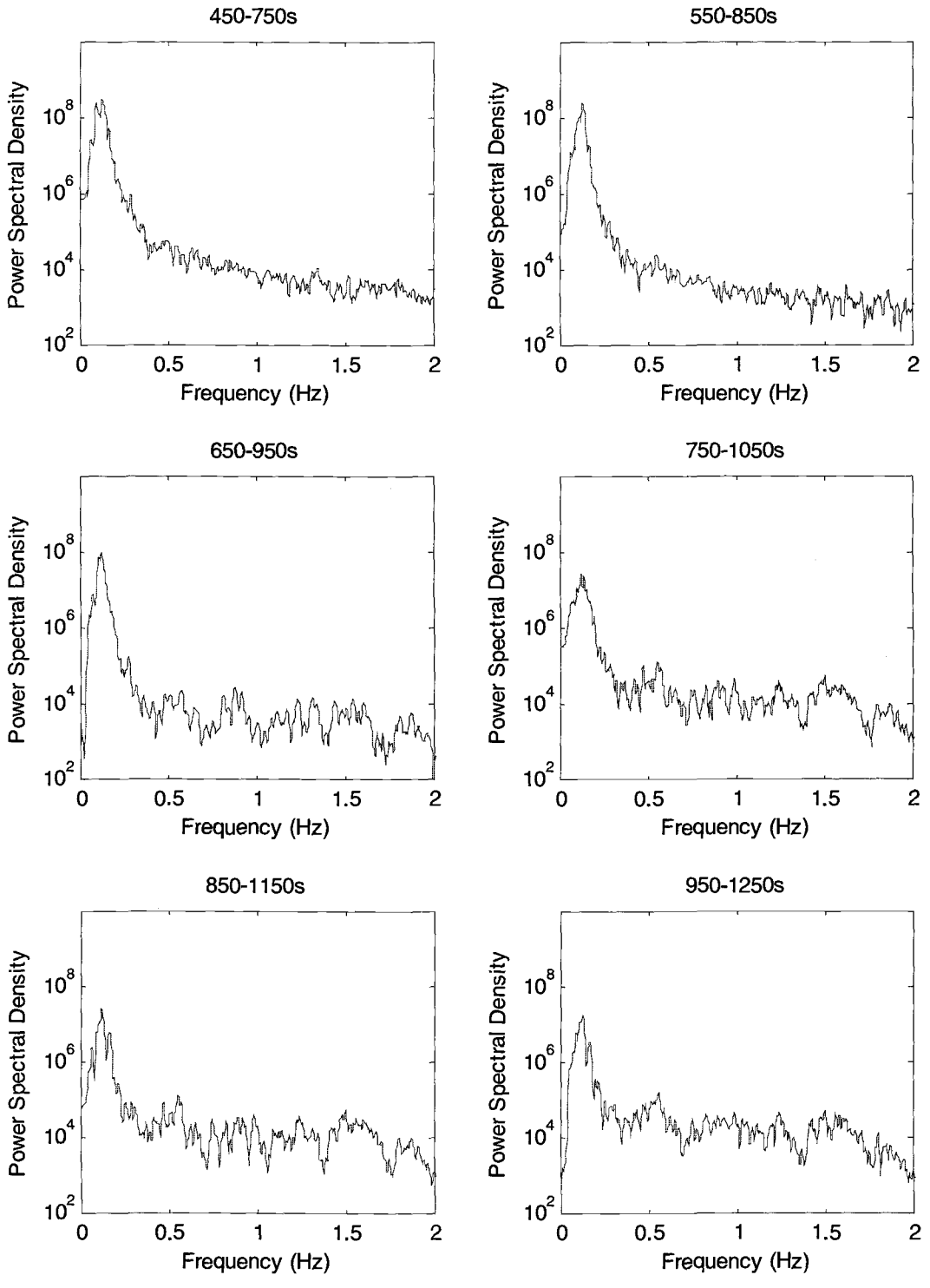

Figure 3.17 (Continued)

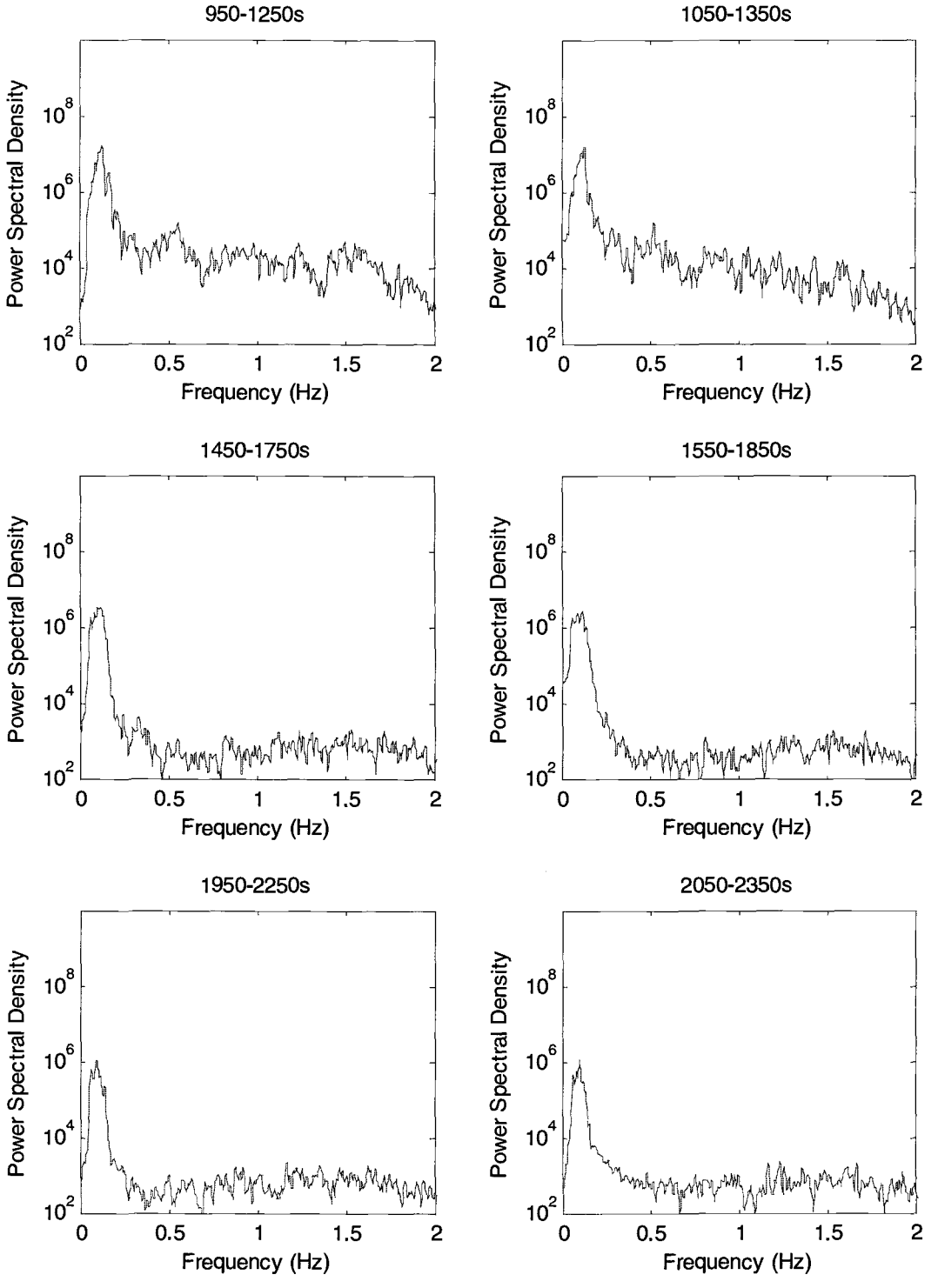

Figure 3.17 (Continued)

Table 3.3: Dominant peak frequencies of the resulting spectra for the filtered pressure data in segmented time intervals (300 seconds).

Time interval (s)	Peak frequency (Hz)
50-350	0.150
150-450	0.117
250-550	0.130
350-650	0.133
450-750	0.133
550-850	0.127
650-950	0.123
750-1050	0.123
850-1150	0.120
950-1250	0.130
1050-1350	0.133
1150-1450	0.133
1450-1750	0.120
1550-1850	0.113
1950-2250	0.093
2050-2350	0.100

To study the behavior of the oscillation with varying frequency component, we can use the variable-frequency complex demodulation method (VFCDM). This method is a modification to the complex demodulation method (CDM) and follows the evolution of the oscillatory frequency of the signal such that the output amplitude and relative phase correspond to that of the dominant oscillation regardless of the actual time

behavior of the frequency (Gasquet & Wootton, 1996). The procedure of VFCDM applied to the filtered pressure data shown in Figure 3.12 are discussed as follows.

First, we can estimate the demodulation frequency f_m from the dominant peak frequencies of the resulting spectra in the segmented time intervals. From Table 3.3, it can be seen that the dominant peak frequency varies in the range [0.093 Hz, 0.15 Hz]. The initial estimation of demodulation frequency $f_{m,0}$ need to be in this range and a low-pass cutoff frequency f_c must satisfy that the frequency band $\left[f_{m,0}-f_c, f_{m,0}+f_c\right]$ is larger than the total range of the carrier frequency over the time period of interest. Here we use $f_{m,0}=0.12Hz$ and $f_c=0.035Hz$. For the demodulation frequency of $f_{m,0}=0.12Hz$, the relative phase function $\phi_{r,0}(t)$ can be extracted by running the standard CDM routine using a 5th order Butterworth low-pass filter with a cutoff frequency of $f_c=0.035Hz$. In Figure 3.18, the upper panel shows the original relative phase plot in the range of $[-\pi,\pi]$, and the lower panel presents the unwrapped phase plot. Then, the unwrapped phase plot was smoothed by using the 5th order Butterworth low-pass filter with a cutoff frequency of 0.05 Hz: the smoothed phase plot is denoted by the thick line in the lower panel of Figure 3.18.

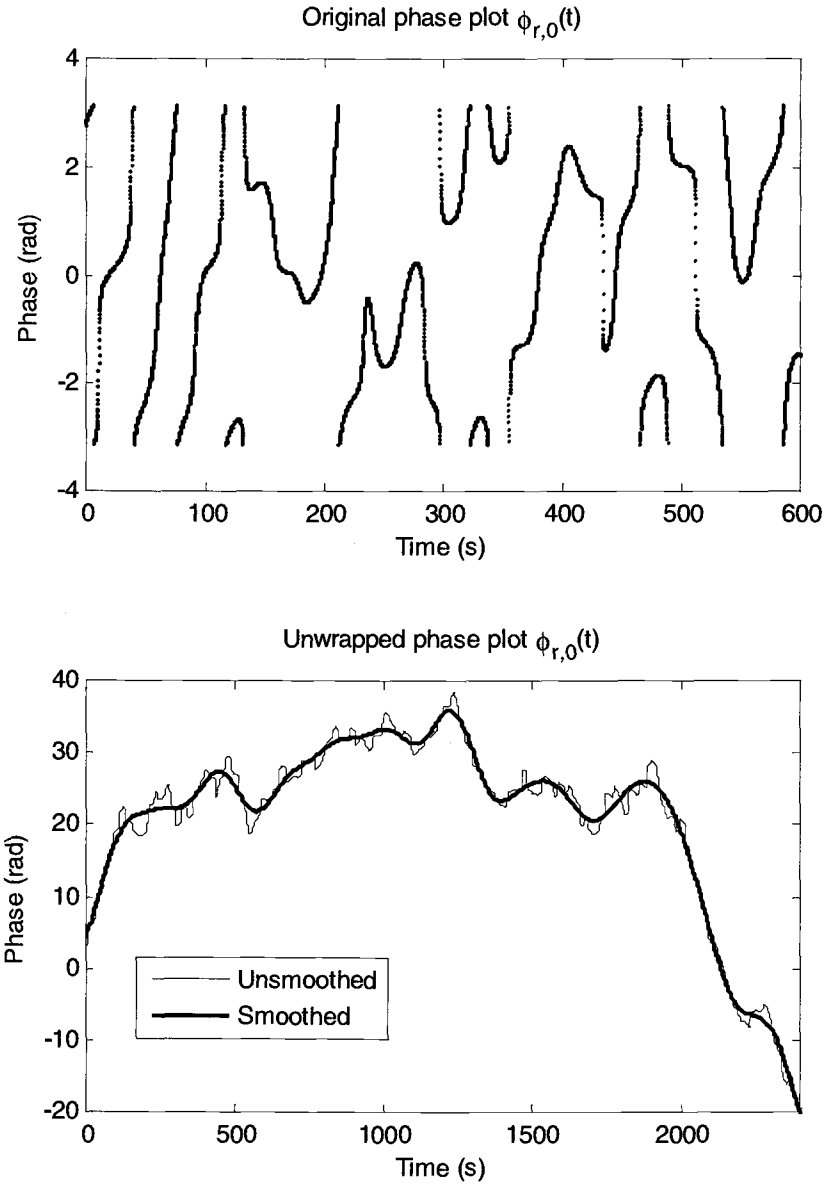

Figure 3.18: The original phase plot in the range of [0, 600s] (upper panel) and the unwrapped phase plot (lower panel). In the lower panel, the thin and thick lines denote the unsmoothed and smoothed phase plots, respectively.

The corrected demodulation frequency can be attained by

$$f_{m,1}(t) = f_{m,0} + \frac{1}{2\pi}\frac{d\phi_{r,0}(t)}{dt} \tag{3.10}$$

where the derivative of $\phi_{r,0}(t)$ can be calculated based on the smoothed phase function by using finite difference method. Note that the time derivative of $\phi_{r,0}(t)$ serves as a correction to the demodulation frequency $f_{m,0}$. Then the CDM is applied to the data again by using $f_{m,1}$ as the demodulation frequency. At this step, the low-pass filter with a narrower passband ($f_c = 0.015Hz$) was used due to the time-dependent frequency tracking. A new relative phase output can be extracted by using

$$\phi_{r,1}(t) = 2\pi \int_0^t \left[f_s(\tau) - f_{m,1}(\tau) \right] d\tau + \delta \tag{3.11}$$

This process is repeated until the correction to demodulation frequency becomes small. The iterations are made by

$$f_{m,2}(t) = f_{m,1} + \frac{1}{2\pi}\frac{d\phi_{r,1}(t)}{dt} \tag{3.12}$$

The first six iterations by the VFCDM are shown in Figure 3.19 by the unwrapped relative phase plots and the frequency corrections. The variance in the unwrapped relative phase and the correction of demodulation frequency are both getting smaller with iteration. We also find that the iteration yield the converged outputs of the 5^{th} and 6^{th} iterations, which means that the time-dependent frequency tracking is achieved after the 5^{th} correction. The time-varying demodulation frequency after the 5^{th} correction can be expressed as

$$f_{m,5}(t) = (f_{m,0} + \frac{1}{2\pi}\sum_{i=0}^{4}\frac{d\phi_{r,i}(t)}{dt}) \tag{3.13}$$

which is shown in Figure 3.20. This figure represents the temporal variations in dominant frequency of the filtered pressure fluctuations at PG1. It can be seen that the dominant frequency is around 0.15 Hz at the beginning and 0.09 Hz or so near the end of the dataset of 2400 seconds, which agrees with Table 3.3.

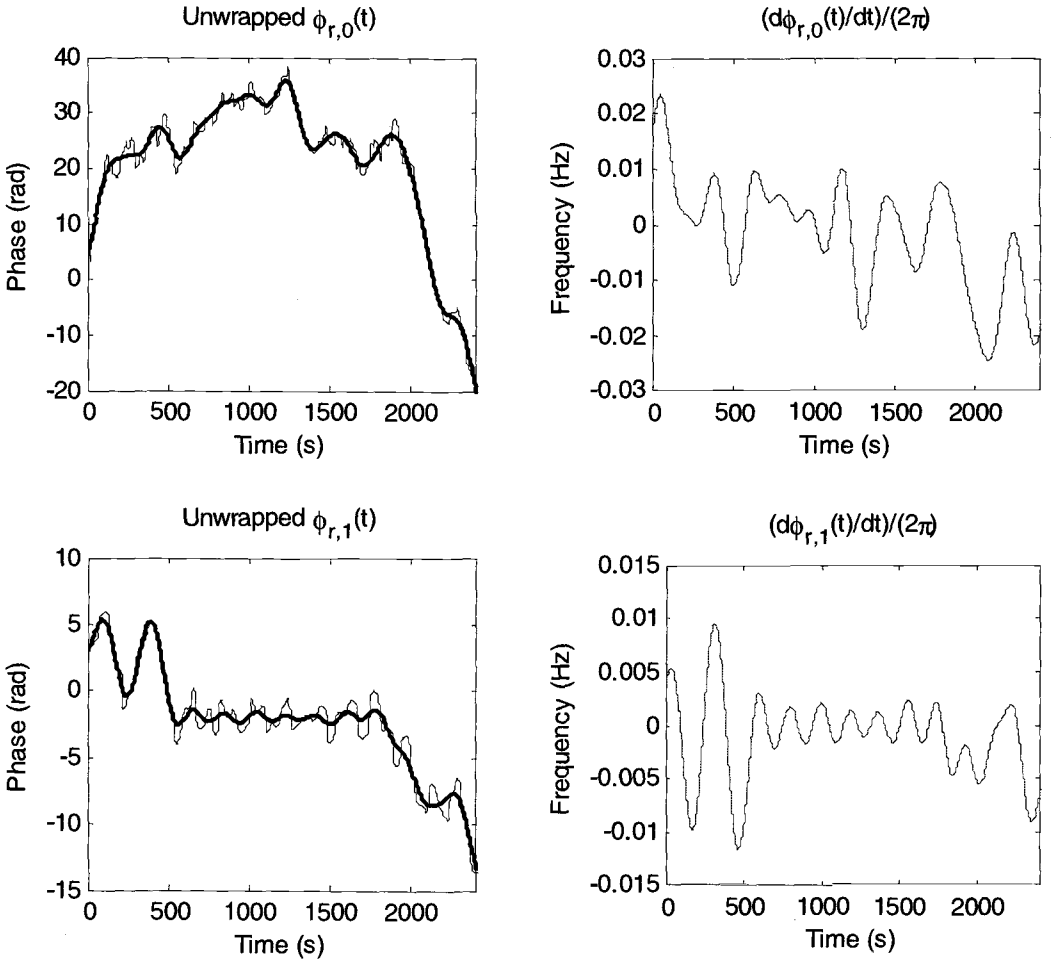

Figure 3.19: Unwrapped relative phase plots (thin line – unsmoothed & thick line - smoothed) and the frequency corrections for the first six iterations by the VFCDM.

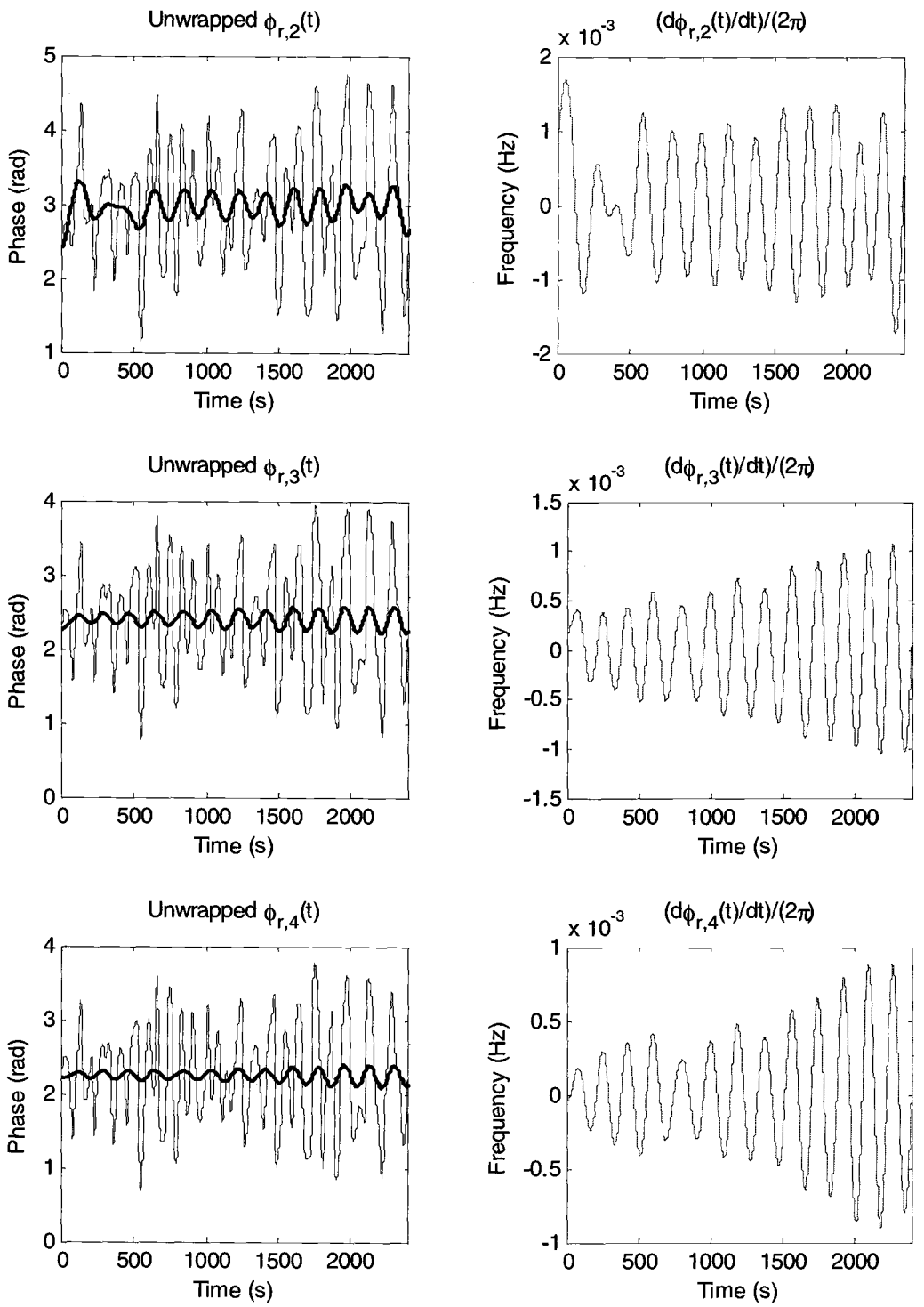

Figure 3.19 (Continued)

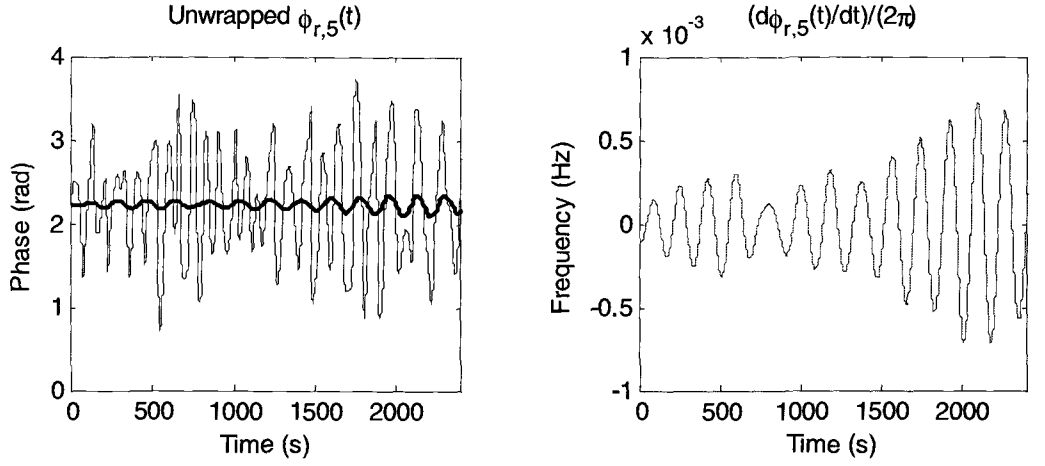

Figure 3.19 (Continued)

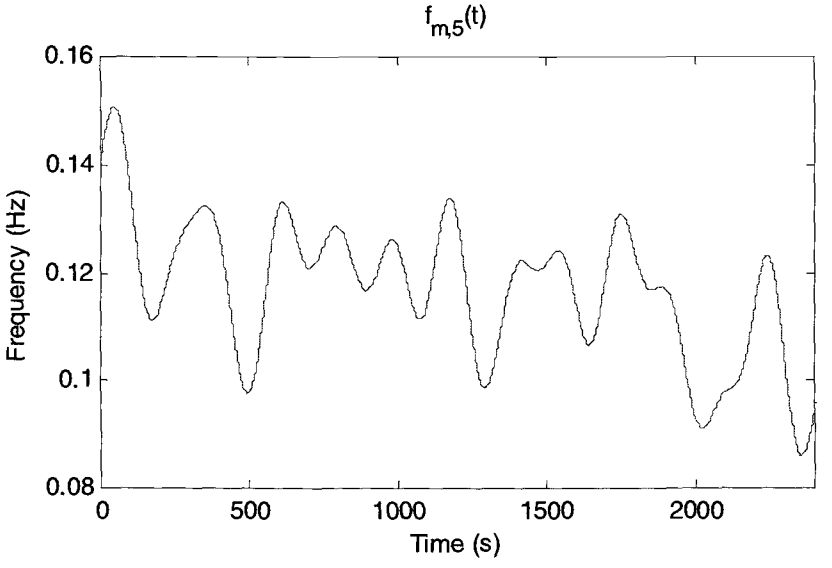

Figure 3.20: Time-varying demodulation frequency after the 5th correction.

In Figure 3.21, the bold solid line represents the output amplitude $A_5(t)$ for the dominant frequency component after 5 iterations computed using the time-varying demodulation frequency $f_{m,5}(t)$ with a 0.015 Hz low-pass cutoff frequency, and the

dotted line denotes the input pressure time series at PG1: the time series is also shown in Figure 3.12 up to 1000 seconds. The amplitude $A_5(t)$ represents a good approximation for the envelope of the pressure data.

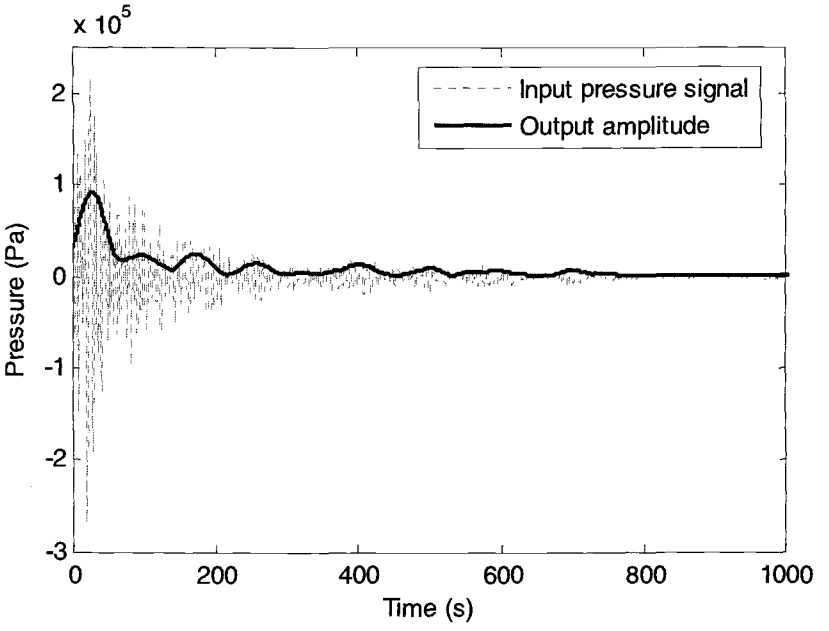

Figure 3.21: The input pressure signal at PG1 (dotted) and the output amplitude signal for the dominant frequency component by the VFCDM (bold solid).

To study the modulating signal (the slowly varying amplitude signal) in the frequency domain, the power spectral density of the de-trended modulating signal was computed. The 5th Butterworse high-pass filter with a 1/300 Hz cutoff frequency is used to de-trend the modulating signal. Figure 3.22 shows the modulating signal $A_5(t)$ (dotted line) and the de-trended modulating signal (solid line) for the duration of 100–2400 seconds. Figure 3.23 presents the periodogram of the de-trended slowly varying amplitude signal shown in Figure 3.22. The dominant peak frequency is found to be

0.0087 Hz. Figure 3.24 shows the periodograms of the de-trended amplitude signals in the segmented time intervals of 500 seconds. It can be found in this figure that the dominant peak frequency varies slightly in time: between 0.006 Hz to 0.01 Hz.

The existence of the dominant frequency component in the modulating signal $A_5(t)$ means that there are side-band frequency components around the carrier-frequency component, and the difference in frequency between the upper and the lower sidebands should be two times of the dominant peak frequency of the modulating signal $A_5(t)$. However, the periodogram in Figure 3.23 shows the peak frequency of $A_5(t)$ is not clear single value, but falls within a range of the frequency [0.006 Hz, 0.012 Hz] with the peak value at 0.0087 Hz. Figure 3.24 also demonstrates that the shape of the periodogram from 100 to 2000 seconds is basically time-invariant. Hence, we conjecture that this modulating behavior in the pressure decay data must be related to inhomogeneous sediment layers that the pressure waves penetrate (i.e. multiple layers for pressure wave to resonate besides the water column).

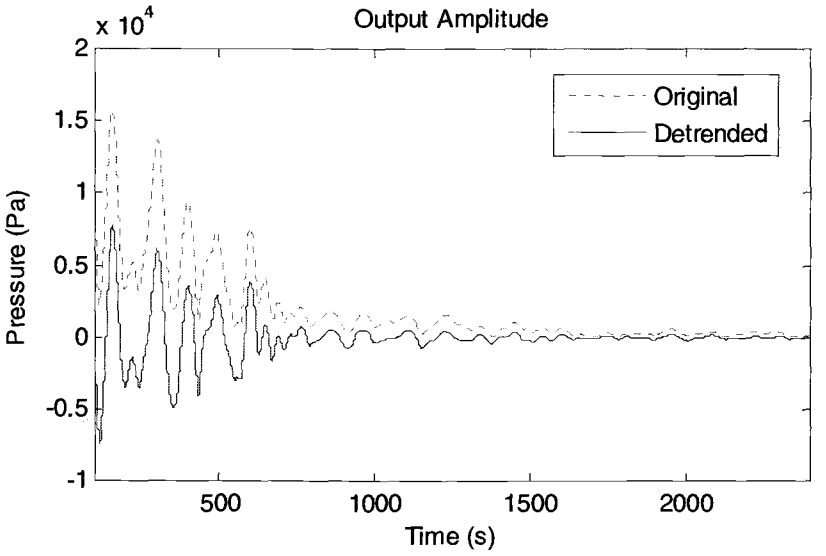

Figure 3.22: The output amplitude signal $A_5(t)$ (dotted) and the de-trended amplitude signal (solid) by using the 5th Butterworse high-pass filter with a 1/300 Hz cutoff frequency, for the duration of 100–2400 seconds.

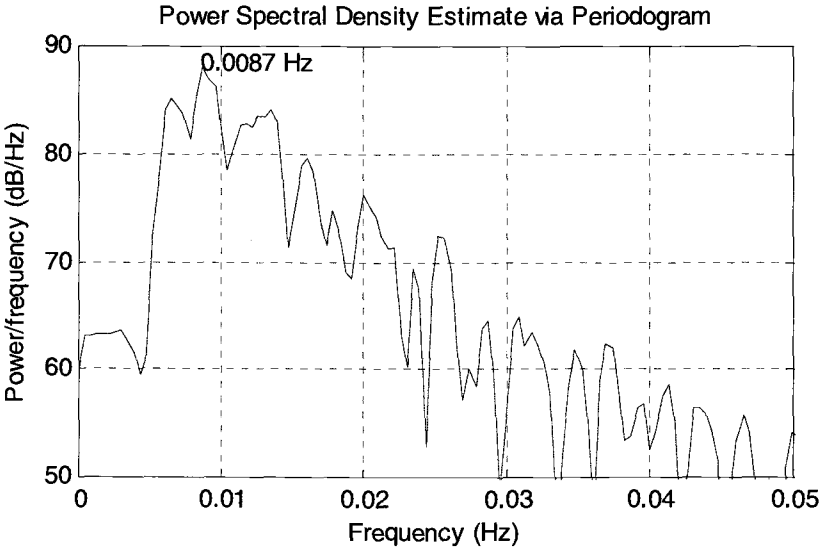

Figure 3.23: Periodogram of the de-trended slowly varying amplitude signal shown in Figure 3.22; Δf = 1/2300 Hz. The dominant peak frequency is 0.0087 Hz.

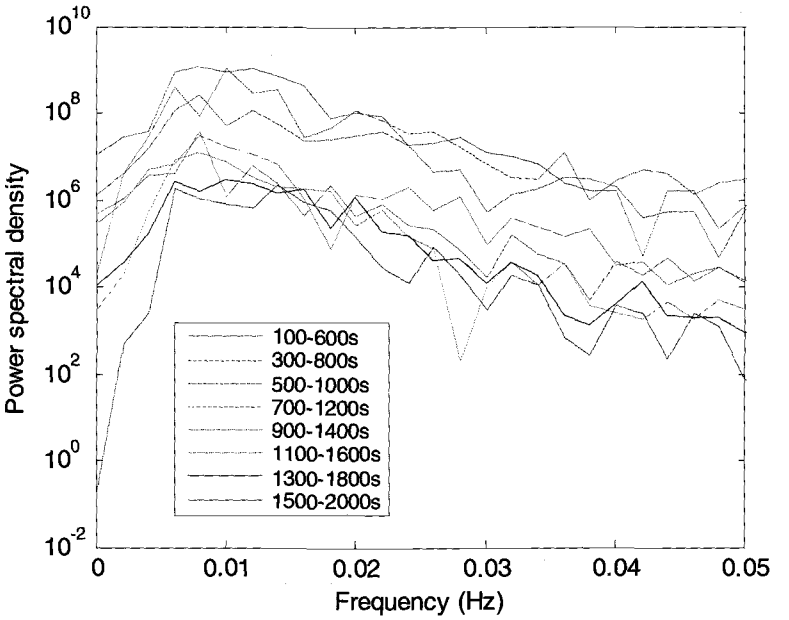

Figure 3.24: Periodograms of the de-trended amplitude signals in the segmented time intervals of 500 seconds; Δf = 1/500 Hz.

The temporal evolution of amplitude spectrum can provide the information of the amplitude in the frequency-time domain. The standard complex demodulation method (CDM) is used to extract the amplitude. The procedure is briefly described as below:

Assume the input signal be $P(t)$ $(t = 0 \sim T_0)$ and the range of frequency to be examined is $0 \sim f_0$. First, the frequency interval is divided into N small sections with the same frequency width Δf, and the frequency in each section is considered constant, which is taken at the frequency at the mid-value of each section, say f_i $(i = 1, 2, \ldots, N)$. Then consider each f_i as the demodulation frequency and apply the standard CDM to the signal $P(t)$ with a low-pass cutoff frequency $\Delta f / 2$. The output will give us the temporal variation in amplitude for the component at the frequencies near f_i. Compiling

all the outputs from the N sections in a contour plot in the frequency-time plane, the temporal evolution of amplitude spectra can be obtained.

According to Table 3.3, the dominant peak frequency of the pressure fluctuations shown in Figure 3.12 is confined within the frequency range of 0~0.2 Hz. Dividing this frequency range into 20 sections ($\Delta f = 0.01Hz$) and applying the standard CDM to the frequency at the center of each section with a 0.005 Hz low-pass cutoff frequency yield the temporal evolution of amplitude spectra for the pressure fluctuations, which is presented in Figure 3.25. Here the amplitude is normalized with the maximum value so that the maximum amplitude is constant over the time, and plotted in the logarithm scale since it varies several orders of magnitude over the frequency. Figure 3.25 clearly demonstrates the gradual decrease in the carrier frequency of the data over 2400 seconds, while the spectral characteristics of the pressure waves appear to persist: even after 2400 seconds (40 minutes), the component at the peak frequency is energetic without fading away into the background noise. Another observation that can be made from Figure 3.25 is the rapid decay in energy of the low frequency components, say, less than 0.04 Hz; the energy decays quickly in the first 500 seconds or so. The careful observation of Figure 3.25 indicates the decay process is oscillatory with the period of approximately 100 seconds. The reason is not clear. However, this observed decay behavior must be related to the gravity waves (tsunamis) generated by the earthquake.

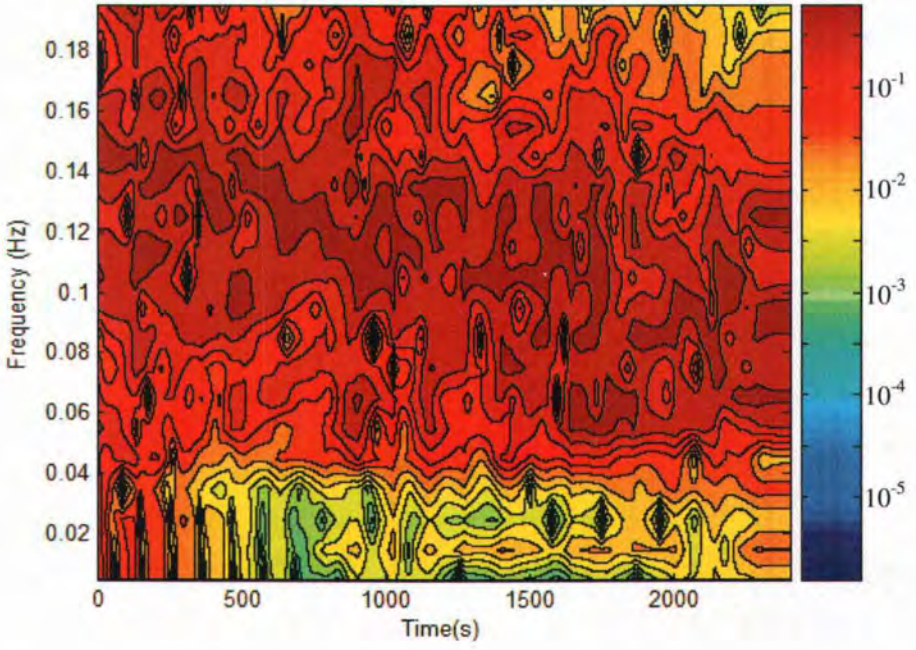

Figure 3.25: Temporal evolution of the amplitude spectra (in logarithm scale) for the pressure data shown in Figure 3.12.

4 Numerical Model

For the 2003 Tokachi-Oki earthquake, the horizontal dimension of the seafloor displacement was in the order of 100 km, which is much greater than the vertical dimension: the water depth (~ 2 km). Hence it is reasonable to assume that the majority of acoustic-wave energy would bounce back-and-forth vertically in the water column, which we may consider it analogous to the water-hammer phenomenon in the closed conduit system. Unlike the closed conduit system, there is no reflective boundary to laterally confine the acoustic wave energy; hence we anticipate the acoustic wave energy would decay slowly due to the leakage. The natural frequencies of the back-and-forth acoustic wave oscillations are not affected by the manner in which the initial motion was established, but the elastic properties of the medium in which the wave propagates. In this Chapter, a one-dimensional numerical model is constructed to simulate the pressure wave propagation.

4.1 Model Description of 1-D Pressure Wave Propagation

Suppose the distance between the solid bottom and the free water surface is H and the bottom is uplifted with the constant velocity V_0. The stages of pressure fluctuation after the bottom uplift from time t = 0 are described. The effect of reflection of pressure wave at the water surface and bottom causes a periodic fluctuation of pressure at any position of the fluid. This is illustrated in Figure 4.1. When the bottom is uplifted at the constant velocity V_0, the fluid adjacent the bottom is compressed and brought to move upward with the same velocity of the bottom. This process propagates upward, thus creating the

pressure wave (compressional wave) that travels towards the ocean surface at the acoustic speed c. The pressure wave brings the fluid to move upward with the velocity V_0 as it passes (Figure 4.1a). At time t = H/c, the entire fluid column between the water surface and the bottom is under the extra pressure Δp and with the velocity V_0 (Figure 4.1b). There is a discontinuity in pressure at the water surface at the instant of arrival of the pressure wave, since the pressure at the free surface is assumed constant under the atmospheric pressure. The situation is therefore unstable and the reflected pressure wave front (rarefaction wave) now propagates from the water surface towards the bottom at the speed of sound c in order to equalize the pressure at the water surface. The reflection of the pressure wave from the free surface is equivalent to the superimposition of the negative pressure $-\Delta p$ on the positive pressure Δp. The fluid returns the pressure to the initial value prior to the bottom uplift and the flow has a velocity $2V_0$ in the upward direction (Figure 4.1c). When the pressure wave reaches the bottom at time t = 2H/c, the pressure is everywhere at the initial hydrostatic value and the entire fluid is moving upward with a velocity $2V_0$ (Figure 4.1d). The flow conditions are now similar to those when the bottom is uplifted except that the flow has a velocity $2V_0$. The pressure thereafter drops by Δp and the fluid is brought to move upwards with the velocity V_0 (Figure 4.1e). When the negative-pressure wave front propagating with the velocity c reaches the water surface at time t = 3H/c, the fluid is uniformly at the low pressure Δp less than the initial equilibrium pressure before the bottom uplift, which gives rise to an unbalanced situation again (Figure 4.1f). The high pressure at the water surface causes the fluid to return to rest and the pressure wave front moves towards to the bottom at a

speed c (Figure 4.1g). At time t = 4H/c, the fluid is at rest everywhere and the flow conditions are exactly the same as the initial conditions (Figure 4.1h). This process is then repeated with the time period for the complete cycle, 4H/c. The periodic pressure variation at the bottom is shown in Figure 4.2.

In the above discussion, the damping effects are neglected so that the pressure vibration does not attenuate with time. But in reality, the energy does attenuate by dissipation due to the viscous effect of the fluid, leakage to the outside of the source area, and absorption to the atmosphere as well as to the sediment layers. Recall that the field pressure data attenuate with time as discussed in Chapter 3.

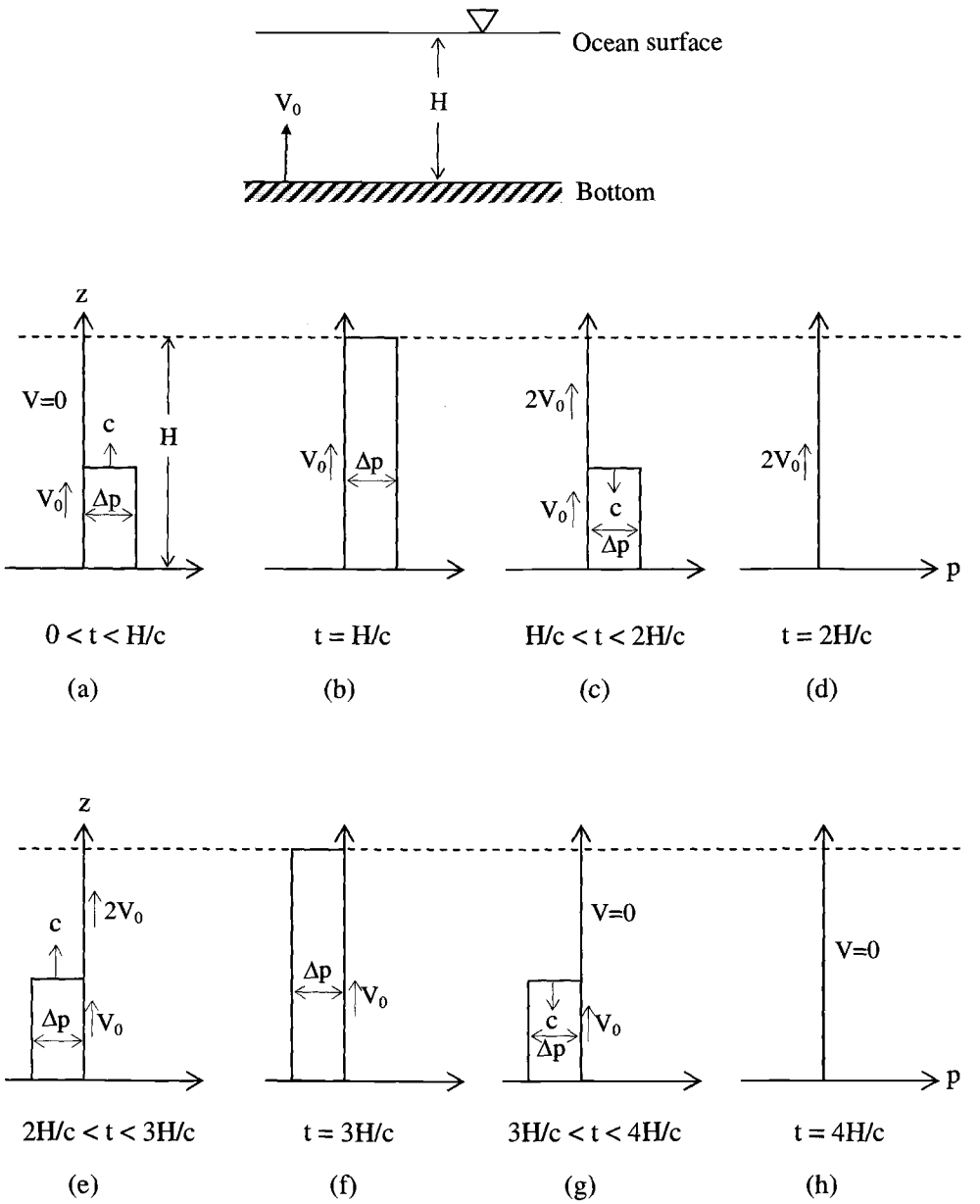

Figure 4.1: Stages of pressure fluctuation after the bottom uplift (damping effects neglected in this case). The displacement of the sea bottom is small during the process, hence the location of the bottom boundary remains at $z = 0$.

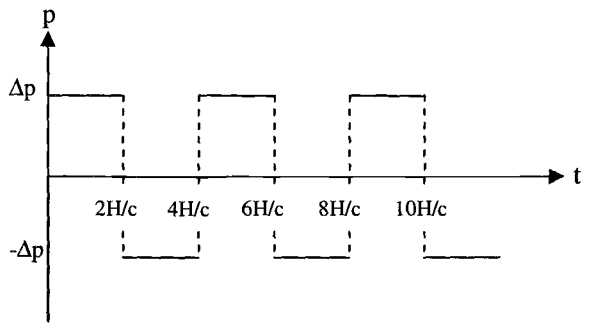

Figure 4.2: Acoustic pressure variation at the bottom.

4.2 Differential Equations for Pressure Waves

The pressure wave in elastic media is an unsteady flow. The linear momentum equation and the conservation of mass are used to express the behavior of pressure waves in the water column. In the formulation, the dependent variables are pressure p and the fluid velocity V, while the independent variables are vertical coordinate distance z ($z=0$ at the sea bottom) and time t ($t=0$ at the initiation of bottom motion). So p and V are both the functions of z and t ($p=p(z,t), V=V(z,t)$).

The 1-D linear momentum equation for inviscid fluid (i.e. Euler's equation) can be expressed by

$$\frac{\partial V}{\partial t}+V\frac{\partial V}{\partial z}=-\frac{1}{\rho}\frac{\partial p}{\partial z}-g \tag{4.1}$$

We can write the variables p and ρ in the form

$$p=p_0(z)+p'(z,t),\ \rho=\rho_0(z)+\rho'(z,t) \tag{4.2}$$

where p_0 and ρ_0 are the pressure and density at the equilibrium state, and p' and ρ' are their variations in the acoustic wave: p' is termed the 'acoustic pressure'. Then Equation (4.1) can be written as

$$\frac{\partial V}{\partial t}+V\frac{\partial V}{\partial z}=-\frac{1}{\rho_0+\rho'}\left(\frac{\partial p_0}{\partial z}+\frac{\partial p'}{\partial z}\right)-g \tag{4.3}$$

With $\frac{\partial p_0}{\partial z}=-\rho_0 g$ and $\rho' << \rho_0$, Equation (4.3) reduces to

$$\frac{\partial V}{\partial t}+V\frac{\partial V}{\partial z}+\frac{1}{\rho_0}\frac{\partial p'}{\partial z}=0 \tag{4.4}$$

As we discussed earlier, the pressure wave decays in the field data, so the momentum equation can be modified, by adding a damping term into Equation (4.4), as

$$\frac{\partial V}{\partial t}+V\frac{\partial V}{\partial z}+\frac{1}{\rho_0}\frac{\partial p'}{\partial z}+\alpha V=0 \tag{4.5}$$

where α is the damping coefficient. Note that we simply added the damping term because the attenuation can be caused by multiple factors, as we discussed earlier (dissipation, dispersion and absorption), and no rational method is available to model the attenuation. The damping term used in Equation (4.5) yields the exponential decay in velocity V, when the equation is reduced to linear.

The equation of mass conservation can be written as

$$\frac{\partial \rho}{\partial t}+\frac{\partial(\rho V)}{\partial z}=0$$

or

$$\frac{\partial \rho}{\partial t} + V\frac{\partial \rho}{\partial z} + \rho\frac{\partial V}{\partial z} = 0 \tag{4.6}$$

We assume that the propagation of acoustic wave is an adiabatic process and then introduce the adiabatic pressure-density relationship

$$c^2 = \frac{dp}{d\rho} \tag{4.7}$$

where c is the acoustic speed. So we have

$$\frac{\partial p}{\partial t} = \frac{dp}{d\rho}\frac{\partial \rho}{\partial t} = c^2\frac{\partial \rho}{\partial t} \tag{4.8}$$

$$\frac{\partial p}{\partial z} = \frac{dp}{d\rho}\frac{\partial \rho}{\partial z} = c^2\frac{\partial \rho}{\partial z} \tag{4.9}$$

According to Equations (4.8) and (4.9), replacing ρ in Equation (4.6) yields

$$\frac{\partial p}{\partial t} + V\frac{\partial p}{\partial z} + \rho c^2\frac{\partial V}{\partial z} = 0 \tag{4.10}$$

With $p = p_0 + p'$, $\frac{\partial p_0}{\partial z} = -\rho_0 g$ and $\rho' << \rho_0$, Equation (4.10) can be written as

$$\frac{\partial p'}{\partial t} + V\frac{\partial p'}{\partial z} + \rho_0 c^2\frac{\partial V}{\partial z} - \rho_0 g V = 0 \tag{4.11}$$

Equations (4.5) and (4.11) provide partial differential equations in the dependent variables V and p' in terms of the independent variables z and t.

4.3 Solution by Characteristics Method

The partial differential equations (4.5) and (4.11) may be transformed by the method of characteristics into particular ordinary differential equations. These ordinary differential

equations may then be integrated to yield finite-difference equations, which can be solved numerically.

4.3.1 Characteristic Equations

The linear momentum equation (4.5) and the equation of mass conservation (4.11) are re-written and identified as L_1 and L_2

$$L_1 = \frac{\partial V}{\partial t} + V\frac{\partial V}{\partial z} + \frac{1}{\rho_0}\frac{\partial p}{\partial z} + \alpha V = 0 \tag{4.12}$$

$$L_2 = \frac{\partial p}{\partial t} + V\frac{\partial p}{\partial z} + \rho_0 c^2 \frac{\partial V}{\partial z} - \rho_0 g V = 0 \tag{4.13}$$

Here, and henceforward, we omit the prime in p' for brevity.

By linearly combining L_1 and L_2 with an unknown multiplier λ.

$$L = L_2 + \lambda L_1 = \frac{\partial p}{\partial t} + V\frac{\partial p}{\partial z} + \rho_0 c^2 \frac{\partial V}{\partial z} - \rho_0 g V + \lambda\left(\frac{\partial V}{\partial t} + V\frac{\partial V}{\partial z} + \frac{1}{\rho_0}\frac{\partial p}{\partial z} + \alpha V\right) = 0$$

or

$$L = \left[\frac{\partial p}{\partial t} + \left(V + \frac{\lambda}{\rho_0}\right)\frac{\partial p}{\partial z}\right] + \lambda\left[\frac{\partial V}{\partial t} + \left(\frac{\rho_0 c^2 + \lambda V}{\lambda}\right)\frac{\partial V}{\partial z}\right] + (\lambda\alpha - \rho_0 g)V = 0 \tag{4.14}$$

In general, both variables p and V are functions of z and t. If the independent variable z is permitted to be a function of t, i.e. $z = z(t)$, then

$$\frac{dp}{dt} = \frac{\partial p}{\partial z}\frac{dz}{dt} + \frac{\partial p}{\partial t}, \qquad \frac{dV}{dt} = \frac{\partial V}{\partial z}\frac{dz}{dt} + \frac{\partial V}{\partial t} \tag{4.15}$$

Observation of Equation (4.14) leads us that, if

$$\frac{dz}{dt} = V + \frac{\lambda}{\rho_0} = \frac{\rho_0 c^2 + \lambda V}{\lambda} \tag{4.16}$$

then Equation (4.14) becomes the ordinary differential equation of the form

$$L = \frac{dp}{dt} + \lambda \frac{dV}{dt} + (\lambda\alpha - \rho_0 g)V = 0 \tag{4.17}$$

According to Equation (4.16), the multiplier λ takes the values

$$\lambda = \pm\rho_0 c \tag{4.18}$$

Then

$$\frac{dz}{dt} = V \pm c \tag{4.19}$$

Because the flow velocity is very small compared with the acoustic velocity ($V \ll c$) for our problem, Equation (4.19) can be written approximately as

$$\frac{dz}{dt} = \pm c \tag{4.20}$$

Substituting the values of λ into Equation (4.17) yields the following two pairs of equations which are called "the characteristic equations" and denoted by C^+ and C^-.

$$\left.\begin{aligned} L &= \frac{dp}{dt} + \rho_0 c \frac{dV}{dt} + (+\rho_0 c\alpha - \rho_0 g)V = 0 \qquad (4.21)\\ \frac{dz}{dt} &= c \qquad (4.22) \end{aligned}\right\} \quad C^+$$

$$\left.\begin{aligned} L &= \frac{dp}{dt} - \rho_0 c \frac{dV}{dt} + (-\rho_0 c\alpha - \rho_0 g)V = 0 \qquad (4.23)\\ \frac{dz}{dt} &= -c \qquad (4.24) \end{aligned}\right\} \quad C^-$$

Equations (4.22) and (4.24) are plotted as two straight lines on the $z-t$ plane, as shown in Figure 4.3. These lines in the $z-t$ plane are called the "characteristic" lines. The

slopes of lines AP and BP are $\frac{dz}{dt} = \pm c$, respectively. Each of Equations (4.21) and (4.23) is valid only on the corresponding characteristic line. Note that unlike a traditional open-channel flow problem or a hypersonic compressible flow problem, the approximation of $\frac{dz}{dt} = \pm c$ made by $V \ll c$ simplifies the computations substantially.

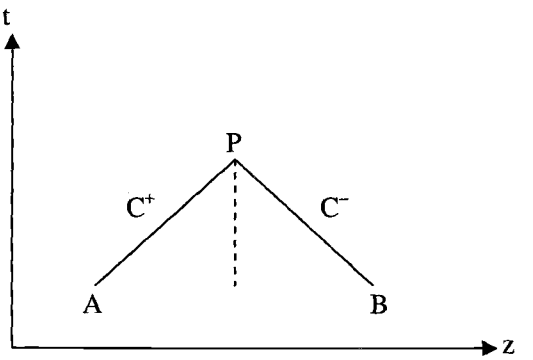

Figure 4.3: Characteristic lines in the zt plane.

4.3.2 Finite-difference Equations

We take a constant time-step Δt and divide the distance between the bottom and ocean surface H into N cells with the size of the i th cell $(\Delta z)_i = z_{i+1} - z_i = c_i(t_{n+1} - t_n) = c_i \Delta t$, as shown in Figure 4.4. The C^+ and C^- lines are then the diagonals of the rectangular grid, shown by the lines AP and BP.

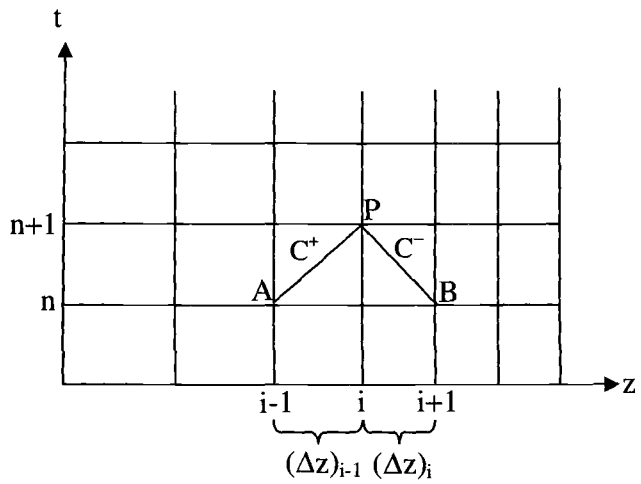

Figure 4.4: zt grid for solving characteristic equations.

Multiplying Equation (4.21) by dt, and integrating along the line AP, yields

$$\int_A^P dp + \int_A^P \rho_0 c dV + \int_A^P (\rho_0 c\alpha - \rho_0 g) V dt = 0 \tag{4.25}$$

The equation may be written, in finite-difference form, as

$$p_P - p_A + \rho_0 c(V_P - V_A) + (\rho_0 c\alpha - \rho_0 g)\frac{(V_A + V_P)}{2}\Delta t = 0 \tag{4.26}$$

The corresponding integration of Equation (4.23) along the C^- line between B and P, in the similar manner, becomes

$$p_P - p_B - \rho_0 c(V_P - V_B) - (\rho_0 c\alpha + \rho_0 g)\frac{(V_B + V_P)}{2}\Delta t = 0 \tag{4.27}$$

Equations (4.26) and (4.27) may be written in the following form, namely

$$p_i^{n+1} - p_{i-1}^n + (\rho_0 c)_{i-1}(V_i^{n+1} - V_{i-1}^n) + (\rho_0 c\alpha - \rho_0 g)_{i-1}\frac{(V_{i-1}^n + V_i^{n+1})}{2}\Delta t = 0 \tag{4.28}$$

$$p_i^{n+1} - p_{i+1}^n - (\rho_0 c)_i(V_i^{n+1} - V_{i+1}^n) - (\rho_0 c\alpha + \rho_0 g)_i\frac{(V_{i+1}^n + V_i^{n+1})}{2}\Delta t = 0 \tag{4.29}$$

Solving these two compatibility equations simultaneously for unknowns V_i^{n+1} and p_i^{n+1} at any interior grid intersection point, yields

$$V_i^{n+1} = \frac{2(p_{i+1}^n - p_{i-1}^n) - (g\Delta t + (2-\alpha\Delta t)c_{i-1})\rho_{0,i-1}V_{i-1}^n + (g\Delta t - (2-\alpha\Delta t)c_i)\rho_{0,i}V_{i+1}^n}{(g\Delta t - (2+\alpha\Delta t)c_{i-1})\rho_{0,i-1} - (g\Delta t + (2+\alpha\Delta t)c_i)\rho_{0,i}} \tag{4.30}$$

$$p_i^{n+1} = p_{i-1}^n + \rho_{0,i-1}c_{i-1}(V_{i-1}^n - V_i^{n+1}) + \rho_{0,i-1}(g - c_{i-1}\alpha)\Delta t\frac{(V_{i-1}^n + V_i^{n+1})}{2} \tag{4.31}$$

The acoustic pressure p and flow velocity V at any grid intersection point are always available for the preceding time step, either as given initial conditions or as the results of a previous stage of the calculations.

Since the end points of the system start to affect the interior points after the first time step, it is necessary to introduce the appropriate boundary conditions in order to complete the solution for any position and any time.

4.3.3 Initial and Boundary Conditions

Initial Conditions

At time $t = 0$, the fluid is at rest except the layer adjacent to the bottom being at the same velocity as that of the bottom, and no pressure wave is generated.

$$V_1^0 = V_{BT}(t=0),\ V_i^0 = 0,\ i = 2,3,...,N+1 \tag{4.32}$$

$$p_i^0 = 0,\ i = 1,2,\ldots,N+1 \tag{4.33}$$

where V_{BT} is the moving velocity of the bottom.

Boundary conditions

The fluid adjacent to the bottom has the same velocity as that of the bottom.

$$V_1^n = V_{BT}(t = t_n),\ n \geq 0 \tag{4.34}$$

And the acoustic pressure p at the bottom for each time step is determined by a direct solution of Equation (4.29).

$$p_1^{n+1} = p_2^n + \rho_{0,1} c_1 \left(V_1^{n+1} - V_2^n\right) + \rho_{0,1}(g + c_1 \alpha)\frac{(V_2^n + V_1^{n+1})}{2}\Delta t \tag{4.35}$$

At the free surface, the fluid is always under the atmospheric pressure, so the acoustic pressure is zero.

$$P_{N+1}^n = 0,\ n \geq 0 \tag{4.36}$$

And the fluid velocity V at the free surface for each time step can be obtained by Equation (4.28).

$$V_{N+1}^{n+1} = \frac{2(p_{N+1}^{n+1} - p_N^n) - (g\Delta t + (2 - \alpha\Delta t)c_N)\rho_{0,N} V_N}{(g\Delta t - (2 + \alpha\Delta t)c_N)\rho_{0,N}} \tag{4.37}$$

5 Analytical Model

5.1 Model 1: Water Column

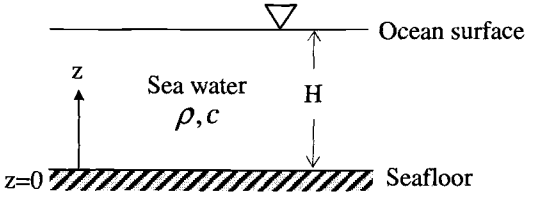

Figure 5.1: One-layer model (water column) for simulating pressure waves.

The pressure wave is said to be longitudinal because the motion is in the same direction as the wave propagates. Let $\eta(z,t)$ denote the longitudinal particle displacement at the position z. The one-dimensional wave equation in terms of the longitudinal displacement is expressed as

$$\frac{\partial^2 \eta}{\partial z^2} = \frac{1}{c^2}\frac{\partial^2 \eta}{\partial t^2} \tag{5.1}$$

The general harmonic solution to the wave equation for plane progressive waves is

$$\eta(z,t) = A\cos[\omega(t - z/c) + \delta_A] + B\cos[\omega(t + z/c) + \delta_B] \tag{5.2}$$

where c is the velocity of pressure wave, ω is the angular frequency, A, B are the arbitrary constants, and δ_A, δ_B are the phase angles. The first term of the solution represents waves traveling in the forward (positive) z direction, and the second term, waves traveling in the backward (negative) z direction.

In the case of pure standing waves, the amplitudes A and B should be the same, then Equation (5.2) becomes

$$\eta(z,t) = 2A\cos[\omega(z/c)+\varphi]\cos[\omega t+\psi] \tag{5.3}$$

where $\varphi = \frac{\delta_B - \delta_A}{2}$, $\psi = \frac{\delta_B + \delta_A}{2}$.

Applying the no-flux boundary condition at the bottom ($z = 0$) yields

$$\eta(0,t) = 2A\cos(\varphi)\cos(\omega t+\psi) = 0 \tag{5.4}$$

and the zero acoustic pressure condition at the free surface ($z = H$) yields

$$p(H,t) = -\rho c^2 \frac{\partial \eta(z,t)}{\partial z} = -2\rho c\omega A\sin[\omega(H/c)+\varphi]\cos[\omega t+\psi] = 0 \tag{5.5}$$

where ρ is the density of medium. This expression of acoustic pressure in terms of the longitudinal displacement can be obtained by using the linearized Equation (4.10):

$$\frac{\partial p}{\partial t} = -\rho c^2 \frac{\partial V}{\partial z} \tag{5.6}$$

where V is fluid particle velocity, and $c^2 = \frac{dp}{d\rho}$ (assume a functional dependence $p = p(\rho)$). Integrating Equation (5.6) yields

$$p = -\rho c^2 \frac{\partial}{\partial z}\int V dt = -\rho c^2 \frac{\partial \eta}{\partial z} \tag{5.7}$$

To satisfy the boundary conditions: Equations (5.4) and (5.5), we require

$$\cos(\varphi) = 0 \text{ or } \varphi = (2m+1)\pi/2 \text{ for } m = 0,1,2,... \tag{5.8}$$

And

$$\sin[\omega(H/c)+\varphi] = 0 \text{ or } \omega(H/c)+\varphi = n\pi \text{ for } n = 0,1,2,... \tag{5.9}$$

The allowed angular frequencies are thus given by

$$\omega = [(2n-2m-1)\pi]c/2H = [(2k+1)\pi]c/2H \text{ for } k = 0,1,2,... \tag{5.10}$$

So the corresponding frequencies are

$$f_k = \omega/2\pi = (2k+1)c/4H \text{ for } k = 0,1,2,... \tag{5.11}$$

These special frequencies are termed 'natural' or 'characteristic' frequencies.

5.2 Model 2: Water Column and Single Sediment Layer

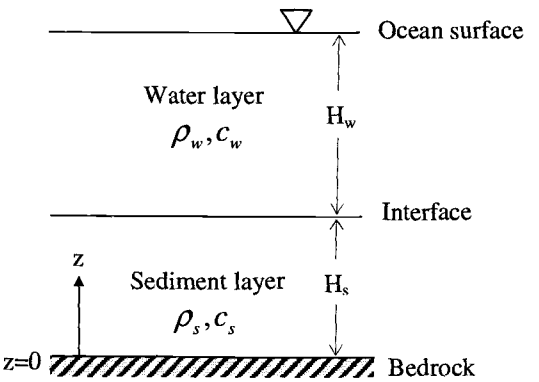

Figure 5.2: Two-layer model (water column and single sediment layer) for simulating pressure waves.

The longitudinal displacements in sediment layer and water layer obey the wave equations, respectively

$$\frac{\partial^2 \eta_s}{\partial z^2} = \frac{1}{c_s^2}\frac{\partial^2 \eta_s}{\partial t^2} \tag{5.12}$$

and

$$\frac{\partial^2 \eta_w}{\partial z^2} = \frac{1}{c_w^2}\frac{\partial^2 \eta_w}{\partial t^2} \tag{5.13}$$

The standing-wave solutions to Equations (5.12) and (5.13) are

$$\eta_s(z,t) = 2A_s \cos[\omega(z/c_s)+\varphi_s]\cos[\omega t+\psi_s] \text{ for } 0 \le z \le H_s \tag{5.14}$$

and

$$\eta_w(z,t) = 2A_w \cos[\omega(z/c_w)+\varphi_w]\cos[\omega t+\psi_w] \text{ for } H_s \le z \le H_s + H_w \tag{5.15}$$

Applying the no-flux boundary condition at the bottom ($z = 0$) and zero acoustic pressure at the free surface ($z = H_s + H_w$) yields

$$\eta_s(0,t) = 2A_s \cos(\varphi_s)\cos(\omega t + \psi_s) = 0 \tag{5.16}$$

and

$$\begin{aligned} p_w(H_s + H_w, t) &= -\rho_w c_w{}^2 \left.\frac{\partial \eta_w(z,t)}{\partial z}\right|_{z=H_s+H_w} \\ &= -2\rho_w c_w \omega A_w \sin[\omega(H_s + H_w)/c_w + \varphi_w]\cos[\omega t + \psi_w] = 0 \end{aligned} \tag{5.17}$$

At the water–sediment interface, continuity of displacement yields

$$\eta_s(H_s, t) = \eta_w(H_s, t)$$

or

$$\begin{aligned} &A_s \cos[\omega(H_s/c_s) + \varphi_s]\cos[\omega t + \psi_s] \\ &= A_w \cos[\omega(H_s/c_w) + \varphi_w]\cos[\omega t + \psi_w] \end{aligned} \tag{5.18}$$

and continuity of pressure yields

$$p_s(H_s, t) = p_w(H_s, t)$$

or

$$\rho_s c_s^2 \left.\frac{\partial \eta_s(z,t)}{\partial z}\right|_{z=H_s} = \rho_w c_w^2 \left.\frac{\partial \eta_w(z,t)}{\partial z}\right|_{z=H_s}$$

or

$$\begin{aligned} &\rho_s c_s A_s \sin[\omega H_s/c_s + \varphi_s]\cos[\omega t + \psi_s] \\ &= \rho_w c_w A_w \sin[\omega H_s/c_w + \varphi_w]\cos[\omega t + \psi_w] \end{aligned} \tag{5.19}$$

According to Equations (5.16) and (5.17), we can get

$$\cos(\varphi_s) = 0 \text{ or } \varphi_s = (2m+1)\pi/2 \text{ for } m = 0,1,2,... \tag{5.20}$$

And

$$\sin[\omega(H_s + H_w)/c_w + \varphi_w] = 0$$

Or

$$\omega(H_s + H_w)/c_w + \varphi_w = n\pi \text{ for } n = 0,1,2,... \tag{5.21}$$

Dividing Equation (5.19) by Equation (5.18) gets

$$\rho_s c_s \tan[\omega H_s / c_s + \varphi_s] = \rho_w c_w \tan[\omega H_s / c_w + \varphi_w] \tag{5.22}$$

Substituting Equations (5.20) and (5.21) into Equation (5.22) yields

$$\rho_s c_s \tan[\omega H_s / c_s + (2m+1)\pi/2] = \rho_w c_w \tan[n\pi - \omega H_w / c_w] \tag{5.23}$$

and hence

$$\tan\left(\frac{\omega H_s}{c_s}\right)\tan\left(\frac{\omega H_w}{c_w}\right) = \frac{\rho_s c_s}{\rho_w c_w} \tag{5.24}$$

Thus the natural frequencies are given by

$$\tan\left(\frac{2\pi f H_s}{c_s}\right)\tan\left(\frac{2\pi f H_w}{c_w}\right) = \frac{\rho_s c_s}{\rho_w c_w} \tag{5.25}$$

5.3 Model 3: Water Column and Two Sediment Layers

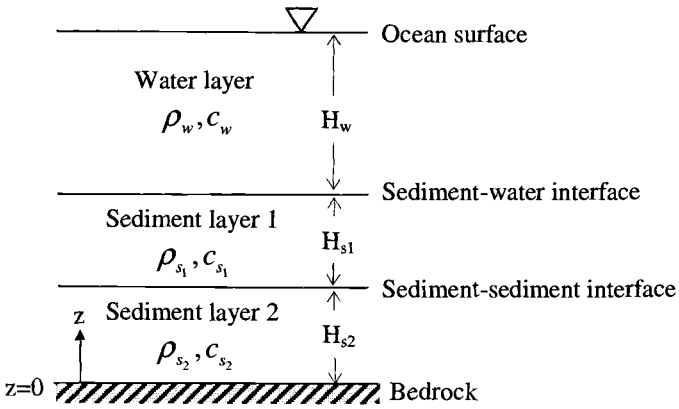

Figure 5.3: Three-layer model (water column and two sediment layers) for simulating pressure waves.

Similar to the two-layer case, the standing-wave solutions for the longitudinal displacement in sediment layer 2, 1 and water layer are

$$\eta_{s_2}(z,t) = 2A_{s_2}\cos[\omega(z/c_{s_2})+\varphi_{s_2}]\cos[\omega t+\psi_{s_2}] \text{ for } 0 \le z \le H_{s_2} \tag{5.26}$$

$$\eta_{s_1}(z,t) = 2A_{s_1}\cos[\omega(z/c_{s_1})+\varphi_{s_1}]\cos[\omega t+\psi_{s_1}] \text{ for } H_{s_2} \le z \le H_{s_1}+H_{s_2} \tag{5.27}$$

$$\eta_w(z,t) = 2A_w\cos[\omega(z/c_w)+\varphi_w]\cos[\omega t+\psi_w] \quad \text{for } H_{s_1}+H_{s_2} \le z \le H_w+H_{s_1}+H_{s_2} \tag{5.28}$$

Applying the no-flux boundary condition at the bottom ($z=0$) and zero acoustic pressure at the free surface ($z = H_w + H_{s_1} + H_{s_2}$) yields

$$\eta_{s_2}(0,t) = 2A_{s_2}\cos(\varphi_{s_2})\cos(\omega t+\psi_{s_2}) = 0 \tag{5.29}$$

and

$$\begin{aligned} p_w(H_w+H_{s_1}+H_{s_2},t) &= -\rho_w c_w{}^2 \left.\frac{\partial \eta_w(z,t)}{\partial z}\right|_{z=H_w+H_{s_1}+H_{s_2}} \\ &= -2\rho_w c_w \omega A_w \sin[\omega(H_w+H_{s_1}+H_{s_2})/c_w+\varphi_w]\cos[\omega t+\psi_w] = 0 \end{aligned} \tag{5.30}$$

At the water–sediment 1 interface, continuity of displacement yields

$$\eta_{s_1}(H_{s_1}+H_{s_2},t) = \eta_w(H_{s_1}+H_{s_2},t)$$

or

$$\begin{aligned} &A_{s_1}\cos[\omega(H_{s_1}+H_{s_2})/c_{s_1})+\varphi_{s_1}]\cos[\omega t+\psi_{s_1}] \\ &= A_w\cos[\omega(H_{s_1}+H_{s_2})/c_w)+\varphi_w]\cos[\omega t+\psi_w] \end{aligned} \tag{5.31}$$

and continuity of pressure yields

$$p_{s_1}(H_{s_1}+H_{s_2},t) = p_w(H_{s_1}+H_{s_2},t)$$

or

$$\rho_{s_1} c_{s_1}{}^2 \left.\frac{\partial \eta_{s_1}(z,t)}{\partial z}\right|_{z=H_{s_1}+H_{s_2}} = \rho_w c_w{}^2 \left.\frac{\partial \eta_w(z,t)}{\partial z}\right|_{z=H_{s_1}+H_{s_2}}$$

or

$$\begin{aligned} &\rho_{s_1} c_{s_1} A_{s_1} \sin[\omega(H_{s_1}+H_{s_2})/c_{s_1}+\varphi_{s_1}]\cos[\omega t+\psi_{s_1}] \\ &= \rho_w c_w A_w \sin[\omega(H_{s_1}+H_{s_2})/c_w+\varphi_w]\cos[\omega t+\psi_w] \end{aligned} \tag{5.32}$$

At the sediment 1–sediment 2 interface, two boundary conditions

$$\eta_{s_1}(H_{s_2},t)=\eta_{s_2}(H_{s_2},t)$$

or

$$\begin{aligned} &A_{s_1}\cos[\omega H_{s_2}/c_{s_1}+\varphi_{s_1}]\cos[\omega t+\psi_{s_1}] \\ &=A_{s_2}\cos[\omega H_{s_2}/c_{s_2})+\varphi_{s_2}]\cos[\omega t+\psi_{s_2}] \end{aligned} \tag{5.33}$$

and

$$p_{s_1}(H_{s_2},t)=p_{s_2}(H_{s_2},t)$$

or

$$\rho_{s_1}c_{s_1}{}^2\left.\frac{\partial\eta_{s_1}(z,t)}{\partial z}\right|_{z=H_{s_2}}=\rho_{s_2}c_{s_2}{}^2\left.\frac{\partial\eta_{s_2}(z,t)}{\partial z}\right|_{z=H_{s_2}}$$

or

$$\begin{aligned} &\rho_{s_1}c_{s_1}A_{s_1}\sin[\omega H_{s_2}/c_{s_1}+\varphi_{s_1}]\cos[\omega t+\psi_{s_1}] \\ &=\rho_{s_2}c_{s_2}A_{s_2}\sin[\omega H_{s_2}/c_{s_2}+\varphi_{s_2}]\cos[\omega t+\psi_{s_2}] \end{aligned} \tag{5.34}$$

By Equation (5.28) and (5.29), we can get

$$\cos(\varphi_{s_2})=0 \text{ or } \varphi_{s_2}=(2m+1)\pi/2 \text{ for } m=0,1,2,... \tag{5.35}$$

and

$$\sin[\omega(H_w+H_{s_1}+H_{s_2})/c_w+\varphi_w]=0$$

or

$$\omega(H_w+H_{s_1}+H_{s_2})/c_w+\varphi_w=n\pi \text{ for } n=0,1,2,... \tag{5.36}$$

Dividing Equation (5.31) by (5.30) and Equation (5.33) by (5.32) gets

$$\rho_{s_1}c_{s_1}\tan[\omega(H_{s_1}+H_{s_2})/c_{s_1}+\varphi_{s_1}]=\rho_w c_w\tan[\omega(H_{s_1}+H_{s_2})/c_w+\varphi_w] \tag{5.37}$$

and

$$\rho_{s_1} c_{s_1} \tan[\omega H_{s_2} / c_{s_1} + \varphi_{s_1}] = \rho_{s_2} c_{s_2} \tan[\omega H_{s_2} / c_{s_2} + \varphi_{s_2}] \tag{5.38}$$

Substituting Equations (5.35) and (5.34) into Equations (5.36) and (5.37), respectively, we have

$$\begin{aligned} \rho_{s_1} c_{s_1} \tan[\omega(H_{s_1} + H_{s_2}) / c_{s_1} + \varphi_{s_1}] &= \rho_w c_w \tan[n\pi - \omega H_w / c_w] \\ &= -\rho_w c_w \tan[\omega H_w / c_w] \end{aligned} \tag{5.39}$$

And

$$\begin{aligned} \rho_{s_1} c_{s_1} \tan[\omega H_{s_2} / c_{s_1} + \varphi_{s_1}] &= \rho_{s_2} c_{s_2} \tan[\omega H_{s_2} / c_{s_2} + (2m+1)\pi/2] \\ &= -\rho_{s_2} c_{s_2} \cot[\omega H_{s_2} / c_{s_2}] \end{aligned} \tag{5.40}$$

The term $\tan[\omega(H_{s_1} + H_{s_2}) / c_{s_1} + \varphi_{s_1}]$ can be expressed in terms of $\tan[\omega H_{s_1} / c_{s_1}]$ and $\tan[\omega H_{s_2} / c_{s_1} + \varphi_{s_1}]$, then Equation (5.39) can be written as

$$\rho_{s_1} c_{s_1} \frac{\tan[\omega H_{s_1} / c_{s_1}] + \tan[\omega H_{s_2} / c_{s_1} + \varphi_{s_1}]}{1 - \tan[\omega H_{s_1} / c_{s_1}] \tan[\omega H_{s_2} / c_{s_1} + \varphi_{s_1}]} = -\rho_w c_w \tan[\omega H_w / c_w] \tag{5.41}$$

Substituting Equation (5.40) into Equation (5.41) yields

$$\frac{\dfrac{\rho_{s_2} c_{s_2}}{\rho_{s_1} c_{s_1}} - \tan\left(\dfrac{\omega H_{s_1}}{c_{s_1}}\right) \tan\left(\dfrac{\omega H_{s_2}}{c_{s_2}}\right)}{\tan\left(\dfrac{\omega H_{s_2}}{c_{s_2}}\right) + \dfrac{\rho_{s_2} c_{s_2}}{\rho_{s_1} c_{s_1}} \tan\left(\dfrac{\omega H_{s_1}}{c_{s_1}}\right)} = \frac{\rho_w c_w}{\rho_{s_1} c_{s_1}} \tan\left(\frac{\omega H_w}{c_w}\right) \tag{5.42}$$

Thus the natural frequencies satisfy

$$\frac{\dfrac{\rho_{s_2} c_{s_2}}{\rho_{s_1} c_{s_1}} - \tan\left(\dfrac{2\pi f H_{s_1}}{c_{s_1}}\right) \tan\left(\dfrac{2\pi f H_{s_2}}{c_{s_2}}\right)}{\tan\left(\dfrac{2\pi f H_{s_2}}{c_{s_2}}\right) + \dfrac{\rho_{s_2} c_{s_2}}{\rho_{s_1} c_{s_1}} \tan\left(\dfrac{2\pi f H_{s_1}}{c_{s_1}}\right)} = \frac{\rho_w c_w}{\rho_{s_1} c_{s_1}} \tan\left(\frac{2\pi f H_w}{c_w}\right) \tag{5.43}$$

6 Results and Discussions

6.1 Time History of Seafloor Displacement Used in Model

To simulate the pressure waves generated by the seafloor displacement, the time history of the displacement must be given as an initial condition. Here a half cosine curve is used to roughly simulate the time history of seafloor displacement, which is expressed as

$$d = \frac{\Delta D}{2}\left[1-\cos\left(\frac{\pi}{\tau}t\right)\right] \text{ for } 0 \le t \le \tau \tag{6.1}$$

where τ is the duration of the seafloor displacement and ΔD is the net seafloor uplift. The moving velocity of the seafloor can be obtained by taking derivative of the displacement with respect to time:

$$V(t) = \Delta D\frac{\pi}{2\tau}\sin\left(\frac{\pi}{\tau}t\right) \text{ for } 0 \le t \le \tau \tag{6.2}$$

The sketches of the seafloor displacement and moving velocity are shown in Figure 6.1.

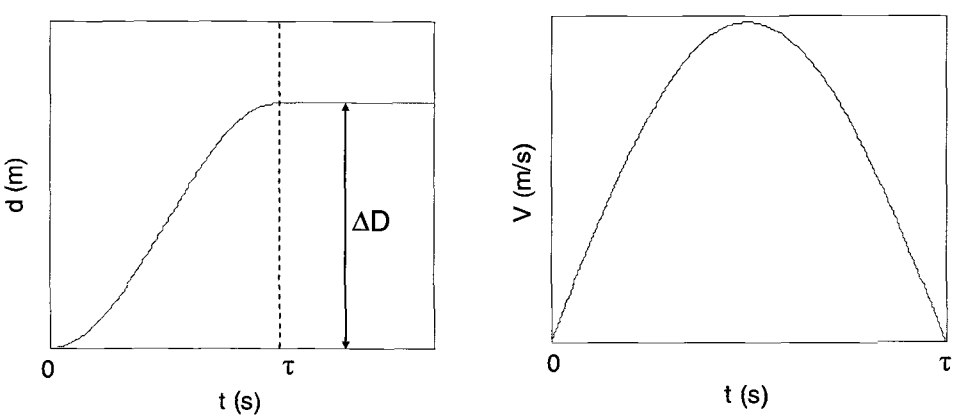

Figure 6.1: Sketches of the displacement (d) and moving velocity (V) of the seafloor used in simulation.

The estimation of co-seismic uplift of the seafloor was refined by Hirata (2004) based on the pressure measurements before and after the earthquake: the net uplift is 33cm at PG1 ($\Delta D1 = 0.33m$). According to the Harvard CMT Catalog, the 2003 Tokachi-Oki earthquake lasted 33.5 seconds. However, during the earthquake the rupture propagated towards Hokkaido (Yagi, 2004) and the bottom displacement took place as a traveling wave. Therefore, the duration of the bottom displacement at a given location in the tsunami source area must be shorter than the earthquake duration. Nosov (2005) estimated the duration of seafloor displacement at PG1 as $\tau_{PG1} \approx 4s$ with the constant co-seismic bottom displacement velocity $U \sim 0.1m/s$.

The pressure (acoustic) waves, generated by the rapid seafloor uplift, bounce back-and-forth vertically in the water column. The combination of forward and reflected backward pressure waves results a standing wave. The natural frequencies of the standing wave depend on the elastic properties of the medium alone but not affected by the manner in which the motion of the seafloor was established. Hence the duration of the bottom displacement τ has no effect on the natural frequencies of the pressure wave. However, the uplift speed can determine the magnitude of the pressure wave.

Another parameter to be determined for the numerical simulation is the damping coefficient α. The damping term used in Equation (4.5) does not affect the natural frequencies of the pressure wave. Thus we can study the discrete frequency spectrum of the simulated pressure wave with any reasonable values of τ and α.

6.2 Estimation of Elastic Properties at PG1

The natural frequencies of the pressure wave are determined by the elastic properties of the medium in which the wave propagates. The elastic properties of a medium include the density and the acoustic speed. The following is the estimations of the acoustic speed structure and density distribution at the location of PG1.

6.2.1 Acoustic Speed Structure

Table 6.1 (a) gives the 1-D acoustic speed structure for the nearest point of PG1 & OBS1 along the survey line HK103 and Table 6.1 (b) gives the 1-D acoustic speed structure for the nearest point of PG2 & OBS3 along the survey line HK201. The data were provided by Tsuru (2004) by analyzing multi-channel seismic data on two nearby survey lines HK103 and HK201 shown in Figure 6.2.

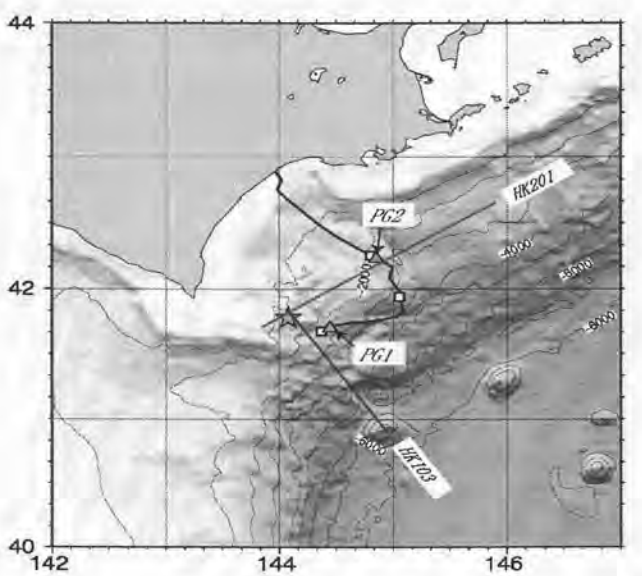

Figure 6.2: The 2003 Tokachi-Oki earthquake epicenter (pentagram), pressure gauges PG1 and PG2 at the ocean bottom, and two nearby survey lines HK103 and HK201 (Tsuru, 2004).

Table 6.1 (a): 1-D acoustic speed structure for the nearest point of PG1 & OBS1 along the survey line HK103 (Tsuru, 2004).

Depth (m) BSL	Acoustic speed (m/s)	Medium thickness (m)
0 – 2700	1500	2700
2700 – 2980	2000	280
2980 – 3460	2270	480
3460 – 4790	2650	1330
4790 – 5350	3650	560

Table 6.1 (b): 1-D acoustic speed structure for the nearest point of PG2 & OBS3 along the survey line HK201 (Tsuru, 2004).

Depth (m) BSL	Acoustic speed (m/s)	Medium thickness (m)
0 – 2290	1500	2290
2290 – 2710	1700	420
2710 – 3160	2050	450
3160 – 4300	2360	1240

According to Tsuru's interpretation, the depth of the acoustic basement below sediment layers is 5350 m (2650 m below sea floor: bsf) and 4300 m (2010 m bsf) for the nearest points of PG1 & OBS1 and PG2 & OBS3, respectively. We can assume that these sub-seafloor structures are identical to those at the locations of PG1 & OBS1 and PG2 & OBS3, respectively. PG1 and PG2 located at the sea floor at depth 2283 m and 2248 m respectively; hence we assume that the depth of the acoustic basement below the

sea level is 2283 + 2650 = 4933m (2650 m bsf) and 2248 + 2010 = 4258 m (2010 m bsf) at PG1 and PG2, respectively. With this consideration, the acoustic speed structures at PG1 and PG2 are estimated in Table 6.2.

Table 6.2: Estimated 1-D acoustic speed structures for PG1 and PG2

PG1	
Depth (thickness) (m)	Acoustic speed (m/s)
0 – 2283 (2283)	1500
2283 – 2563 (280)	2000
2563 – 3043 (480)	2270
3043 – 4373 (1330)	2650
4373 – 4933 (560)	3650

PG2	
Depth (thickness) (m)	Acoustic speed (m/s)
0 – 2248	1500
2248 – 2668 (420)	1700
2668 – 3218 (450)	2050
3218 – 4458 (1240)	2360

For PG1, the acoustic speed in the lowest sediment layer (4373 ~ 4933 m) is 3650 m/s, which is excessively larger than those in the other sediment layers. Therefore, it is reasonable to assume that the lowest layer is not soft sediment and can be neglected from our analyses. In other words, we can assume 4373 m as the depth of the acoustic basement below the sea level (2090 m below the sea floor). Figure 6.3 shows the estimated structure of water and sediment layers below the ocean surface and the corresponding acoustic speeds (PG1 is located at the seafloor).

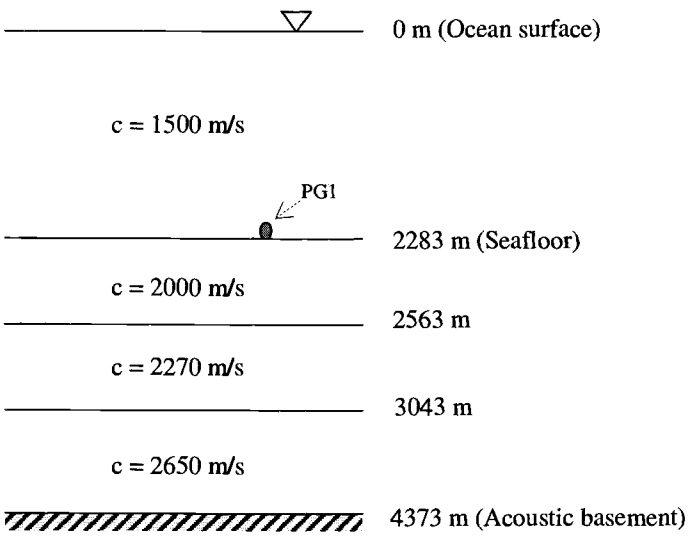

Figure 6.3 (a): Sketch of the acoustic speed structure below the sea level (PG1 is located at the seafloor).

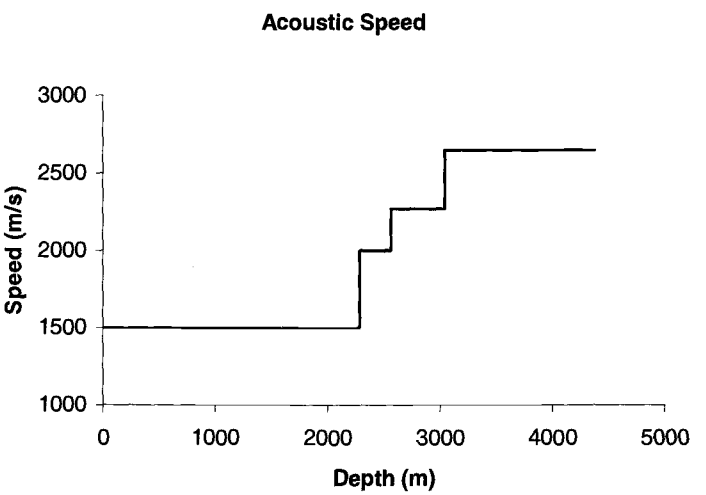

Figure 6.3 (b): Acoustic speed over depth for PG1.

6.2.2 Density Distribution

The main factors that affect density of seawater are salinity, temperature, and pressure. The density of seawater approximately varies in the range of $1023\,kg/m^3$ at the water surface to $1036\,kg/m^3$ at 2000 m deep (Knauss, 1978). In this study, we assume the density of water layer $1028\,kg/m^3$. However, the sediments are composed of solid particles and water. The bulk density of sediments can be calculated from the formula

$$\rho_b = \rho_p(1-\theta)+\rho_w\theta \tag{6.3}$$

where ρ_b is the bulk density of sediments, ρ_p is the particle density, ρ_w is the water density and θ is the porosity. Table 6.3 shows the particle density and porosity of the sediments at different depths below the sea level (bsl) at a reference point (42.44°N, 143.90°E) near PG1 (Oil and Natural Gas Resource in Japan, 1992). We can assume the physical properties of the sediments below the sea floor at the reference point is the same as PG1. The depth of sediments at PG1 and the corresponding particle density and porosity are shown in Table 6.4. To match the sea floor elevation at PG1, the values in the first column of this table are obtained by adding 1100 m (2283 -1183 = 1100 m) to every value in the first column of Table 6.3. The bulk density of the sediments at PG1 was calculated by Equation (6.3) and shown in Table 6.4 (Note that the sea water density ρ_w used here is $1028\,kg/m^3$ and the deviation due to increasing pressure is negligible in comparison with the uncertainty involved in the sediment structure).

Table 6.3: Particle density and porosity of the sediments at the reference point with the depth (bsl) (Oil and Natural Gas Resource in Japan, 1992).

Depth (bsl) (m)	Particle Density (kg/m^3)	Porosity (%)
1183	2471	41.7
1600	2473	37.2
2020	2567	28.0
2087	2639	26.9
2105	2633	25.0
2120	2615	27.9
2145	2634	28.6
2245	2599	29.0
2405	2651	26.9
2433	2645	26.1
2501.2	2615	14.9
2504.5	2657	19.8
2849	2679	28.5
3486.3	2644	14.1

Table 6.4: Particle density, porosity and bulk density of the sediments at PG1 with the depth (bsl).

Depth (bsl) (m)	Particle Density (kg/m^3)	Porosity (%)	Bulk Density (kg/m^3)
2283	2471	41.7	1869.27
2700	2473	37.2	1935.46
3120	2567	28.0	2136.08
3187	2639	26.9	2205.64
3205	2633	25.0	2231.75
3220	2615	27.9	2172.23
3245	2634	28.6	2174.68
3345	2599	29.0	2143.41
3505	2651	26.9	2214.41
3533	2645	26.1	2222.96
3601.2	2615	14.9	2378.54
3604.5	2657	19.8	2334.46
3949	2679	28.5	2208.47
4586.3	2644	14.1	2416.14

Figure 6.4 shows the variation of the bulk density of the sediments at PG1 with the depth. In this figure, the discrete circles denote the data points listed on Table 6.4, and the solid poly-line connected by four triangles is a fitting curve of these discrete data points. The two lowest points and the highest point on this poly-line are the same as the corresponding data in Table 6.4 depicted with the circular points. The point P (triangle) is obtained by calculating the average of the data (circular points) closed in the dashed rectangle. We use this poly-line as the estimated density profile for the sediment layers

and the profile in the depth including the sea water column at PG1 is presented in Figure 6.5 and also listed in Table 6.5.

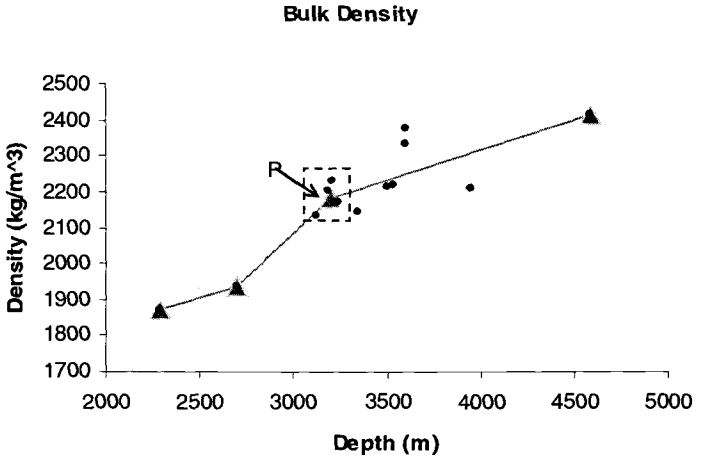

Figure 6.4: Variations of the bulk density of the sediments at PG1 with the depth. The discrete circles denote the bulk density at different depths listed on Table 6.5, and the solid poly-line connected by four triangles is a fitting curve of these discrete data points. The point P (triangle) is obtained by calculating the average of the circular points closed in the dashed rectangle.

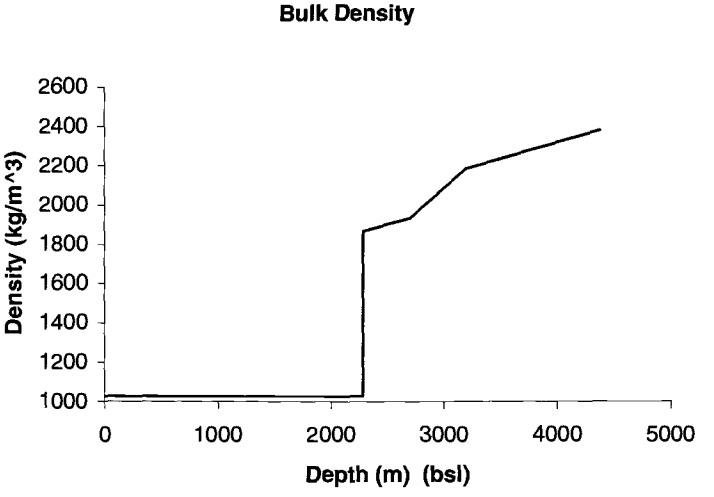

Figure 6.5: Estimated density profile in the depth including the seawater column at PG1.

Table 6.5: Density variations with the depth (below the sea level) at PG1.

Depth (m) bsl	Density (kg/m^3)
0 – 2283	1028
2283 – 2700	1869.27 – 1935.46
2700 – 3195.4	1935.46 – 2184.076
3195.4 – 4373	2184.076 – 2380.556

6.3 Simulation of Pressure Waves

6.3.1 Model 1: Water Column

First, we consider the medium of pressure wave excursion within the seawater column only – neglecting all the soft sediment layers that might have contributed to the formation of the pressure wave observed in the field. In this case, the entire pressure wave energy is assumed to be reflected at the sea bottom. Figure 6.6 shows the one-layer model for simulating pressure waves. The speed of acoustic wave in seawater and the seawater density are $c_w = 1500 m/s$ and $\rho_w = 1028 kg/m^3$, respectively (See Tables 6.2 and 6.5). The pressure gauge (PG1) is located at the seafloor ($H_w = 2283 m$). These parameters are also presented in Table 6.6.

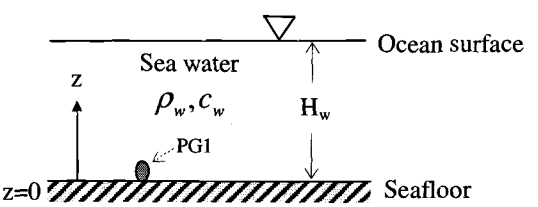

Figure 6.6: One-layer model (water column) for simulating pressure waves.

Table 6.6: Thickness and elastic properties of the water layer.

Media	Thickness	Acoustic Speed	Density
Seawater	$H_w = 2283m$	$c_w = 1500m/s$	$\rho_w = 1028kg/m^3$

The pressure variations at PG1 are computed numerically using the algorithm discussed in Chapter 4. Here, and henceforward, we use $\tau_{PG1} = 4s$ (Nosov, 2005) and $\alpha = 0$ in simulation calculation for PG1, where τ_{PG1} is the duration of the seafloor uplift at PG1 and α is the damping coefficient. Figure 6.7 presents the periodogram of the simulated acoustic pressure variations at the seafloor for the duration from 0 to 2400 seconds using the one-layer model: note that in the computation, the seafloor displacement starts at t = 0 and ceases at t = 4 seconds. In the figure, the first three peak frequencies are found at 0.163 Hz, 0.490 Hz and 0.817 Hz.

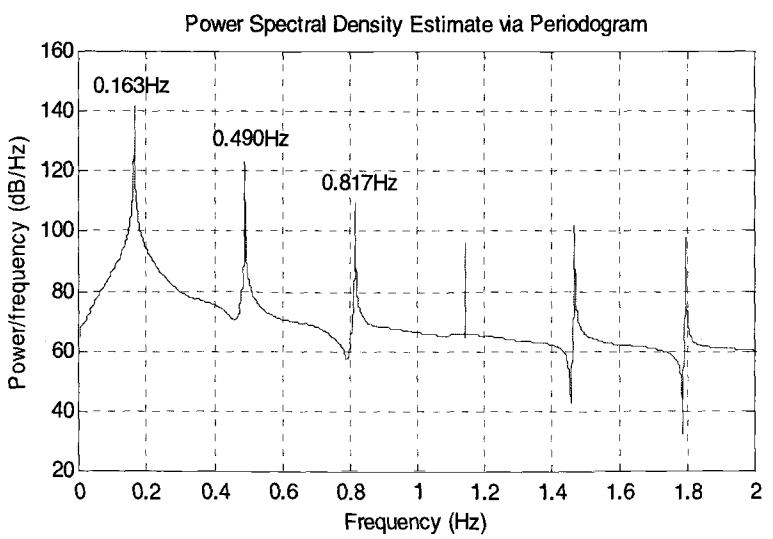

Figure 6.7: Periodogram of simulated acoustic pressure variations at PG1 for the duration from 0 to 2400 sec. using one-layer model (The seafloor displacement starts at t = 0 and ceases at t = 4 seconds).

The natural (characteristic) frequencies of elastic oscillations of water layer can be analytically calculated by Equation (5.11): the first three solutions are $f_1 = 0.164Hz$, $f_2 = 0.492Hz$ and $f_3 = 0.821Hz$ ($k = 1,2,3$), which are, as expected, essentially identical to those computed numerically as shown in Table 6.7.

Table 6.7: The first three peak frequencies of the numerical simulation and the theoretically calculated natural frequencies for one-layer model.

Frequencies	f_1	f_2	f_3
Simulated (Hz)	0.163	0.490	0.817
Theoretical (Hz)	0.164	0.493	0.821

Figure 6.8 shows the smoothed periodogram (i.e. spectrum) of the filtered field pressure data shown in Figure 3.12 for the duration of 250–1750 seconds with a moving average of length 40, i.e., a window size of 41 points. The reason for choosing the time interval of 250–1750 seconds is that the dominant frequency is relatively stable (fairly constant varying between 0.120 and 0.133 Hz) in the range of 250–1750 seconds (See Table 3.3). Figure 6.8 indicates that the dominant peak frequency of the measured pressure wave at PG1 is 0.131 Hz. According to the model result (Figure 6.7), the dominant peak frequency was predicted at 0.163 Hz: the discrepancy is substantial.

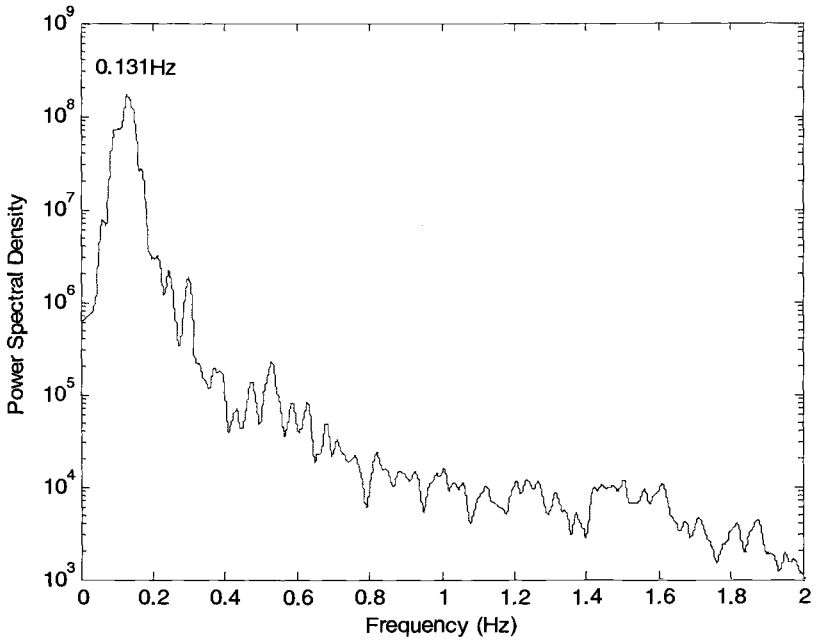

Figure 6.8: Smoothed periodogram of the filtered field pressure data for the duration of 250–1750 seconds. The dominant frequency is 0.131 Hz.

6.3.2 Model 2: Water Column and Single Sediment Layer

Our hypothesis is that the sediment layer, if it is soft enough, should play a role in the pressure wave transmission. As for the simplest case, we add the single sediment layer of 2090 m thick (280 + 480 + 1330 = 2090 m as listed in Table 6.2) with the constant elastic properties to simulate the pressure waves (coupled elastic oscillations of water column and single sediment layer) and assume an acoustic basement below the sediments to be absolutely rigid. Figure 6.9 shows the two-layer model used in the simulation, in which H_w is the water depth, c_w is the acoustic speed in water, ρ_w is the water density, H_s is the thickness of sediment layer, c_s is the acoustic speed in sediment layer and ρ_s is the sediment density. These parameters are listed in Table 6.8 (based on Tables 6.2 and 6.5),

where $c_s = 2476m/s$ is the weighted averaged acoustic speed in the sediment layer of 2090m thick: $c_s = (2000\times280+2270\times480+2650\times1330)/(280+480+1330) \approx 2476m/s$, and $\rho_s = 2154kg/m^3$ is the averaged density of the sediment layer.

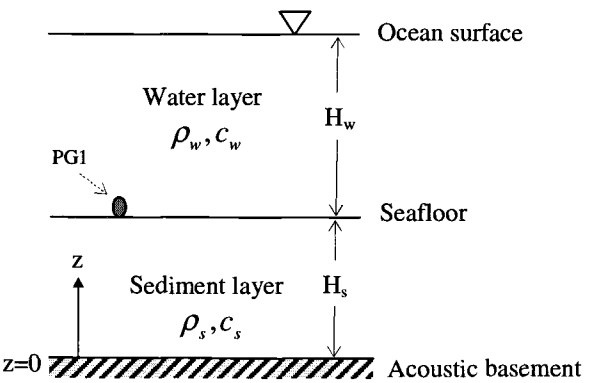

Figure 6.9: Two-layer model (water column and single sediment layer) for simulating pressure waves (PG1 is located at the seafloor).

Table 6.8: The respective thickness and elastic properties of water and one sediment layer.

Media	Thickness	Acoustic Speed	Density
Sea Water	$H_w = 2283m$	$c_w = 1500m/s$	$\rho_w = 1028kg/m^3$
Sediment	$H_s = 2090m$	$c_s = 2476m/s$	$\rho_s = 2154kg/m^3$

Figure 6.10 shows the periodogram of the simulated acoustic pressure variations at PG1 for the duration from 0 to 2400 seconds using the two-layer model (The acoustic basement uplift starts at t = 0 and ceases at t = 4 seconds). It can be found that the first three peak frequencies of the periodogram are 0.138 Hz, 0.306 Hz and 0.507 Hz, respectively.

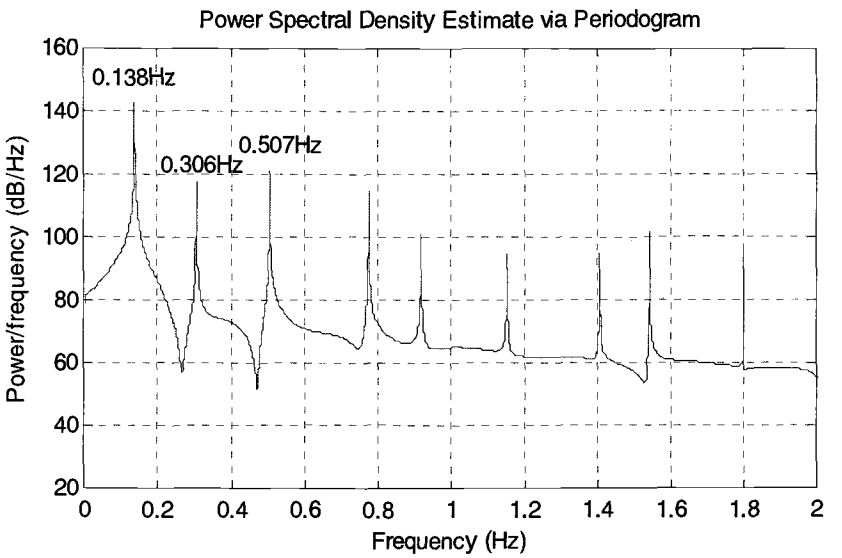

Figure 6.10: Periodogram of the simulated acoustic pressure variations at PG1 for the duration of 0–2400 seconds using the two-layer model (The acoustic basement uplift starts at t = 0 and ceases at t = 4 seconds) and the first three peak frequencies identified in the figure.

The natural frequencies of the coupled elastic oscillations of water column and single sediment layer can be computed analytically by Equation (5.25), which yields the theoretical solutions for the first three natural frequencies: $f_1 = 0.138Hz$, $f_2 = 0.307Hz$ and $f_3 = 0.507Hz$. Table 6.9 presents the first three natural frequencies for numerical simulation and theoretical calculation using two-layer model, which shows that the numerically calculated result is the same as the theoretical solution for two-layer model, as expected.

Table 6.9: The first three peak frequencies of the numerical simulation and the theoretically calculated natural frequencies for two-layer model.

Frequencies	f_1	f_2	f_3
Simulated (Hz)	0.138	0.306	0.507
Theoretical (Hz)	0.138	0.307	0.507

The dominant frequency of the simulated pressure wave for the two-layer model (0.138 Hz) is in good agreement with that of the measurements (0.131 Hz as shown in Figure 6.8). This strongly suggests that the sediment layer must have played a role in the formation of the pressure wave after the earthquake.

6.3.3 Model 3: Water Column and Two Sediment Layers

Now we will discuss the three-layer model (water column and two sediment layers) as shown in Figure 6.11, where H_w is the water depth, c_w is the acoustic speed in water, ρ_w is the water density, H_{s_1} and H_{s_2} are the thickness of sediment layers 1 and 2, respectively, c_{s_1} and c_{s_2} are the acoustic speed in sediment layers 1 and 2, respectively, and ρ_{s_1} and ρ_{s_2} are the density of sediment layers 1 and 2, respectively. These parameters are listed in able 6.10 (based on Tables 6.2 and 6.5), in which $H_{s_1} = 280 + 480 = 760m$, $c_{s_1} = 2171m/s$ is the weighted averaged acoustic speed in the sediment layer 1 of 760 m thick: $c_{s_1} = (2000 \times 280 + 2270 \times 480)/(280 + 480) \approx 2171m/s$, $\rho_{s_1} = 1956kg/m^3$ and $\rho_{s_2} = 2267kg/m^3$ are the averaged density of sediment layers 1 and 2, respectively.

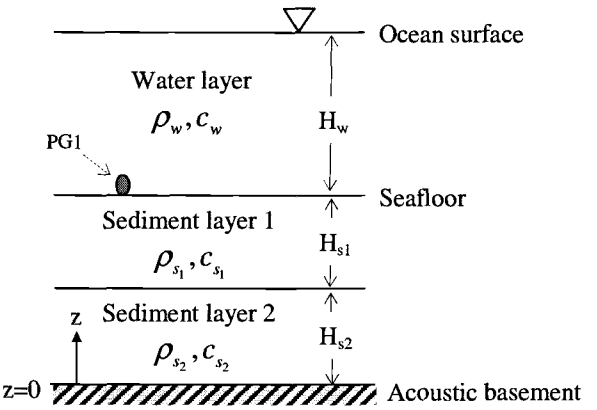

Figure 6.11: Three-layer model (water column and two sediment layers) for simulating pressure waves (PG1 is located at the seafloor).

Table 6.10: The respective thickness and elastic properties for water column and two sediment layers.

Media	Thickness	Acoustic Speed	Density
Sea Water	$H_w = 2283m$	$c_w = 1500m/s$	$\rho_w = 1028kg/m^3$
Sediment 1	$H_{s_1} = 760m$	$c_{s_1} = 2171m/s$	$\rho_{s_1} = 1956kg/m^3$
Sediment 2	$H_{s_2} = 1330m$	$c_{s_2} = 2650m/s$	$\rho_{s_2} = 2267kg/m^3$

Figure 6.12 shows the periodogram of the simulated acoustic pressure variations at PG1 for the duration from 0 to 2400 seconds using the three-layer model. The first three peak frequencies of the periodogram are 0.138 Hz, 0.325 Hz and 0.511 Hz, respectively. The dominant peak frequency (0.138 Hz) is identical to that of two-layer model.

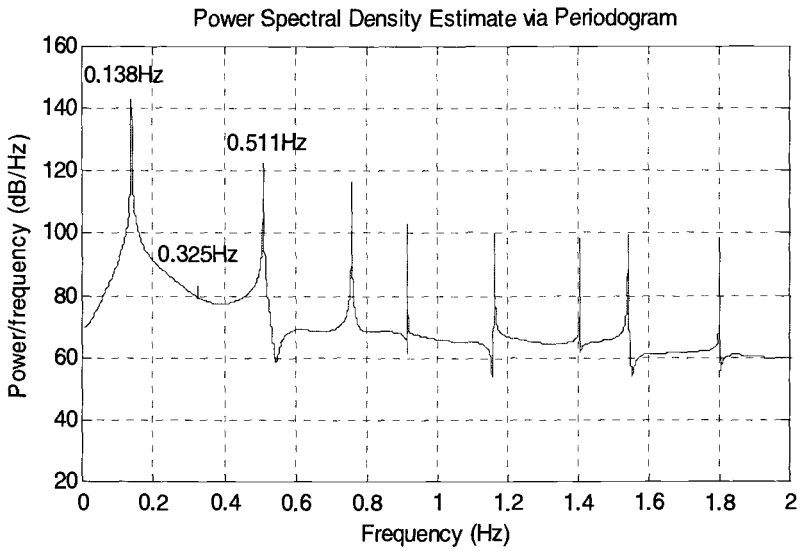

Figure 6.12: Periodogram of the simulated acoustic pressure variations at PG1 for the duration of 0–2400 seconds using the three-layer model (The acoustic basement uplift starts at t = 0 and ceases at t = 4 seconds) and the first three peak frequencies identified in the figure.

Table 6.11 lists the first three natural frequencies for numerical simulation and analytical calculation based on Equation (5.43) using three-layer model. As expected, the numerically computed result is essentially identical to the analytical solution for three-layer model.

Table 6.11: The first three peak frequencies of the numerical simulation and the theoretically calculated natural frequencies for three-layer model.

Frequencies	f_1	f_2	f_3
Simulated (Hz)	0.138	0.325	0.511
Theoretical (Hz)	0.138	0.326	0.509

6.3.4 Model 4: Water Column and Sediment Layer with Continuous Density

Figure 6.13 shows the periodogram of the simulated acoustic pressure variations at PG1 for the duration of 0–2400 seconds with the acoustic speed and density distributions shown in Figures 6.3 and 6.5, respectively (The density of sediments varies continuously). The dominant peak frequency of the periodogram is 0.138 Hz, which is the same as that of two-layer and three-layer models.

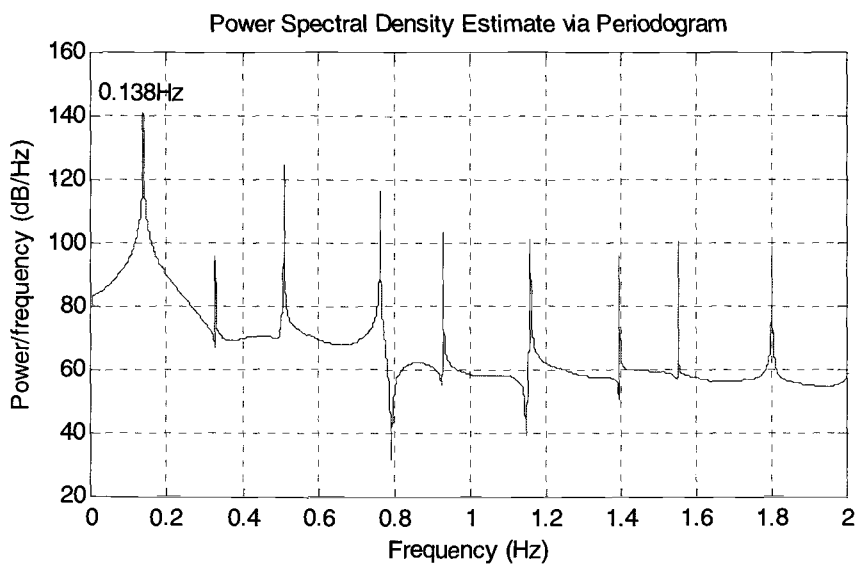

Figure 6.13: Periodogram of the simulated acoustic pressure data at PG1 for the duration of 0–2400 seconds using Model 4 (The acoustic basement uplift starts at t = 0 and ceases at t = 4 seconds). The dominant peak frequency is 0.138 Hz.

Table 6.12: Dominant frequencies for the 4 models above and in-situ measurement.

	Model 1	Model 2	Model 2	Model 4	Measurement
Dominant Frequency	0.163 Hz	0.138Hz	0.138 Hz	0.138 Hz	0.131Hz

For the four models discussed above, Model 4 (water column and sediment layer with continuous density) is the most realistic. To get better simulation result, we need to have a good estimation on the values of τ and α, where τ is the duration of the seafloor displacement and α is the damping coefficient (See Equation (4.5)). Since α affects the pressure-wave attenuation, it can be estimated by comparing the e-folding times for the simulated and measured pressure waves. For the measured pressure wave, the e-folding time for the first 150 seconds of the mainshock is about 75.4 seconds (See Table 3.2). By adjusting the value of α, we find that the e-folding time for the simulated pressures waves is 75.39 seconds when $\alpha = 0.0264 s^{-1}$, which is good enough for simulation. After fixing the value of α, we will estimate the value of τ in two ways:

1. To match the maximum peak-to-peak amplitudes of the simulated and measured pressure waves. For the duration of 0–2400 seconds, the maximum peak-to-peak amplitude of the simulated pressure wave with $\alpha = 0.0264 s^{-1}$ and $\tau = 7 s$ is 4.52×10^5 Pa, which is very close to that of the filtered field pressure data shown in Figure 3.6 (4.85×10^5 Pa). The time history of the simulated pressure variations at PG1 for the duration of 0–1000 seconds using Model 4 with $\alpha = 0.0264 s^{-1}$ and $\tau = 7 s$ is plotted by the dotted line in Figure 6.14. The filtered field pressure data at PG1 is also shown in this figure, denoted by the solid line. Figure 6.15 presents the power spectra of the measured (solid line) and simulated pressure data (dotted line) at PG1 for the duration of 250–2400 seconds using Model 4 with $\alpha = 0.0264 s^{-1}$ and $\tau = 7 s$. The spectrum of the measured data is obtained by smoothing the periodogram with a moving average of length 50. The dominant peak frequencies of measured and simulated pressure waves are 0.130 Hz and

0.138 Hz, respectively (The values of α and τ have no effect on the natural frequencies of the simulated pressure waves).

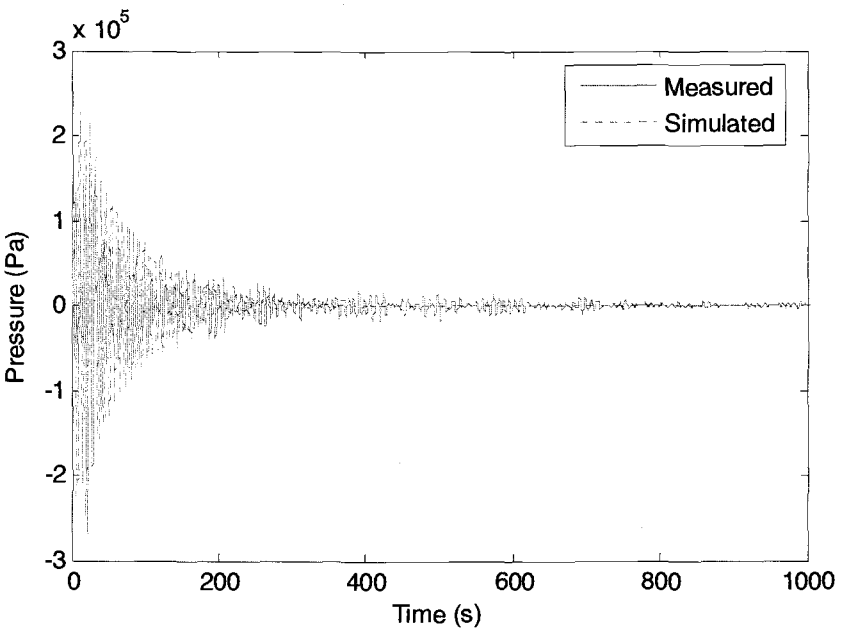

Figure 6.14: Time histories of the measured (solid) and simulated pressure data (dotted) at PG1 for the duration of 0–1000 seconds using Model 4 with $\alpha = 0.0264 s^{-1}$ and $\tau = 7 s$ (The time origin corresponds to the start of the mainshock).

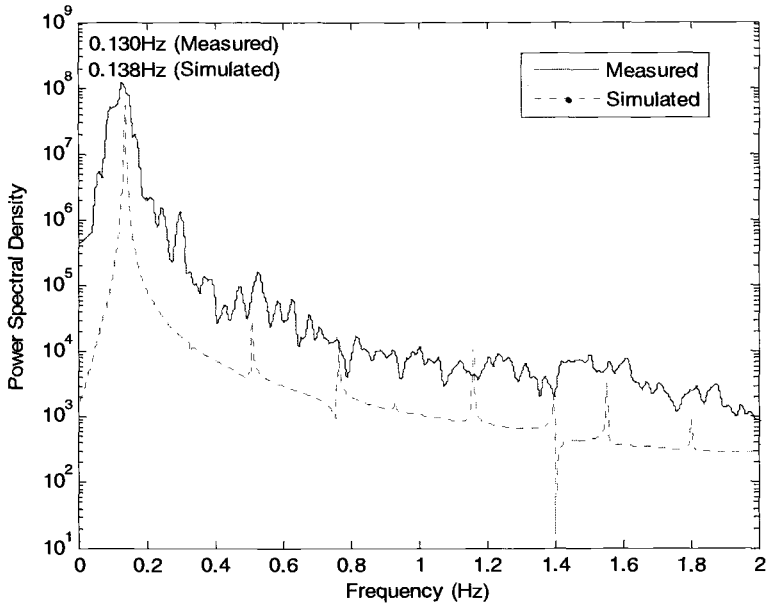

Figure 6.15: Power density spectra of the measured (solid) and simulated pressure data (dotted) at PG1 for the duration of 250–2400 seconds using Model 4 with $\alpha = 0.0264 s^{-1}$ and $\tau = 7 s$. The dominant peak frequencies of the measured and simulated pressure waves are 0.130 Hz and 0.138 Hz, respectively.

2. To match the total power of the power density spectra for the simulated and measured pressure data. The total power is the sum of the power spectra density (PSD): $E = \sum (PSD)$ $(= \sum p^2 \Delta t)$. For the duration of 0–2400 seconds, the total power of the spectrum for the simulated pressure data is $E = 5.38 \times 10^{11} Pa^2 \cdot s$ with $\tau = 7.9 s$ $(\alpha = 0.0264 s^{-1})$, which is quite close to that of the measured data, $E = 5.44 \times 10^{11} Pa^2$. Figure 6.16 presents the time histories of the measured (solid) and simulated pressure variations (dotted) at PG1 for the duration of 0–1000 seconds using Model 4 with $\alpha = 0.0264 s^{-1}$ and $\tau = 7.9 s$. The power spectra of the measured and simulated pressure data at PG1 for the duration of 250–2400 seconds with $\alpha = 0.0264 s^{-1}$

and $\tau = 7.9s$ are shown in Figure 6.16, in which the dominant peak frequencies of the measured and simulated pressure waves are 0.130 Hz and 0.138 Hz, respectively.

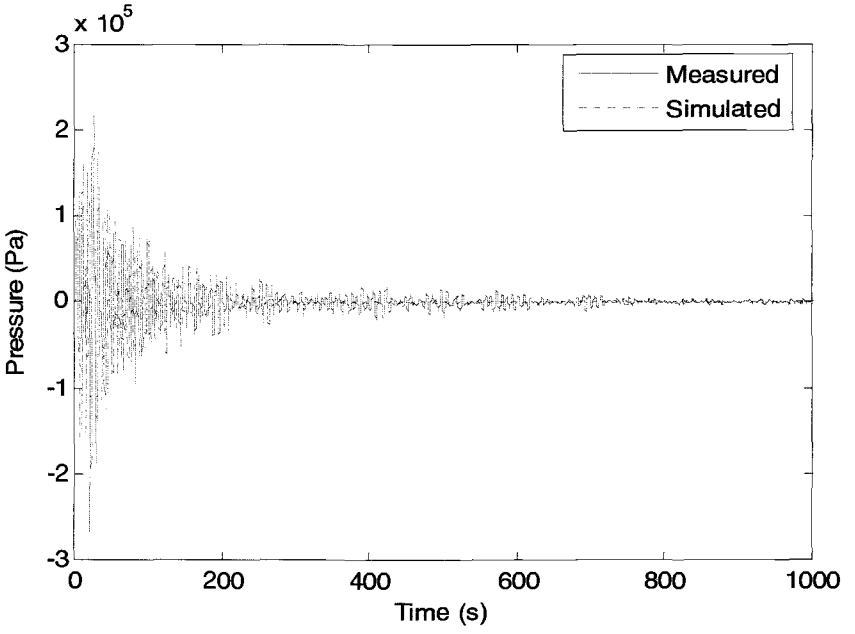

Figure 6.16: Time histories of the measured (solid) and simulated pressure data (dotted) at PG1 for the duration of 0–1000 seconds using Model 4 with $\alpha = 0.0264s^{-1}$ and $\tau = 7.9s$ (The time origin corresponds to the start of the mainshock).

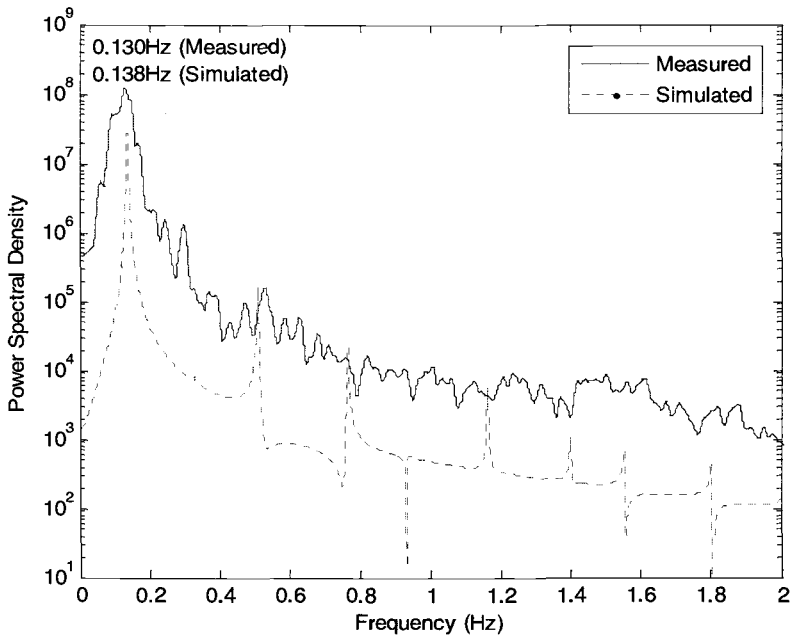

Figure 6.17: Power density spectra of the measured (solid) and simulated pressure data (dotted) at PG1 for the duration of 250–2400 seconds using Model 4 with $\alpha = 0.0264 s^{-1}$ and $\tau = 7.9 s$. The dominant peak frequencies of the measured and simulated pressure waves are 0.130 Hz and 0.138 Hz, respectively.

7 Conclusions

The pressure fluctuations observed at the ocean bottom during the 2003 Tokachi-Oki earthquake were studied. The dominant frequency of the pressure fluctuations at PG1 is fairly constant varying between 0.120 and 0.133 Hz. This suggests that there is one dominant physical mechanism to sustain the regular pressure fluctuation that was triggered by the seafloor displacement due to the earthquake.

A few of aftershocks subsequently occurred and the largest aftershock followed about one hour after the mainshock. The amplitude of pressure fluctuations attenuates quickly after every aftershock, which can be explicitly observed in the band-pass filtered pressure data. The e-folding time for the attenuation of pressure wave was estimated for each shock. The e-folding times for the mainshock, 1st aftershock and 3rd aftershock are quite similar. However, the e-folding time for the 2nd aftershock is much shorter than the other events. This indicates that the source mechanism of the 2nd aftershock must be different from other events; such as the rupture of a very small area or not occurred at PG1 but somewhere nearby.

The amplitude modulation of the pressure fluctuations caused by the mainshock was investigated by applying the variable-frequency complex demodulation method (VFCDM). The modulating behavior must be related to the inhomogeneous sediment layers in which the pressure waves penetrate (i.e. multiple layers for pressure wave to resonate besides the water column). The temporal evolution of amplitude spectra of the pressure fluctuations at PG1 demonstrates that the dominant frequency of the pressure data decreases gradually, while the dominant component is energetic without fading away

into the background noise. The energy decay process is oscillatory with the period of approximately 100 seconds, which must be related to the tsunamis generated by the earthquake.

Based on the method of characteristics, a one-dimensional numerical model is constructed to simulate the pressure wave propagation. The dominant frequency of the simulated pressure wave is in good agreement with that of the measurement if sediment layers are taken into account. Since the natural (characteristic) frequencies of the acoustic wave oscillation depend on the elastic properties of the medium alone, the sediment layers must play a role in the formation of the pressure wave caused by the seafloor displacement. The natural frequencies were also computed analytically for one-layer model (water column), two-layer model (water column and single sediment layer) and three-layer model (water column and two sediment layers); the results are, as expected, essentially identical to the numerically computed ones.

According to the time history of the co-seismic seafloor displacement provided by Hirata (2004), the seafloor displacement took place in the duration of about 20 min. He also estimated the co-seismic uplift of the seafloor based on the low-pass filtered pressure data: the net uplift is 0.33m at PG1. Nosov (2005) estimated the duration of the bottom displacement $\tau_{PG1} \approx 4s$ with the constant co-seismic bottom displacement velocity $U \sim 0.1m/s$. In the present study, a half cosine curve is used to simulate the time history of the seafloor displacement. By matching the e-folding times of the simulated and measured pressure waves, the damping coefficient α is estimated to be $\alpha = 0.0264s^{-1}$. Furthermore, by matching the maximum peak-to-peak amplitudes or matching the total

power, the duration of the bottom displacement τ is determined as $\tau = 7s$ or $\tau = 7.9s$, respectively. Note that both the duration of the bottom displacement τ and the damping coefficient α have no effects on the natural frequencies of the pressure waves.

Bibliography

Bloomfield, P. (2000), Fourier Analysis of Time Series An Introduction (2nd Edition), *Wiley Series in Probability and Statistics*, John Wiley & Sons, Inc.

Finch, R. D. (2005), Introduction to Acoustics, Pearson Education, Inc., Upper Saddle River, NJ 07458.

Gasquet, H., and A. J. Wootton (1997), Variable-Frequency Complex Demodulation Technique for Extracting Amplitude and Phase Information, *Review of Scientific Instruments*, *68*(1), pt 2, 1111–1114.

Hashimoto, N., M. Mitsui, Y. Goda, T. Nagai, and T. Takahashi (1996), Improvement of Submerged Doppler-type Directional Wave Meter and Its Application to Field Observation, *Proceedings of the 25th International Conference on Coastal Engineering (ICCE'96)*, *1*, 629–642.

Hirata, K. (2004), Personal Communication.

Hirata, K., M. Aoyagi, H. Mikada, and K. Kawaguchi, Y. Kaiho, R. Iwase, S. Morita, I. Fujisawa, H. Sugioka, K. Mitsuzawa, K. Suyehiro, H. Kinoshita, and N. Fujiwara (2002), Real-time geophysical measurements on the deep seafloor using submarine cable in the southern Kurile subduction zone, *IEEE Journal of Oceanic Engineering*, *27*(2), 170–181.

Hirata, K., T. Baba, H. Sugioka, H. Matsumoto, E. Araki, T. Watanabe, H. Mikada, K. Mitsuzawa, R. Iwase, R. Otsuka, S. Morita, and K. Suyehiro (2003), Ocean-bottom Near-field Observation to the 2003 Tokachi-oki Earthquake with Cabled Seafloor Observatory, *2003 AGU Fall Meeting*, *84*(46), Abstract S52L–04.

Hirata, K., Y. Tanioka, K. Satake, S. Yamaki, and E. L. Geist (2004), The Tsunami Source Area of the 2003 Tokachi-Oki Earthquake Estimated from Tsunami Travel Times and Its Relationship to the 1952 Tokachi-Oki Earthquake, *Earth Planets Space*, *56*(3), 367–372.

Ichiyanagi, M., H. Takahashi, and M. Kasahara (2004), Aftershock Activity of the 2003 Tokachi-Oki Earthquake ($M_{JMA} = 8.0$), *Geophysical Bulletin of Hokkaido University*, *64*.

Kajiura, K. (1970), Tsunami Source, Energy and the Directivity of Wave Radiation, *Bulletin of Earthquake Research Institute*, *48*, 835–869.

Kato, T., Y. Terada, M. Kinoshita, H. Kakimoto, H. Isshiki, T. Moriguchi, M. Tanno, M. Kanzaki, and J. Johnson (2001), A New Tsunami Monitoring System using RTK-GPS, *ITS 2001 Proceedings*, Session 5, Number 5-12, 645–651.

Knauss, J. A. (1978), Introduction to Physical Oceanography, Prentice Hall, Inc., Englewood Cliffs, NJ, pp 338.

Landau, L. D. (Deceased), E. M. Lifshitz (1959), Fluid Mechanics, *Course of Theoretical Physics, Volume 6*, Pergamon Press Ltd., Headington Hill Hall, Oxford, England.

Nagai, T., N. Hashimoto, K. Kawaguchi, H. Yokoi, M. Kudaka, and M. Mitsui (2002), Frequency Banded Wave Climate Description Based on the Observed Directional Spectra, *Coastal Engineering Journal (CEJ), Japan Society of Civil Engineers, 44*, 1, 53–65.

Nagai, T., and K. Nukada (2004a), Recent Improvement of Real-time Coastal Wave-tide Information System in Japan, *Workshop on Wave, Tide Observations and Modelings in the Asian-Pacific Region.*

Nagai, T., H. Ogawa, K. Nukada, and M. Kudaka (2004b), Characteristics of the Observed 2003 Tokachi-off Earthquake Tsunami Profile, *Coastal Engineering Journal, 46*(3), 315–327.

Nagai, T., S. Satomi, Y. Terada, T. Kato, K. Nukada, and M. Kudaka (2005), GPS Buoy and Seabed Installed Wave Gauge Application to Offshore Tsunami Observation, *Proceedings of the 15th International Offshore and Polar Engineering Conference (ISOPE-2005)*, 292–299.

Nagai, T., K. Sugahara, N. Hashimoto, T. Asai, S. Higashiyama, and K. Toda (1994), Introduction of Japanese NOWPHAS system and its current topics, *Proceedings of the International Conference on Hydro-Technical Engineering for Port and Harbor Construction (HYDRO-PORT'94)*, PHRI, 67–82.

Nosov, M. A. (1999), Tsunami Generation in Compressible Ocean, *Physics and Chemistry of the Earth, Part B, 24*(5), 437–441.

Nosov, M. A. (2000), Tsunami Generation in a Compressible Ocean by Vertical Bottom Motions, *Izvestiya, Atmospheric and Oceanic Physics, 36, No. 5*, 718–726.

Nosov, M. A. (2005), Elastic Oscillation of Water Layer in the 2003 Tokachi-Oki Tsunami Source, *22nd IUGG International Tsunami Symposium, Chania, Greece, 27–29, June, 2005.*

Ohmachi, T., H. Matsumoto, and H. Tsukiyama (2001), Seawater Pressure Induced by Seismic Ground Motions and Tsunamis, *ITS 2001 Proceedings (Proceedings of the 2001 International Tsunami Symposium)*, Session 5, Number 5-4, 595–609.

Oil and Natural Gas Resources in Japan (1992), Association of Continental Shelf Oil Development, Natural Gas Mining Society.

Streeter, V. L., and E. B. Wylie (1979), Fluid Mechanics (7th Edition), McGraw-Hill, Inc.

Takayama, T., N. Hashimoto, T. Nagai, T. Takahashi, H. Sasaki, and Y. Ito (1994), Development of Submerged Doppler-type Directional Wave Meter, *Proceedings of the 24th International Conference on Coastal Engineering (ICCE'94), 1*, 624–634.

Tanioka, Y., Y. Nishimura, K. Hirakawa, F. Imamura, I. Abe, Y. Abe, K. Shindou, H. Matsutomi, T. Takahashi, K. Imai, K. Harada, Y. Namegawa, Y. Hasegawa, Y. Hayashi, F. Nanayama, T. Kamataki, Y. Kawata, Y. Fukasawa, S. Koshimura, Y. Hada, Y. Azumai, K. Hirata, A. Kamikawa, A. Yoshikawa, T. Shiga, M. Kobayashi, and S. Masaka (2004), Tsunami Run-up Heights of the 2003 Tokachi-Oki Earthquake, *Earth Planets Space, 56*(3), 359–364.

Tomita, T., H. Kawai, and T. Kakinuma (2004), Tsunami Due to the Tokachi-Oki Earthquake in 2003, *UJNR Panel on Wind and Seismic Effects, the 36th Joint Meeting,* session 5.

Ueno, J., S. Takada, and Y. Kuwata (2004), Performance of Water Supply During the 2003 Tokachi-Oki Earthquake, *the Third Taiwan-Japan Workshop on Lifeline Performance and Disaster Mitigation.*

Wylie, E.B., and V.L. Streeter (1978), Fluid Transients, McGraw-Hill, Inc.

Yagi, Y. (2004), Source Rupture Process of the 2003 Tokachi-Oki Earthquake Determined by Joint Inversion of Teleseismic Body Wave and Strong Ground Motion Data, *Earth Planets Space*, *56*, 311–316.

Yamanaka, Y., and M. Kikuchi (2003), Source Process of the Recurrent Tokachi-Oki Earthquake on September 26, 2003, Inferred from Teleseismic Body Waves, *Earth Planets Space*, *55*, e21–e24.